



UNIVERSITY
OF TRENTO - Italy

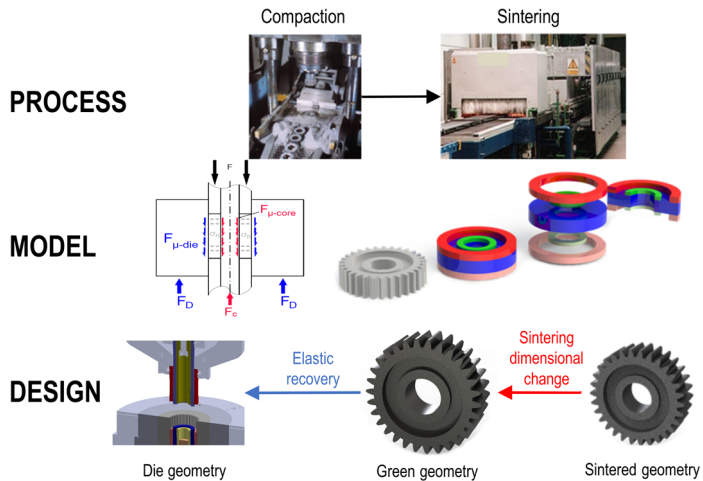
DEPARTMENT OF INDUSTRIAL ENGINEERING

XXXII cycle

Doctoral School in Materials, Mechatronics
and Systems Engineering

Design for anisotropic dimensional change: new insight and practical approach

Marco Zago



June 2020

**DESIGN FOR ANISOTROPIC DIMENSIONAL CHANGE:
NEW INSIGHT AND PRACTICAL APPROACH**

Marco Zago

E-mail: marco.zago-1@unitn.it

Approved by:

Prof. Ilaria Cristofolini, Advisor
Department of Industrial Engineering
University of Trento, Italy.

Prof. Alberto Molinari,
Department of Industrial Engineering
University of Trento, Italy.

Ph.D. Commission:

Prof. Didier Bouvard,
Grenoble INP
University of Grenoble Alpes, France.

Prof. Vigilio Fontanari,
Department of Industrial Engineering
University of Trento, Italy.

Prof. Josè Manuel Torralba,
Department of Materials Science and
Engineering
University of Carlos III Madrid, Spain.

University of Trento,
Department of Industrial Engineering

June 2020

**University of Trento - Department of
Industrial Engineering**

Doctoral Thesis

Marco Zago - 2020

Published in Trento (Italy) – by University of Trento

ISBN: - - - - -

Preface

This thesis has been made in collaboration with the research group of University of Trento headed by prof. Ilaria Cristofolini and prof. Alberto Molinari. This research group has a wide and consistent experience in the field of powder metallurgy and dimensional variation of PM parts, the main topic of the thesis. This wide experience was derived from more than 10 years of active research and publication on journals and conference papers.

The second part of this thesis has been developed thanks to the funding of EPMA, which promoted a Club Project entitled “*Design for Sintering – Dealing with anisotropy of dimensional changes: DfS – Demonstrator Project*”, where the main partners were five European companies:

- **AMES** - sintered components manufacturer, one of the world leaders in the manufacturing of sintered parts, based in Spain, Hungary, USA, China.
- **GKN sinter metals** - the largest producer of PM parts in the world.
- **Höganäs AB** - world leader in the market of iron and metal powders.
- **MIBA** - one of the leading partners of automotive industries, whose portfolio includes sintered components, industrial bearings, friction materials and powder electronic components.
- **Sintex** - company of Grundfos group settled in Denmark, working in many different industrial sectors.

The author would like to thank EPMA, which makes possible the cooperation between academic and industrial sector. In addition, the author would like to thank companies for the materials provided and for their consent to publish the results of this work within the limit of confidential agreement.

Abstract

The competitiveness of conventional press & sinter technology mainly depends on the ability to obtain tight tolerance on sintered products. In order to maintain this strategic advantage in spite of the rapid global market changes, a continuous improvement in the dimensional accuracy of the products has to be pursued. One of the major limits in the dimensional precision of sintered products regards the anisotropic dimensional change occurring on sintering. Despite this problem is well known, an effective design procedure accounting for the anisotropic behavior of dimensional variations is far to be reached. The main reasons concern the multi-physical mechanisms involved and the effect of material, geometry and process condition on the final results. This work aims at developing a design methodology accounting for the anisotropy of dimensional changes on sintering. This study has been performed considering both the fundamental principles and the industrial application, aiming at proposing:

- a solid theory considering the mechanisms which determine the anisotropic dimensional changes;
- a practical and effective design tool for the industrial application.

The role of uniaxial compaction on the origin of anisotropic dimensional change was firstly investigated. AISI 316L ring shaped samples were compacted at different geometries, and four different particle sizes. During single action compaction, forces acting on the tooling and powder column, and related displacements, were recorded by the press in order to derive the compaction mechanics of the powder mixes. Further, the dimensions of the samples were measured before and after sintering. A linear trend was observed correlating the deviatoric stresses occurring in compaction to the anisotropic dimensional variations on sintering. This result offers a new perspective in the prediction of the anisotropic dimensional change, and could lay the foundation of a solid model.

Aiming at developing an effective design tool to predict dimensional change on sintering, the analytical design procedure previously developed by the research group at the University of Trento was validated on real parts. A Club Project was promoted by EPMA, collecting the University of Trento and five qualified industrial partners. These companies provided five different real parts characterized by different materials and geometries, whose dimensions were measured before and after sintering. The comparison of the measured and the predicted sintered dimensions demonstrated that this design approach can be an effective tool for designers.

Further work could implement the promising results obtained investigating the

compaction mechanics in the design procedure, aiming at defining a powerful tool to design PM parts accounting for anisotropic dimensional changes.

Contents

Preface	V
Abstract	VII
1 State of the art	1
1.1 Introduction	1
1.2 Powder Metallurgy: press and sinter	2
1.2.1 Powder production	2
1.2.2 Compaction process	3
1.2.3 Sintering	10
1.2.4 Secondary operation	18
1.3 Dimensional precision of sintered part	19
1.4 Dimensional variation on sintering	21
1.5 Theory and model of anisotropy of dimensional change	23
1.6 Aim of this work	28
2 Part A: Influence of compaction on the anisotropy of dimensional change	29
2.1 Introduction	29
2.2 Experimental procedure (Materials and Methods)	29
2.3 Compaction mechanics	34
2.4 Estimation of the dimensional change	54
2.5 Results and discussion	56
2.5.1 Introduction	56
2.5.2 Densification	56
2.5.3 Elasto-plastic transition threshold	65
2.5.4 Friction coefficients	68
2.5.5 Analysis of stresses	70
2.5.6 Dimensional change on sintering	79
2.5.7 Compaction stress field and sintering shrinkage	89
2.6 Conclusion	95
3 Part B: Design method accounting for the anisotropic dimensional change on sintering	97
3.1 Aim of the work	97
3.2 Introduction	97

3.3	Design procedure	102
3.3.1	Design procedure for large change in volume	105
3.3.2	Design procedure for small change in volume	109
3.3.3	Design procedure applied to multilevel parts	113
3.4	Experimental procedure	116
3.5	Results and discussion	123
3.5.1	Introduction	123
3.5.2	Measurement results	123
3.5.3	Isotropic dimensional change	127
3.5.4	Geometry Break Down	128
3.5.5	Prediction Results	131
3.5.6	Non-cylindrical geometry: oval shape	134
3.5.7	ISO IT tolerance classes	142
3.6	Critical analysis of anisotropic parameters K_{anis}, α	143
3.7	Conclusion	146
	Conclusions and future works	149
	References	151
	Scientific production	165
	Acknowledgments	169

1 State of the art

1.1 Introduction

Powder metallurgy (PM) is a process shaping metal powders into near-net shape or net shape parts by the densification and consolidation processes [1]. There are different reasons why PM has been developed in addition to casting process. Historically, PM was a technology for producing wrought metals which could not be casted due to the high melting temperature of some materials. In the XIX century, the high demand of pure wrought platinum lead to the development of PM process, which consisted in the compaction, sintering and hot forging of platinum powders as described by Wollaston in 1829 [2] and Sobolevsky in 1834 [3]. At the beginning of XX century, William Coolidge patented a PM process for the production of tungsten wire in order to supply the high demand of the new material, which substituted the carbon filament in Edison bulb lamp [4]. In same years, PM expanded thanks to new product: self-lubricating bearings. Lowendahl patented a method for the production of bearings obtained mixing bronze powders with ammonium nitrate [5]. The ammonium nitrate was used as a pore former to control the size of pores, which were filled with lubricant after sintering. In Germany, Karl Schröter filed a patent for the production of cemented carbide by PM process in 1925 [6].

In second half of XX century PM production widened in high variety of structural parts. The reason of the increased interest in this technology did not depend on the high melting temperature of some metal materials or the advantage of a porous structure, but on the economical perspective. There is a great number of structural parts which require dimensional tolerances and mechanical properties, which are fitted by PM technology at a lower cost compared to competitor processes [7]. The main advantages of conventional PM technology are:

- the energy and material sustainability, since low scraps are produced and lower energy consumption is required comparing with other metal manufacturing technologies, as reported in table 1.1 [8].
- PM is a net-shape or near net-shape technology, which reduces or avoids secondary operations.
- Complex geometries can be produced without extra operation, as turning or machining.
- PM parts have good surface finishing and roughness.
- High production rate can supply huge demand of consumer goods.

Raw material utilisation	Manufacturing process	Energy requirement per kg of finished part
95	Powder Metallurgy	29
90	Casting	30-38
85	Cold or Warm extrusion	41
75-80	Hot drop forging	46-49
40-50	Machining processes	66-82
% 75 50 25		25 50 75 MJ

Table 1.1. Comparison of the raw metal and energy consumption for different manufacturing processes [8].

1.2 Powder Metallurgy: press and sinter

As summarized by European Powder Metallurgy Association (EPMA), powder metallurgy includes more process technologies: press & sinter (P&S), metal injection molding (MIM), hard metals (HM) and additive manufacturing (AM). P&S is the most widespread in terms of material usage. In 2017, 250 thousand tons of parts have been produced in European countries. Among them 80% have been produced by press and sinter of ferrous materials and 6% by press and sinter of non-ferrous materials.

From an economical perspective, the value of PM part production was 11.6 billion of dollars in 2017 in Europe, where 28% was represent by PM structural parts and bearings produced by press and sinter [8]. Parts produced by P&S are mainly absorbed by automotive sector, in particular components for: power train, engine, transmission, gear box, clutches, shock absorber, oil pumps. Despite the electrification of automotive engine system, PM and P&S could keep a central role in the supply chain of automotive sector.

1.2.1 Powder production

Powder metallurgy process can be divided into powder production and densification processes. There are a great variety of powder production processes based on material type and consolidation method. Without entering into the detail, metal powders can be produced by following methods:

- Physical processes: water and gas atomization.
- Chemical processes: electrolytic (Cu, Fe), thermochemical (Fe), precipitation (Ni, precious materials).
- Mechanical processes: milling, friction, shock.

1.2.2 Compaction process

In conventional P&S, compaction process aims at pressing metal powder in the so-called green part. The green compact is dimensionally close to the final geometry, however metal powders are weakly bonded together by Van der Waals forces. Since green parts do not have sufficient mechanical resistance, compacts are then consolidated by sintering process.

Uniaxial cold compaction is the shaping process most extensively used in PM industrial application, in comparison to warm compaction, wall die lubrication, cold and hot isostatic compaction, roll compaction and explosive compaction. Uniaxial cold compaction basically needs a shaped die cavity, a certain number of upper and lower punches based on the part complexity, and in some cases core-rods for creating holes.

Conventional uniaxial compaction process can be divided in four main steps as shown in figure 1.1:

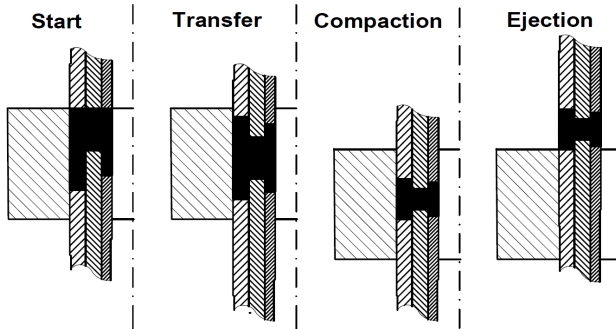


Figure 1.1. Schematic examples of the fundamental steps in uniaxial cold compaction: start, powder transfer, compaction, part ejection.

During uniaxial press cycle, a feed shoe sweeps over the die cavity filling it by particles. The powder filling height ($H_{filling}$) corresponding to the height at the beginning of compaction, is calculated for each column by equation (1.1) [9]:

$$H_{filling} = \frac{\rho_{green}}{\rho_{filling}} H_{green} \quad (1.1)$$

Where:

- H_{green} is the desired height of the column in the green part,
- $\frac{\rho_{green}}{\rho_{filling}}$ is the filling factor, which is the ratio between the required green

density and the filling density.

For multilevel parts, the powder columns must be properly positioned before compaction. This operation is called powder transfer and consists in the synchronized movement of punches, which shift powder columns in a proportional configuration, with respect to the final geometry. Theoretically, powder transfer is correctly carried out if:

- the density and height of each column does not change in relation to the filling stage,
- no shear deformation verified between adjacent columns.

In the compaction step, powder columns are plastically deformed by means of the axial force transmitted by the punches to the powders. While the pressure rises up, in each column the height progressively decreases and density increases simultaneously. The most widespread compaction technique uses double action compaction process, in which the upper and lower punches, or the upper punches and the die, synchronously move during compaction. These cooperative movements determine the same force acting on upper and lower punches and minimize the gradient of density in the compact around the neutral zone.

After compaction, axial force is reduced to the 10-15% of maximum force reached on compaction (hold down force). A complete removal of compressive force could cause cracks formation due to the different elastic recovery of the compact and the punches. The last step of the compaction cycle consists in the ejection of the part from the die. Lower punches push the compact out of the die, or the die is moved downwards. Afterward the green part is removed by the press working plane, before the compaction cycle starts again.

During powder compaction different densification mechanisms modify both powder morphology and material hardening behavior. In the filling step, particles flow in the die cavity pushed by the gravity force. The shape of the die cavity, the flowability of the powders, and the feed shoe technology influence the filling density, which defines the initial state of material before the subsequent deformation.

At the very beginning of compaction, meanwhile the applied pressure increases, the powders can slide and rotate under elastic material condition. This densification mechanism, which does not involve particle shape changes, is commonly called rearrangement. When locally the stress field exceeds the metal yield strength, plastic

deformation grows in the contact zone and the relative movement and rotation between particles end. The increment of the plastic deformation determined the closure of the interconnect porosity and the hardening of the metal powder. Therefore, plastic deformation becomes the dominant densification mechanism, which is controlled by the hardening rule of metal powder material [9].

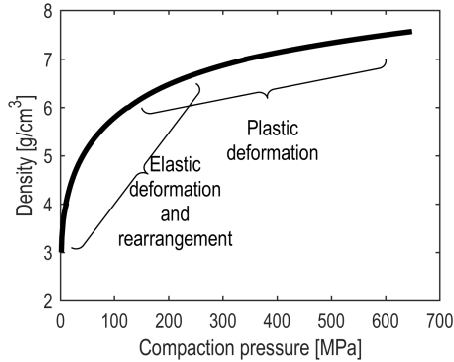


Figure 1.2. Green density vs. compaction pressure. Scheme of the densification mechanisms in uniaxial cold compaction [9].

In order to design the compaction process, it is necessary to know how powder mix evolves under uniaxial compaction. The property is called compressibility. Standard test method explains how to evaluate the compressibility of metal powders under uniaxial compaction [10]. Though standard gives a detailed procedure on the experimental set-up, it does not provide indication on the mathematical relationships to be used in order to fit pressure-density trend. For this reason, scientific community has developed a great variety of densification relationships over the years.

One of the most famous equations was proposed by Heckel in 1961 [11]:

$$\ln \frac{1}{1 - \rho_r} = KP + \ln \frac{1}{1 - \rho_{r0}} + B \quad (1.2)$$

Where:

- ρ_r is the relative density which is conventionally calculated by the ratio of the green density and the theoretical density of the powder mix,
- ρ_{r0} is the relative apparent density,
- P is the applied pressure,

- K, B are constants depending on fitting of experimental data.

Other relationships were reported in literature over the years [12–15]. Among them, the most relevant equations proposed in the in the last twenty years are following reported. Secondi [16] proposed equation (1.3):

$$\ln \left(\frac{\rho_{\infty} - \rho_r}{\rho_{\infty} - \rho_{r0}} \right) = -KP^n \quad (1.3)$$

Where:

- ρ_r is the relative density,
- ρ_{r0} is the relative apparent density,
- ρ_{∞} is the maximum relative density which can be reached by the activated densification mechanisms,
- P is the applied pressure,
- K, n are material constants which control the material hardening rule and plasticity at the macroscopic scale.

Parilak tested equation (1.4) for 205 different powder mixes [17].

$$\Theta = \Theta_0 \exp(-KP^n) \quad (1.4)$$

Where:

- Θ is the porosity,
- Θ_0 is the initial porosity when applied pressure is zero,
- P is the applied pressure,
- K, n are compaction parameters.

In 2015, Aryanpour et al. [18] proposed equation (1.5):

$$\ln \left(\frac{1 - \rho_{r0}}{1 - \rho_r} \right) = \ln \left(\frac{\frac{1}{Pa} - \frac{1}{ba}}{\frac{1}{ba}} \right) + KP \quad (1.5)$$

Where:

- ρ_{r0} is the relative apparent density,
- ρ_r is the relative density,
- P is the applied pressure,
- K, a, b are material parameters.

In 2017 Molinari et al. [19] [20] developed relation (1.6):

$$1 - \frac{\rho_0}{\rho_{situ}} = AP_m^B \quad (1.6)$$

Where:

- ρ_0 is the filling density.
- ρ_{situ} is the in-situ density,
- A, B are material constant,
- P_m is the mean compaction pressure.

In 2018 Montes et al. [21] proposed equation (1.7)

$$P = \frac{\sqrt{3}}{2} \left(1 - 2\mu_k z \frac{H_0}{D} \right)^{-1} k \left[\ln \left(\frac{1 - \Theta}{1 - \Theta_M} \right) \right]^n \frac{1 - \Theta/\Theta_M}{\sqrt{\Theta/\Theta_M}} \quad (1.7)$$

Where:

- P is the applied pressure,
- μ_k is the kinetic frictional coefficient,
- z is the radial to axial pressure ratio,
- H_0 is the initial height of powder column,
- D is the diameter of the die,
- k, n are material parameters,
- Θ is the porosity,
- Θ_M is tap porosity.

Comparing all the relationships previously reported, differences in the mathematical expressions and physical meaning of the constants can be highlighted. In a recent work, Cristofolini et al. compared the reliability of the densification laws proposed by Parilak, Aryanpour, Montes and Molinari in fitting experimental densification curve of AISI316L powder. The results showed some discrepancy between the experimental data and the derived fitting trend [22]. Looking at this result and at the number of densification equations proposed in literature, it is possible to conclude that a density-pressure relationship based on physical principles able to describe the powder compressibility is far away to be reached.

The major limitations of the densification relationships regard the boundary effect of the die cavity. In contrast to classical uniaxial tensile test, in confined uniaxial compaction, the stress is not homogeneous since radial and frictional forces are also

present in addition to axial force. In two distinct papers, Beiss [23] and Bocchini [24], explain that the geometry has an influence on frictional forces, and consequently on the axial force needed for reaching the desired green density. Therefore, densification equations generally do not correspond to the intrinsic material property.

As described in the standard, the compressibility curve, which is related to a specific geometry, can only offer a qualitative estimation of the compressibility of the powder mix, because these relationships fail in providing an accurate prediction of pressure and density in the compaction of complex structural parts [10, 25].

A precise description of the compaction mechanics of powder mix requires the knowledge of the triaxial state of stress, friction coefficients and green strength as function of green density. The green strength, which consists in the ultimate tensile and shear strength, should be known in order to develop a failure criterion for predicting crack formation.

Friction coefficients allow to know the interaction between powder and die cavity. Four types of frictional forces can be classified on powder compaction [26]:

1. Friction between punches and die wall,
2. Friction among particles (interparticle friction),
3. Friction between particles and die cavity,
4. Friction between compact and die wall under ejection step.

Among them, friction between powder mix and die cavity has the major contribution in compaction.

In order to evaluate the failure criteria of green compacts, literature suggests two failure tests:

- free compression test,
- diametral test [27, 28].

Due to the triaxial state of stress, friction interaction and failure criteria do not linearly depend on density, and the evolution of green density on compaction cannot be predicted by an analytical closed form equation. For this reason, different computer codes have been developed in order to solve this non-linear problem. It is possible to divide them in:

- Discrete element modeling (DEM)
- Finite element modeling (FEM)

- Multi particle finite element modeling (MPFEM)

These techniques offer support for investigating the PM process at different size-scale. DEM approach is recommended for simulating particles rearrangement when powders are assumed as rigid spheres governed by normal and tangential forces. The solution of Newton's second law equations provides the particles' position and velocity. This simulation process is useful for studying die filling or powder flowability, and compaction of metal and ceramic powders under elastic condition [29, 30].

In finite element approach, powder material is considered as a continuum. FEM would be implemented for simulating compaction at high relative density. A great variety of constitutive material models have been developed during years, assuming granulate material as a continuum medium. The most promising models for simulating metal powder compaction are: Green model [31], Shima-Oyane model [32], Gurson model [33], cam-clay [34–36], Ducker Prager cap model [37].

Generally, these models separate the elastic and plastic behavior of material. Elastic behavior is usually assumed isotropic and it is described by two material parameters: elastic modulus and Poisson coefficient, which are function of a state variable associated to relative density. In the same way, hardening material parameters are related to the density state variable. Only modified cam-clay model and Drucker Prager cap model include a failure condition for predicting crack formation. These constitutive models seem adequate to simulate the compaction process; however they require a high number of experimental tests in order to characterize the material properties. Unfortunately, the material parameters database, which is essential for designers, is quite poor. Another limitation regards the lack of a standard procedure for material characterization. In fact, several characterization methods are reported in literature, as it will be described in depth in section 2.2.

With relation to multi particle finite element modeling, a combination of DEM and FEM approaches could be considered. MPFEM seems particularly suitable for representing the overall compaction process, from die filling to plastic deformation of particles. The current drawback of this method involves the high computational time and resource required, which limit the real application.

1.2.3 Sintering

According to the ISO definition, sintering is a *thermal treatment of a powder or compact, at a temperature below the melting point of the main constituent, for the purpose of increasing its strength by the metallurgical bonding together of its particles* [38]. In other words, sintering provides the thermal energy which promotes the consolidation or the densification of metal structure with the consequent enhance of mechanical strength. If the increase of strength is an obvious target of sintering, the densification and the closure of porosity lead to undesired dimensional change, and in some cases to shape distortion.

At the beginning of conventional sintering thermal cycle, furnace is slowly heated up to 500-600°C (dewaxing process). During this stage, the decomposition of polymeric material begins at 150°C and usually ends around 550°C. High temperature induces the burn-off of polymer chains in carbon monoxide, carbon dioxide, water and so on. These gas molecules can easily flow out of compacts if dewaxing is properly managed. An excessive heating rate can produce cracks on compacts, which are caused by the volume expansion of gases.

In the sintering process of metal powder, the control of sintering atmosphere, as well as the control of thermal cycle, is crucial. Reducing or oxidizing atmospheres are carefully controlled in order to eliminate impurities (lubricant, oxide, moisture). In the effort of removing lubricant, oxidizing atmosphere enhances the dewaxing process. High hydrogen fraction determines the reduction of carbon residuals, which can detrimentally modify the chemical composition of metal parts [39]. After dewaxing, temperature is raised up and held for a certain time interval in order to activate the sintering densification mechanisms. For ferrous materials, conventional isothermal stage lasts 30 minutes at 1120°C. In order to guarantee the metal densification, reducing atmosphere is employed after dewaxing. By this way, oxide layer on particle surface is removed, promoting mass transport mechanisms. Therefore, reducing atmosphere is necessary, but it could determine undesired carbon loss from the surface. For this reason, after the isothermal stage, carburizing atmosphere may be introduced in order to restore carbon content. Secondary goal of carbon restoration regards the increase of carbon content on the surface for subsequent sinter hardening thermal treatment. Figure 1.3 shows the thermal stages, also related to different atmospheres, in a continuous furnace. In a modern system, separated chambers are designed in order to avoid interaction between the different gas mixtures. In batch sintering procedure, dewaxing and sintering are generally performed in two separate furnaces, in order to avoid that residual soot of dewaxing contaminates the sintering

process.

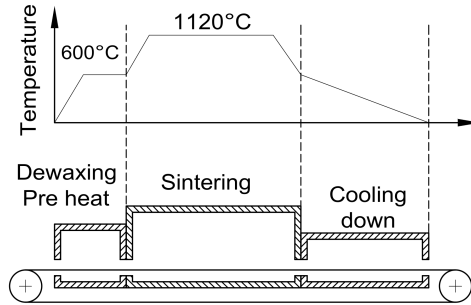


Figure 1.3. Temperature stages in the different positions of the continuous furnace.

Considering the physical aspects, sintering is a thermal treatment which promotes the material densification by the activation of diffusion mechanisms. The driving force of sintering is the reduction of interfacial energy $\Delta(\gamma A)$ which depends on specific surface energy (γ) and total surface area of compact (A) [40]. The variation of total surface energy can be expressed as:

$$\Delta(\gamma A) = \Delta\gamma * A + \gamma * \Delta A \quad (1.8)$$

As schematized in figure 1.4, the variation of total surface energy can produce the densification and/or the coarsening of particles.

Two main physical mechanisms can be distinguished in sintering: solid state sintering and liquid phase sintering. Solid state sintering occurs when metal powders are in solid state at the sintering temperature, whereas, in liquid phase sintering, both liquid and solid phases are present at the sintering temperature.

In solid state sintering it is possible to recognize three overlapped states, which modify the powder microstructure: initial stage, intermediate stage and final stage. The initial stage considers the necks formation between particles. The classical sintering theory models this stage by two spherical particles initially in point contact. The diffusion mechanisms produce the flux of atoms towards the contact region, and the further neck growth. On the intermediate stage the higher densification occurs in relation to the other sintering stages. The reason is ascribed to the progressive evolution of porosity, from open interconnected structure to some isolated voids. The densification of the open porosity system is classically described by channel pore model. Carrying on the sintering process, grains grow and the isolated pores dissolve.

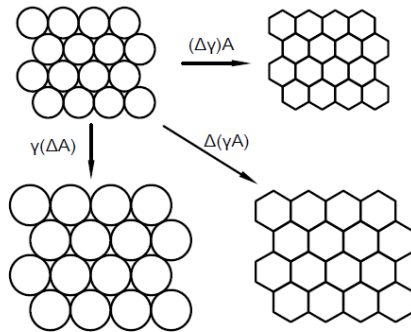


Figure 1.4. Scheme of the phenomena occurring on sintering promoted by the reduction of surface energy $\Delta(\gamma A)$ [40].

This is the final stage of sintering and is represented by isolate pore model [40].

The classical theory [41] and model [42] regarding liquid phase sintering propose three stages:

1. particle rearrangement by liquid flow,
2. contact flattening by solution and reprecipitation process,
3. solid state sintering.

In figure 1.5 an example of the densification, as a function of the sintering time is proposed for solid state sintering and liquid phase sintering, with special interest on the contribution of each stages on the overall densification.

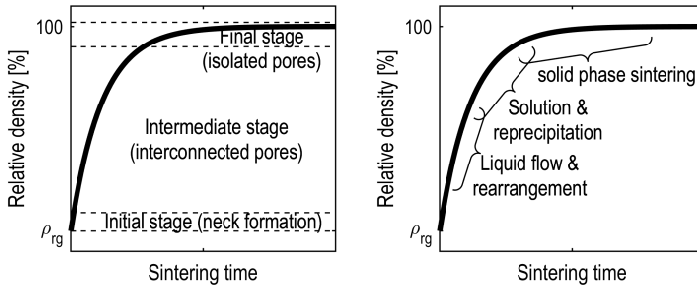


Figure 1.5. Schematic densification curve in solid state sintering on the left [40] and liquid phase sintering on the right [43].

Different kinetic equations have been developed for each stage of sintering. Classical sintering theory describes the densification process by diffusion mechanisms, occurring in a simplified system. For instance, the initial stage of solid state sintering is simplified by two spheres in point contact. Sintering activates some diffusion mechanisms, which produce a flux of atoms from convex to concave shape causing the neck formation and the further growth. The two spheres move closer, causing the shrinkage of the system. The shrinkage of the system can be expressed by equation (1.9).

$$\left(\frac{X}{D}\right)^n = \left(\frac{\Delta l}{l_0}\right)^{\frac{n}{2}} = \frac{B}{D^m} t \quad (1.9)$$

Where:

- X is the neck radius,
- D is diameter of the particle,
- $\Delta l/l_0$ is the macroscopic dimensional change,
- t is the isothermal sintering time,
- B, n, m depends on the diffusion mechanisms as reported on table 1.2.

Mechanisms	n	m	B
Viscous Flow	2	1	$3\gamma_s/\eta$
Plastic Flow	2	1	$9\pi\gamma_b D_v/kT$
Evaporation-Condensation	3	2	$(3P\gamma_s/\rho^2)(\pi/2)^{1/2}(MkT)^{3/2}$
Volume Diffusion	5	3	$80D_v\gamma_s\Omega/kT$
Grain Boundary Diffusion	6	4	$20\delta D_b\gamma_s\Omega/kT$
Surface Diffusion	7	4	$56D_s\gamma_s\Omega^{4/3}/kT$

Table 1.2. Summary of the main diffusion mechanisms involved on the neck growth at the initial stage of solid state sintering [44].

In addition to the classical equations for the sintering stages [39, 43, 45, 46], alternative models have been proposed in order to describe the kinetic of macroscopic dimensional change on sintering. Kingery and Berg [41, 47] modelled the linear shrinkage between two sphere-shaped particles by their center approach. The linear shrinkage is expressed by a power-law equation (1.10).

$$\frac{l_s - l_g}{l_g} = (kt)^n \quad (1.10)$$

Where:

- l_s is the sintered length,
- l_g is the green length,
- t is the sintering time,
- k, n are physical parameter of the kinetic process.

In 1961, Coble [48] developed a model based on the assembly of cylindrical pores situated along the edges of regularly polyhedral grains. In this model porosity has a logarithmic dependence on sintering time, as expressed in equation (1.11).

$$\Theta_0 - \Theta = k \ln \frac{t}{t_0} \quad (1.11)$$

Where:

- Θ_0 is the porosity at the beginning of isothermal sintering stage.
- Θ is the porosity,
- k are physical parameter of the kinetic process.

- t is the sintering time,
- t_0 is the time at the beginning of the isothermal stage,

In 1972, Skorokhod proposed a rheological approach [49] assuming viscous material behavior. In this model porosity evolves during the sintering process by equation (1.12)

$$\frac{\Theta}{\Theta_0} = (1 + kt)^{-n} \quad (1.12)$$

Where:

- Θ is the porosity at time t ,
- Θ_0 is initial porosity of sintering process equal to the green density,
- t is the sintering time,
- k, n are physical parameter of the kinetic process.

In 1975, Kuczynski proposed a statistical theory [50–52] which provides a shrinkage kinetic law similar to equation (1.12).

As stated by Exner in [53, 54] these shrinkage kinetic equations lack for a solid theory which considers the mechanisms occurring on sintering. Despite this limitation, the proposed equations can fit very well the experimental results.

In the recent years, Molinari et al was working on the development of a kinetic equation based on physical metallurgy principles [55–57]. In some recent works [58, 59], the kinetic of linear shrinkage is expressed by (1.13).

$$\frac{l_s - l_g}{l_g} = -2G \left[D_a \frac{\gamma \Omega}{k_b T} t \right]^e \quad (1.13)$$

Where:

- l_g is the green length,
- l_s is the sintered length,
- G, e are constant which depends on geometry of the contact region,
- D_a is the bulk diffusivity,
- γ is the surface tension,
- Ω is atomic volume,
- k_b is the Boltzmann constant,
- T the absolute isothermal sintering temperature,
- t is the isothermal sintering time.

For the reason explained by Exner, in most of the cases kinetic shrinkage equations suffer poor theoretical background, since they are the result of purely fitting operations. In addition, the kinetic equation has poor practical interest from engineering perspective, since it does not provide an effective tool for predicting shape distortion of complex geometry and the resulting microstructural evolution in practical sintering operation. Due to these limitations, computer aid approaches have been developed in the last years in order to simulate the sintering process as for powder compaction. As summarized by German, the simulation techniques can be sorted on the basis of relevant scale of the problem [43].

Atomistic model simulated the atomic interaction. Usually clusters of atoms are assembled in one to three powders. By the introduction of the material parameters and the boundary condition of time-temperature relation, some properties can be extracted, such as: elastic modulus, melting temperature, thermal expansion coefficient. Attempts were conducted to predict macroscopic dimensional change through the simulation of the neck growth of spherical particles based on the volume and grain diffusion mechanisms [60, 61]. Despite some accordance between simulations and experimental results, atomistic model seems not be suitable for predicting macroscopic dimensional change on sintering.

Monte Carlo approach simulates probabilistic events as atoms movements. In comparison of atomistic model, Monte Carlo method approximates material at bigger scale of grains. For this reason, it is particularly suitable for modeling grain growth, grain coalescence, and pore-grain interaction [62].

As used for modeling powder compaction, discrete element (DEM) and finite element modeling (FEM) represent the most promising techniques for the prediction of dimensional change of complex geometry. As for compaction, DEM approach consists in the assembly of rigid particles. Particles are governed by an interparticle contact law and after the application of boundary conditions, the commercial code solves the equation of motions in order to predict the particles positions. Considering sintering simulation, adequate contact law should be introduced. An example of contact model was postulated considering the grain boundary and surface diffusion as the mass transport mechanisms originating the normal and tangential forces [29, 63, 64].

In FEM approach, a material constitutive law must be defined in order to simulate sintering dimensional change. The most widespread constitutive model assumes a non-linear viscous material behavior. The viscous model was originally developed by Skorohod [65] and successively introduced in FEM code by Olevsky [66]. Olevsky supposed that the strain rate can be linked to the sintering stress by the material

constitutive law expressed by equation (1.14).

$$\sigma_{ij} = \frac{\sigma(W)}{W} \left[\varphi \varepsilon_{ij} + \left(\psi - \frac{1}{3} \right) \dot{\varepsilon} \delta_{ij} \right] + P_L \delta_{ij} \quad (1.14)$$

Where:

- σ_{ij} are the component of stress tensor,
- $\frac{\sigma(W)}{W}$ represents the generalized viscosity,
- $\sigma(W)$ is the effective stress,
- W is the equivalent effective strain rate,
- ε_{ij} are the component of strain rate tensor,
- φ is the normalized shear viscosity, which depends on porosity,
- ψ is the normalized bulk viscosity, which depend on porosity,
- $\dot{\varepsilon}$ is the first invariant of the strain rate tensor,
- δ_{ij} is the Kronecker operator,
- P_L is the Laplace pressure.

Unfortunately, in current use, constitutive parameters (sintering stress, bulk and shear viscosity) are obtained from analytical solution of highly simplified grains and pore structure [67]. Usually these analytical solutions are calculated considering the evolution of unit cell of packed spherical particles with a pore in the center. As recognized by the author self, the major limitations of this model concern the determination of material parameters [67]. In addition, the model needs for the development of constituent parameters based on macroscopic experimental results.

In the last years, Johnson [68] introduced the concept of master sintering curve which has been also carried on by other authors [69–71]. This alternative approach would provide a quantitative result of the dimensional change independently on the thermal cycle. On sintering, the resulting dimensional change is strictly dependent on the thermal path. Therefore, a variation in the heating rate, temperature, and time of isothermal stage, produces a different densification result. The formulation of the master sintering curve expressed by equation (1.15) allows the prediction of the densification at any time-temperature sintering profile.

$$O(t, T(t)) = \int_0^t \frac{1}{T} \exp\left(-\frac{Q_a}{RT}\right) dt \quad (1.15)$$

Where:

- O is a dimensionless parameter which depends on the time-temperature profile,
- t is the sintering time,
- T is the absolute temperature,
- Q_a is the activation energy,
- R is the gas constant.

The master sintering curve seems suitable for the optimization of the sintering process, as well as for the research of the thermal path which guarantees the densification requirement. However, at the moment this model is only adequate for predicting isotropic dimensional change. In fact, master sintering curve does not deal for the possible anisotropy of dimensional variation and the shape distortion. For this reason, further development is needed in order to adjust this strategy for predicting the complex dimensional change of P&S parts.

In conclusion, alternative approaches have been developed in order to predict the microstructural and dimensional change on sintering. These models provide a quantitative estimation which is still not good enough for the industrial purpose. The main reason is clearly the high complexity of the sintering process. Further researches should investigate deeply the interaction of different phenomena which influence material evolution.

1.2.4 Secondary operation

At the end of sintering process, parts can be post worked for different scopes. Without entering the details, secondary operations aim at:

- increasing mechanical strength (hot forging, double press double sintering, impregnation, heat treatment, sinter hardening).
- modifying the shape or making hole not allowed by uniaxial press and sinter (drilling).
- adjusting the shape and tolerance (sizing).
- modifying the surface by the closure of porosity (densification, coining) or increasing hardness (surface treatment, steam treatment).

1.3 Dimensional precision of sintered part

A manufacturing process can guarantee the production of nominal dimensions within certain limits. The deviation of actual dimension with respect to nominal dimension is characteristic of the process and it is defined as the process capability. A standard method for evaluating dimensional precision is defined by ISO IT tolerance classes, whose reference is UNI EN 20286-1:1995 standard. The standard individuates tolerance grades based on normalization of nominal dimension intervals and dimensional deviation. Low IT values correspond to high precision (low deviation from nominal dimension) whereas high IT values is associated to poor precision (large deviation from nominal dimension). P&S is an effective technology able to produce components within tight tolerances. A comparison of the IT grades attainable in several shaping technologies is shown in table 1.3.

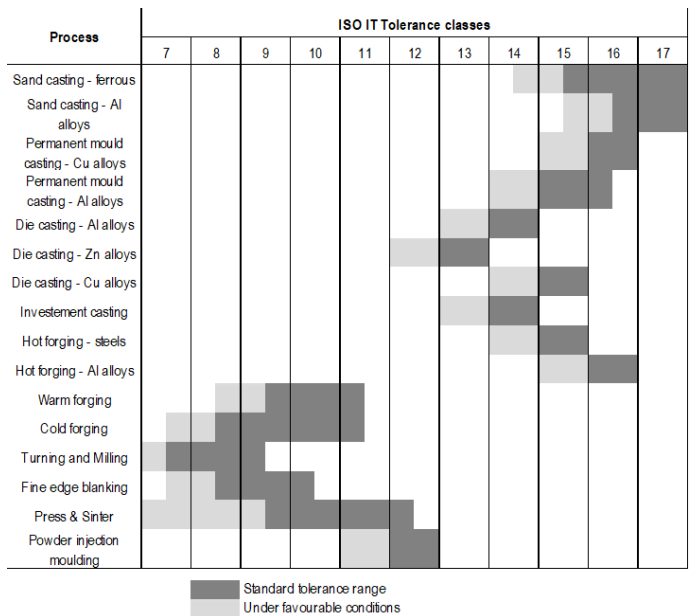


Table 1.3. ISO IT tolerance classes attainable for different shaping technological processes [72].

On the basis of table 1.3, the dimensional tolerances of sintered parts fit IT9-IT12

grades. The tolerance range slightly changes if other literature references are considered. Shatt and Witers [73] reported a worst range between IT12-IT15 for conventional press and sinter. Assinter manual [74] indicated that IT8-IT9 are attainable for dimensions perpendicular to the compaction direction. On the basis of author's experience, IT8-IT10 interval is achievable in as-sintered structural parts. An improvement of tolerance grade can be reached by secondary operations. Sizing, calibration, repressing and machining provide better accuracy in spite of an increase of the production cost. On the other hand, sometimes secondary operations are necessary in order to satisfy the tolerance requirement not guaranteed by the P&S capability. Moreover, secondary processes are also employed to amend errors due to the design of the process.

The tolerance grade is directly connected to the capability of the P&S process. Firstly, there is an influence of the powder supply chain. A deviation in the powder mix in terms of: particle size, lubricant content, powder morphology, segregation of powder and lubricant determines further fluctuation in the final sintered dimensions. Both compaction and sintering process influence the accuracy and scatter of sintered dimensions. The compaction process capability is excellent in compaction plane (diameters), whereas it is worst in compaction direction (heights). On compaction some aspects contribute to the deviation from desired nominal dimensions. These aspects are: the inhomogeneity in die filling, discrepancy of concentric punches and inhomogeneity in green density, elastic deformation of punches and die cavity.

The sintering process capability is dramatically lower in comparison with compaction process. This inferior capability of the sintering process is caused by the dimensional change. In particular, the deviation of the sintered dimension from the nominal one is caused by an erroneous prediction of the absolute dimensional change and the scatter between parts [39]. The scatter on sintering dimensional change is a consequence of superposition of all the inhomogeneities occurred from powder production to sintering practice. For instance, variation in the mean density, scatter of part weight, fluctuation in the compaction force can be observed in compaction, whereas inhomogeneity in the heating rate, temperature gradient, gas flux can be observed in the sintering furnace. Thus, the scatter of sintered dimensions is an intrinsic result of the technology, almost impossible to be avoided. On the contrary, the discrepancy between predicted and actual dimensional change can be ascribed to the design procedure. The design of the sintering process faces on the difficult prediction of the anisotropy of dimensional change. Generally, a higher dimensional variation is commonly observed in compaction direction, with respect to the compaction

plane. This variation affects the tolerance range; diameters present a better precision compared to height. Since height suffers a lower control both on compaction and sintering process, the associated tolerance is worst of 1-3 IT grades with respect to diameters. Therefore, the wide tolerance capability associated to P&S process shown in the table 1.3 is a result of the different accuracy attainable for diameters and height. In conclusion, according to German, dimensional control on sintering is one of the large barriers to expand PM market [39].

1.4 Dimensional variation on sintering

Thanks to the mass transport mechanisms activated by the sintering thermal cycle, consolidation or densification of metal structure occurs. Consolidation slightly affects the dimension of green parts, whereas densification generally determines a more noticeable volume variation. Since consolidation generally does not guarantee sufficient mechanical resistance of structural parts in common production operation, the sintering time-temperature cycle is optimized in order to activate the densification mechanisms. Densification provides the strengthen of compacts, but it causes also an increase or decrease of the volume with comparison to the green state. A volume expansion is observed when liquid state sintering occurs [75], whereas the solid state sintering determines a reduction in volume. If both solid state sintering and liquid phase sintering are activated, the resulting volume change is a balance of the two mechanisms. In addition to the influence of sintering mechanisms, the amount of volume change depends on:

- the material. The presence of low melting alloy causes the liquid formation and the sintering is assisted by liquid phase sintering. A variation in the particle size and particle shape correspond to a different specific surface area, and consequently a different volume change.
- The process conditions, as well as the sintering temperature and time, have a clear influence. Increasing the sintering time and temperature determines higher dimensional variation, being the temperature prevailing parameter compared to the time.

The volume change is related to linear dimensional changes. In P&S, it is well known that the dimensional changes are not isotropic. In fact, the experimental measurements showed the different dimensional change in the compaction direction

(axial direction) and in the compaction plane (radial direction). Figure 1.6 displays typical experimental measurement of the dimensional change on a sintering thermal cycle by means of dilatometry. In the example, the dimensional change of height and diameter of a cylindrical sample made of atomized iron powder is reported. Meanwhile temperature increases, both height and diameter expand because of thermal expansion. Before the isothermal stage, alpha-gamma transformation produces a volume contraction. Then dimensions shrink during isothermal stage because sintering densification mechanisms are active. In this example, at the end of sintering cycle, the dimensional change of height is higher than the dimensional change of diameter.

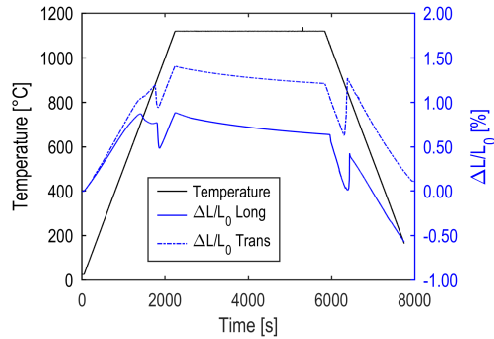


Figure 1.6. Dimensional variation of height and diameter of cylindrical sample versus the sintering temperature profile [58].

The example in figure 1.6 represents the typical situation encountered in solid state sintering, but literature reports some cases of inverse trend, where diameter shrinks more than height [76–78].

Unexpected dimensional changes are also encountered in liquid phase sintering, so, generally speaking, the anisotropy of dimensional change cannot be predicted a priori, since it is a complex phenomenon influenced by a high number of parameters.

1.5 Theory and model of anisotropy of dimensional change

As mentioned above, the anisotropy of dimensional change can dramatically affect the P&S process capability, if it is not properly managed and predicted. When the dimensional variation and shape distortion is not controlled, secondary operations are needed in order to adjust the dimension inside the tolerance limits. These additional operations should be avoided since P&S loses the competitiveness guaranteed by the economic advantage. For this reason, the effective prediction of the dimensional change on sintering is a fundamental aspect for the perspective of P&S. This objective can be reached by previous comprehension of the origin of anisotropy of dimensional variation.

The scientific community agrees that prior uniaxial cold compaction plays a central role in the origin of anisotropy of dimensional change observed on sintering. The compaction process extensively changes the particle arrangement, shape and material structure with respect to the powder as-built state. As introduced in section 1.2.2, rearrangement, elastic and plastic deformation are the densification mechanisms active at different density stages. Rearrangement causes a change of the particle coordination by means of reorganization in powders configuration under elastic material condition. On the contrary, plastic deformation determines shape change and hardening of metal powders. These densification mechanisms occur under anisotropic stress field because the axial stress is higher compared to the transversal one. Therefore, inhomogeneity can be introduced in: powder rearrangement, particle deformation and metal hardening.

In order to investigate the influence of compaction process and the related densification mechanisms on the origin of anisotropic dimensional change, ceramics powder is firstly analyzed. Anisotropy of dimensional changes is also observed in ceramic powders. However, on compaction there are some differences between ceramic and metal powders. Ceramic particles do not present plastic deformation because rearrangement is the only densification mechanism activated. For this reason, the study of ceramics provides information on the influence of rearrangement on the anisotropy of dimensional change on sintering, excluding plastic deformation and material hardening. Some theories suppose that the anisotropy of stress field on compaction causes a preferential orientation of ceramic particles and a gradient on particles distribution along the axial and radial direction. An experimental correlation between such compaction inhomogeneities and the anisotropy of dimensional variation is verified in some papers [79–81]. For instance, Sui et al. compared the sintering deformation of two alumina powders: a spherical and an elongated one [82]. Both

powders are uniaxially cold compacted and then sintered meanwhile the dimensional change was measured by dilatometer test. Compacts made of spherical powders did not present anisotropy on sintering, whereas elongated particles showed an aligned orientation due to compaction and larger shrinkage in height than in diameter. Consequently, it was concluded that in a system of elongated particles, aligned in preferential direction, the shrinkage is higher in the direction normal to the alignment. Evidences support the hypothesis that oriented particles originate anisotropy on sintering of metal powders. In metal injection moulding metal particles are not plastically deformed, but powders can be aligned in preferential direction during forming process, determining an isotropic dimensional variation for spherical particles and slightly anisotropic dimensional variation for particles with higher aspect ratio [83, 84]. Another similar result can be noticed on cold isostatic pressing process (CIP), where metal powders are hydrostatically deformed. In this case, metal powders do not exhibit preferred orientation after compaction, neither slight anisotropy on sintering [55].

In uniaxial metal powder compaction, particles are plastically deformed. As a result, the powder particles are aligned in the as-compacted state. This result is confirmed by Zavaliangos et al., compaction of sphere-shaped particles is modeled and final elliptic shape with the major axis perpendicular to compaction direction is predicted [85]. Therefore, there is coherency to what observed on ceramics material. However, the inhomogeneity of particle deformation does not completely explain the origin of sintering anisotropy in all the cases. Experimental analysis showed a double scenario. Though the dimensional variation in the compaction direction is generally higher than in compaction plane, some experimental analysis showed opposite results [86]. Some authors supposed that the entity of the applied stress controls the higher radial than axial shrinkage at low density, and the opposite occurs at high density [87–89]. An alternative explanation was proposed by Kuroki, who suggested a correlation between the elastic recovery during ejection and the sintering shrinkage [90]. Going into detail, Kuroki supposed that particle contacts open along axial direction as a consequence of the unloading of part during the ejection stage. The experimental results showed a correlation between the elastic recovery (springback) and the dimensional variation during sintering. In particular, the inhomogeneity of springback on radial and axial direction produces a gap in particle's contacts, which is proportional to the anisotropy of sintering dimensional change [91].

A milestone in the research of the causes of anisotropy of dimensional change in powder metallurgy is represented by the in situ observation of sintering of metal powder compacts by means of microtomography technique [92, 93]. In these papers

the microstructural evolution was directly measured during sintering thermal cycle. The microtomography measurements on prior cold compacted samples confirmed the presence of anisotropic shape and orientation of particles and pores. The image analysis of pores on 2D sections at different levels showed two type of pores: big pores called “cusped pores”, which are originated by particle packing, and “elongated pores”, which are small pores at the particle interface. In the cited papers, authors supposed that elongated pores are created during sample ejection. The elongated pores showed a preferred orientation of the major axis of elliptic pores along the compaction plane compared with packing pores.

The analysis of microstructure during dewaxing stage showed that elongated pores open along particle contacts due to the gas flow out. The pores opening produces a swelling along axial direction. Approaching to the isothermal sintering temperature, the elongated pores rapidly heal causing a significant shrinkage in axial direction, whereas cusped pores shrink without change in shape at 1120°C. Another microtomography in-situ analysis was performed on copper particles compacted by cold isostatic pressing (CIP). The analysis of microstructure showed that both particles and pores do not present preferential orientation and shape, both as-compacted and during sintering, isotropic shrinkage occurs in all the direction. Unfortunately, experimental microtomography observation has not performed yet on samples showing higher dimensional change in radial direction compared with axial direction. However, the microtomography images corroborate the Kuroki ideas of interparticle opening after unloading.

The above literature review evidences that uniaxial cold compaction gives rise to the origin of anisotropy of dimensional change on sintering. Uniaxial compaction process causes a microstructural change in compacts, which determines elongated particles and pores aligned within the compact. In most of the cases, higher dimensional variation occurs in compaction direction than in compaction plane. The compaction but also ejection has a role in the origin of anisotropic dimensional changes, and can explain the inverse anisotropy observed in some cases.

Up to now, experimental evidence and theories related to the anisotropy of dimensional change are reported. Two main theories currently aim at predicting the anisotropy of dimensional change on the basis of the microstructural inhomogeneity of green compacts. German and Olevsky focus their attention on the elliptic shape of pores, whereas other research groups are focused on the geometry and structural activity of particles.

German initially supposed that uniaxial cold compaction might have flattened pores from an irregular to an elliptic shape, whose major axis is aligned in the compaction plane [39]. During sintering, pores round with consequent shrinkage in the compaction plane and swelling in compaction direction. The explanation proposed by German has no univocal experimental evidence. As reported in section 1.4, some experimental analyses measured shrinkage both in axial and radial direction, being absolute ratio lower or higher than 1. An improvement of German theory on the influence of pore shape on the anisotropy of dimensional change was proposed by Olevsky [66, 94, 95]. The as-compact microstructure is schematized by skeleton (metal material) and inclusions (voids). In this micromechanical model, voids are simplified by an elliptic pore surrounded by particles, as shown in figure 1.7.

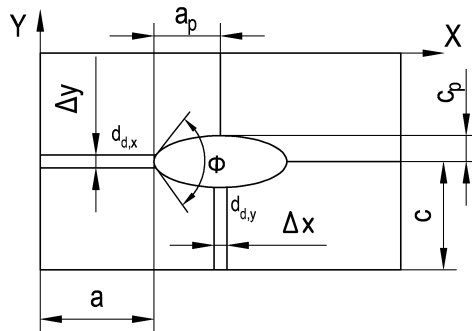


Figure 1.7. Micromechanical model of the porous material structure [96].

According to this theory, the anisotropy of dimensional change depends on two aspects: the Laplace stress tensor and the material constants. With relation to different radii of curvature of the ellipsoidal pore, the Laplace stress component changes. In addition, the curvature of the elliptic pores determines the anisotropy of the material response in terms of viscous material constants. An analytical formulation of the effective strain rate in x ($\dot{\epsilon}_x^{f,s}$) and y direction ($\dot{\epsilon}_y^{f,s}$) is expressed by equations (1.16) and (1.17), respectively [96].

$$\begin{aligned} \dot{\varepsilon}_x^{f,s} = & -3 \frac{D_v \left(1 + \pi r_p^2 d_{d,y} \frac{D_p}{D_V} \right) \Omega}{k_b T \delta} \gamma_{sv} * \\ & * \frac{S_p/2}{c(a+a_p)(c+c_p)} \left[\frac{1}{r_c} - \frac{1}{c} \sin \left(\frac{\phi}{2} \right) \right] \end{aligned} \quad (1.16)$$

$$\begin{aligned} \dot{\varepsilon}_y^{f,s} = & -3 \frac{D_v \left(1 + \pi r_p^2 d_{d,x} \frac{D_p}{D_V} \right) \Omega}{k_b T \delta} \gamma_{sv} * \\ & * \frac{S_p/2}{c(a+a_p)(c+c_p)} \left[\frac{1}{r_a} - \frac{1}{a} \sin \left(\frac{\phi}{2} \right) \right] \end{aligned} \quad (1.17)$$

Where:

- D_v are the coefficient of volume and pipe diffusion,
- r_p is the pipe radius,
- $d_{d,x}, d_{d,y}$ are respectively the dislocation densities along x y directions,
- Ω is the atomic volume,
- δ is the interparticle boundary thickness,
- γ_{sv} is the surface energy,
- S_p is the surface area of the pore,
- a, c are the semicontacts of particles along x and y directions,
- a_p and c_p respectively the major and minor semiaxis of the ellipsoidal pore,
- r_a and r_c are the effective radii of curvature of the ellipsoidal pore,
- ϕ is the dihedral angle.

As mentioned in section 1.2.3, Molinari et al. is working on a kinetic shrinkage equation starting from the classic kinetic equation of neck growth [45]. As in Olevsky model, equation (1.13) relates the anisotropy of shrinkage to the anisotropy of bulk diffusivity and microstructure. The anisotropy of diffusion coefficients is a result of the hardening of metal powders, and the origin of preferential pipe diffusion mechanism. Olevsky identifies a geometrical model of green microstructure centered on the oriented ellipsoidal pore, while this alternative theory focuses on a geometrical model of particles anisotropically deformed after compaction [55–59].

The classical kinetic equation of sintering is based on a geometrical model constituted by two spheres in an initial point contact. On the contrary, this new approach proposes an initial contact extension due to the plastic deformation occurred

during compaction process. Since the triaxial state of stress is not isotropic, longitudinal contacts are higher compared to transversal contacts, owing to the higher stress in compaction direction.

Both theories are deeply physically related to the experimental evidence of sintering procedure. However, both of them do not provide an effective tool for the prediction of the anisotropy of dimensional change, mainly due to the lack of a database of material parameters. In fact, both methods require a deep characterization procedure in order to derive the material parameters related to microstructure characteristic as: grain and bulk diffusion coefficient, bulk and shear viscosity, particle contact length and so on. For this reason, the two theories are currently not attractive for P&S design procedure and trial and error still remains the most frequently used approach.

1.6 Aim of this work

The present thesis would introduce two possible alternative approaches for the prediction of the anisotropic dimensional change on sintering. The first approach is reported in part A. As mentioned above, both triaxial stress field and ejection procedure can influence the anisotropy of dimensional variation. This study would be a first tentative to correlate the anisotropy of the stress field and the dimensional variation on sintering. This analysis would lay the foundation for a new design procedure of P&S process, which considers the evolution of material from compaction to sintering by means of macroscopic properties easy to be measured than microscopic properties.

In part B an alternative prediction method accounting for anisotropic dimensional variation is tested. This method was previously developed by a collaboration between industrial and research partners. This design procedure is based on a database experimentally derived, measuring the anisotropic dimensional change on sintering of samples made of different materials, and pressed and sintered in different conditions. In part B this design method is validated on real industrial parts, within an EPMA Club Project involving the major European P&S companies.

The method proposed in part A has a deeper physical background, while the design method in part B provides an easy and effective design procedure for the manufacturing process.

2 Part A: Influence of compaction on the anisotropy of dimensional change

2.1 Introduction

This study investigates the influence of uniaxial cold compaction on the origin of anisotropic dimensional change on sintering through an experimental approach: ring-shaped samples were compacted by an industrial press and then sintered in a batch furnace. Samples were labeled and tracked from compaction to sintering. Moreover, different geometries and different powder mixes were considered, to distinguish the influence of material and geometry from the influence of stresses in compaction. During compaction process, forces and displacements were continuously recorded by the press, and served as the basis to derive compaction mechanics relationships for the powder mixes. The dimensions of ring samples were measured in the green and sintered state by a coordinate measuring machine (CMM). By the method presented here, a direct comparison between the inhomogeneity of stress field during prior cold compaction and the anisotropy of dimensional variation on sintering can be evaluated.

2.2 Experimental procedure (Materials and Methods)

In this work, three aspects influencing the anisotropy of dimensional change have been studied: the geometry, the material and the stress field occurred during compaction process. The aim of this study is to separate the contribution of each of them.

Ring geometry was selected since the axisymmetric parts are the most widespread in P&S products¹. In literature ring geometry is poorly investigated, with respect to cylindrical shaped samples, while rings are more representative of the real geometry of industrial parts. Cylindrical samples are usually preferred because they require a simpler compaction equipment compared to ring shape, in addition the mathematical description of stress state and dimensional change of cylinders is easier than that for rings.

¹Further explanation of the choice of ring geometry can be found in part B section 3.3.

AISI 316L austenitic stainless steel is the material used in this work. This material is suitable for studying the sintering dimensional change since:

- solid state sintering is the only densification mechanism active during sintering cycle;
- 316L does not present alpha-gamma phase transformation. Conventional steels display phase transformation on heating and cooling stages of sintering cycle. Specifically, on heating the alpha to gamma transformation produces a reduction of volume, which must be subtracted from the dimensional change induced by densification mechanisms. During the cooling stage, austenitic phase evolves in a microstructure depending on the cooling rate. The formation of different microstructural components determines a dimensional change, which is hard to be separated from the dimensional change induced by sintering.

It is necessary to remind that stainless steel has some negative properties such as:

- poor compressibility on compaction. Chromium and nickel determine solution hardening, which strongly reduces the maximum reachable green density.
- critical sintering operation. Since chromium forms stable oxide layer on powder surface, the sintering operation requires vacuum furnace or strong reducing atmosphere (high H_2 content) in addition to high sintering temperature for reducing the oxide layer and promoting sintering mechanisms. This requirement complicates the sintering process and might cause negative consequence on the effectiveness and the production rate.
- high dimensional change on sintering. Generally stainless steel encounters higher shrinkage than other iron based powder mix. If high shrinkage is not properly managed in design procedure it could damage the final tolerance.
- selective corrosion. Even if stainless steel is usually chosen for its corrosion resistance, P&S might suffer of poor corrosion resistance in presence of interconnect porosity. In addition, the corrosion resistance decreases on increasing oxygen content in sintered part.
- market usage. The cost of austenitic stainless steel is one order of magnitude higher than conventional iron based powder mix. For this reason, the market of stainless steel for P&S product is limited.

The influence of particle size was investigated. Commercial 316L stainless steel was provided by Höganäs AB. A fraction of the total amount was sieved in 3 particle

sizes: lower than 45 μm (45), bigger than 90 μm (90) and the intermediate one (45-90). Acrawax lubricant was mixed to the three particle sizes and to the standard powder, up to the 0.6% of weight. Each powder mix was carefully shaken to homogenize the lubricant distribution and limiting the segregation of particles.

Powder mixes were sieved, mixed and shaken by Sacmi Imola S.C. company group² which also provided an industrial press for the compaction operation. The compacting equipment consists in a 200 tons hydraulic press with nine independent movement axes. A die with a cavity of 35 mm, corresponding to the external diameter of the ring sample, was mounted on the press. A core-rod of 15 mm diameter was used for creating the internal hole of the ring sample. Since no alternative die was available, all the samples have the same internal and external diameters. However, in order to investigate the influence of geometry on dimensional change on sintering, samples were compacted at different height.

Samples were compacted by single action cold compaction strategy, as explained in section 2.3, although double action compaction process is the conventional process in industrial application.

During the compaction of each sample, the control unit of the press collected data of the forces acting on upper punch, die and core-rod, and the related displacements. No extra measuring devices were mounted on the press.

Table 2.1 reports the number of samples produced in different geometries and particle sizes.

geometry	Standard	<45	45-90	>90
H/2T=0.25	3	/	/	/
H/2T=0.50	3	3	3	3
H/2T=1.00	3	/	/	/
H/2T=1.50	3	3	3	3
H/2T=2.00	3	/	/	/

Table 2.1. List of samples compacted at different geometries (expressed by height (H) to double thickness (2T) ratio) and particle sizes.

The samples were compacted at the green density of 6.6-6.7 g/cm^3 . The density was measured by the water displacement measurement in a second step.

After compaction, green rings were carefully transported from Sacmi plant to the

²Sacmi is an Italian company, leader in press design and manufacturing for metal and ceramic compaction.

University of Trento for the measurement of dimensions. The dimensions of green parts were measured by means of a coordinate measuring machine (CMM). The CMM is a DEA Global image 07-07-07 which is equipped by a continuous scanning head SP600 Renishaw with an accuracy of $3.4/120 \mu\text{m/s}$ according to ISO 10360-4 [97]. The measurement head mounted a stylus having a nominal length of 100 millimeters ending with the probe, a ruby sphere 8 millimeters diameter. This measurement configuration was accurately selected in agreement with the:

- sample geometry and the features to be measured;
- the position of the sample on CMM working plane;
- stylus assembly guideline [98].

The clamping system of ring-shaped samples is shown in figure 2.1. A mandrel was fixed to the working plane of CMM. Over it, a plastic holder was placed to support the sample by a concave surface having the same curvature of the external diameter of the ring. In this way the operator was helped aligning the samples in a more reproducible way. The sample was constrained by two blocks with a triangular boundary edge, moving on a linear guide by means of a torsional screw. A limited force was applied in order to prevent the damaging of green parts.

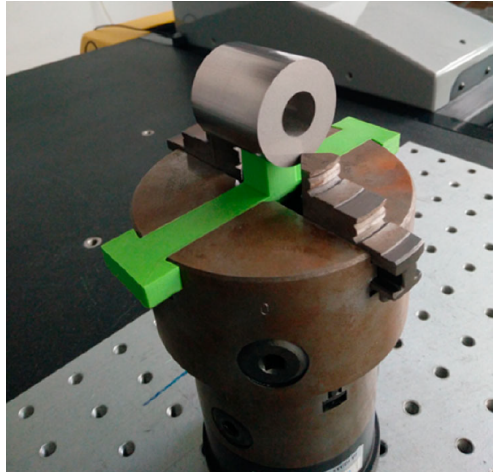


Figure 2.1. Example of the clamping system of ring sample.

This clamping configuration guarantees an optimal access to all sample surfaces. Internal hole diameter can be scanned completely, whereas planes and external diameter can be scanned in an angular interval of 280° , due to the shadowed zone close to the clamping system.

The measuring procedure routine used for all the samples was programmed in PC-Dmis 2016 software suite. The routine initially identifies the datum reference frame of the sample, which is following aligned to the machine reference system. The datum reference frame on the sample is identified by the bottom plane of the ring and the internal axis of the hole. In this work the bottom plane corresponds to the ring plane in contact with the lower punches during compaction. Bottom plane instead of upper plane (plane in contact with the upper punch) was chosen depending on its better flatness measured in previous experimental campaign [99]. In addition, shape distortion is sometimes observed in the upper plane, as a consequence of inhomogeneous filling.

In the alignment procedure, both bottom plane and hole axis were reconstructed by a complete circle scan³. The angular position corresponding to the clamping system was marked in order to scan the sintered sample exactly in the same position of the green sample.

³The external diameter can be scanned in a limited angular range; therefore, it is not suitable for the part alignment.

After part alignment, bottom plane was scanned by a complete circle scan at the diameter of 28 mm and by a partial circle scan at the diameter of 32 mm. The points acquired were filtered out the values outside the 3σ interval of the normal distribution. The remaining points were fitted by a least squares method for the bottom plane reconstruction. The top plane was reconstructed in the same way. The use of two scans provides a high number of points, which can be used for the plane reconstruction, and moreover, the scans at two diameter levels give information on the shape of the surface and the possible presence of distortion.

When both bottom and upper plane were derived, the height of the sample was calculated by the distance between the planes. After height measurement, the external and internal diameters were scanned at 1/4, 1/2, 3/4 of the measured height. The cloud of points of the three external scans was used for the cylinder reconstruction by least squares best fit. The diameter of such cylinder corresponds to the mean external diameter of the ring. In the same way, internal diameter of the ring is derived. Internal and external diameters scanned at three height positions also highlighted the effect of compaction on local shape of the sample.

All the green samples were measured and marked by an ID number, then they were delubed at 600°C for 24h in a batch furnace. On sintering, samples were heated at the speed of 10°C/min from the room temperature to 1250°C followed by an isothermal holding of 60 minutes before cooling down. The sintering furnace is under vacuum condition during heating with a nitrogen backfilling above 900°C. Finally, the sintered rings were measured adopting the same strategy developed for the green parts.

2.3 Compaction mechanics

In this section, the assumptions and relationships which describe the compaction mechanics and the material densification behavior are presented. This analysis aims at determining the triaxial state of stress occurred during compaction.

In the literature different methods to characterize the compaction mechanics of porous materials are described. Each different approach aims at measuring the triaxial state of stress while sample is under compaction. Basically, the characterization tests measure:

1. the displacement of punches in order to know the actual sample height and volume during compaction.

2. Axial force applied by punches and radial force caused by die constraint in order to deduce the triaxial state of stress.
3. Friction coefficients of the powder mix against the die cavity.

Axial force can be quite easily determined, while radial stress is hard to be derived. For this reason, different solutions are reported in the literature for measuring both axial and radial stress. The most promising ones are:

- triaxial test equipment [100–102],
- cylindrical die with instrumented sensors which estimate the radial stress by means of:
 - force transducer [103–105]
 - strain gages [104, 106, 107]
- instrumented cubic die formed by separate plates with a force transducer on longitudinal and transversal direction [108, 109] .

In addition to these experimental approaches, other characterization methods estimate the radial stress by recursive algorithms calibrated on the force/displacement curve measured in compaction [110, 111].

The friction coefficient can also be determined, when the radial stress acting on the die is measured, evaluating the fraction of axial force transmitted to the die due to friction. In addition to instrumented die equipment, there are specific tests designed for measuring the friction generated by powder mix against surfaces. They are:

- Stribos apparatus [112],
- shear-plate technique [113],
- Cameron plint tribometer,
- Jumping ball,
- Ball on disc.

Except for shear-plate technique, other methods were not considered suitable for representing the tribological condition in uniaxial cold compaction by European PM Modnet group [114].

All these test methods represent an optimal compromise for scaling the compaction mechanics phenomena from industrial process to research laboratory. On the other hand, some solutions do not properly reproduce and simulate the behavior of powder mix in actual compaction conditions. For instance, the measurement of radial stress by

means of strain gages required a deformable die, usually made of steel, instead of the conventional hard metal die adopted in industrial processes. But the frictional behavior of powder mix against steel could be completely different in comparison with hard metal. So, given that the friction coefficient has a significant role on the axial and radial forces developed during compaction, the stress field derived from a different friction coefficient would not represent the actual compaction operation in real die cavity. Another example regards square section die, whose shape is far away from the axisymmetric geometry of structural parts.

For these reasons, this study has employed an alternative characterization method in order to derive the compaction mechanics of the four powder mixes. The method is totally empirical and is based on the measurement of the position and force of the punches of an industrial press. Some hypotheses are introduced to estimate the friction coefficient and radial stress. The main drawback of this method concerns the precision of axial force measurements by means of press control unit. Since the press is set up to measure high force with high precision, the measurement suffers a higher signal to noise ratio at low forces. To overcome this limitation, the signal of force was analyzed by a Fourier transformation in the frequency domain to develop a filtering strategy improving the reliability of data acquired.

As described, ring-shaped samples were compacted by an industrial hydraulic press of 200 tons with 9 moving axes, 8 hydraulic and 1 electric-close loop. The control unit of the press collected the forces and displacements of each operating axis at the frequency of 2000 Hz. A schematic representation of the measured forces and displacement is reported in figure 2.2, and described as follow:

- F , the force applied by the upper punch;
- F_D , the force applied to the die;
- F_C , the force applied to the core;
- X , the position of the lower surface of the upper punch with respect to the upper surface of the lower punch;
- Z , the position of the upper surface of the die with respect to the upper surface of the lower punch;
- Z_1 , the position of upper surface of the core with respect to the upper surface of the lower punch.

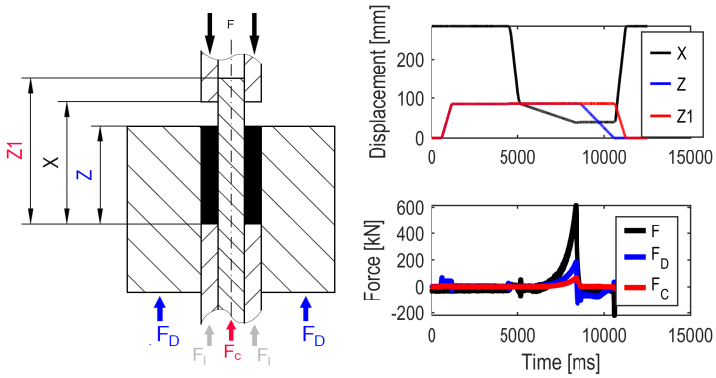


Figure 2.2. Schematic picture of the forces and displacements during the compaction cycle .

The press measuring system can detect the displacement with high accuracy (± 10 microns), while the force is not precisely acquired all over the range investigated since the sensitivity is around 10 kN. Therefore, the uncertainty on force measurement decreases on increasing the compaction force.

In figure 2.3A, an example of the force as recorded by the press is reported. Only the data relevant to the compaction step are considered, whose interval starts when the upper punch contacts the powder column and ends when the highest force applied by the upper punch is reached. It is possible to clearly observe that data are quite scattered, except for the last part of the curve. In order to improve the reliability of the experimental data, force signals were analyzed in the frequency domain. Figure 2.3B shows the module of the result of the Fourier transformation of data showed in figure 2.3A.

The analysis of the force in the frequency domain showed some high amplitude signal components above 100- 200 Hz, which can be related to noise superposed to the actual force signal. In order to remove the undesired noise components, a Butterworth first order low pass filter was initially designed and tested. Nevertheless, this filtering strategy introduced a time shift due to the phase change. To overcome this negative result, a higher order filter was implemented with zero phase response, to avoid the time shift modification (filfilt matlab function [115, 116]) An example of the filtered signal is reported in figure 2.4.

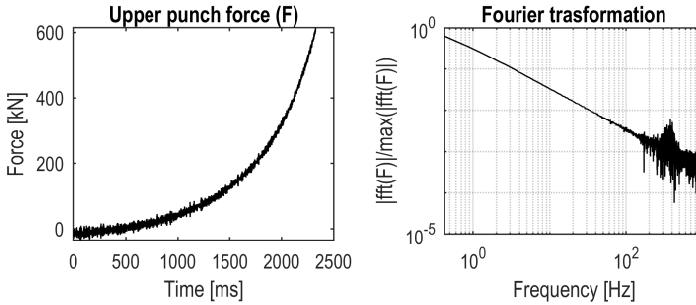


Figure 2.3. (A) Force applied by the upper punch as a function of time. (B) Fourier transformation of the force applied by the upper punch in figure (A).

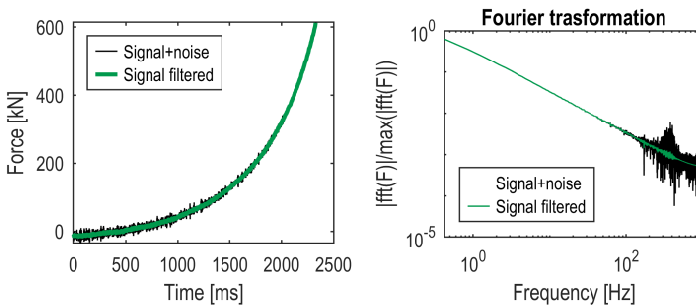


Figure 2.4. Improvement of filtering operation on the signal of force in the time domain (A) and in the frequency domain (B).

By the introduction of this numerical solution, the filter smooths the noise component and improves the accuracy and reliability of the force measurements, as well as the further compaction mechanics description [117].

As previously mentioned, in this study, samples were compacted by single action strategy. Neglecting the force fluctuation due to change in acceleration (inertial force), the equilibrium of force along the compaction direction is expressed by equation (2.1):

$$F = F_D + F_C + F_l \quad (2.1)$$

Since all terms of the equation are known except F_l , the expression can explicit

this unknown parameter. The F_l force is needed to calculate the actual height of the sample during compaction. The sample height is equal to X variable, if the punches are supposed to be infinitely rigid. However, punches can elastically deform during compaction. Hence, introducing the elastic deformation of punches, the actual height of the ring sample under compaction (H_{situ}) is given by equation (2.2):

$$H_{situ} = X + \frac{F}{K_{upper-punch}} + \frac{F_l}{K_{lower-punch}} \quad (2.2)$$

Where $K_{upper-punch}$ and $K_{lower-punch}$ are the stiffness of upper and lower punch⁴, respectively. The geometry of the punches is shown in figure 2.5.

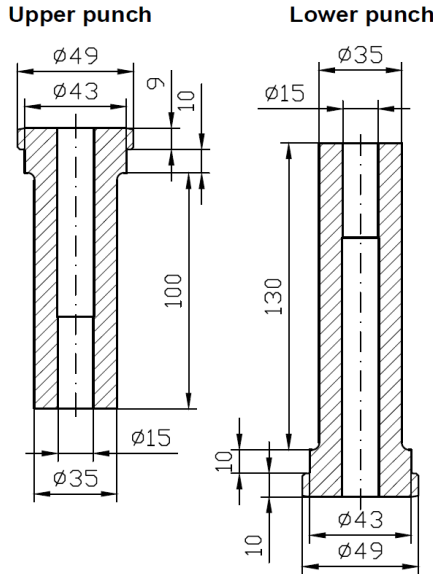


Figure 2.5. Schematic drawing of the upper and lower punches.

The stiffness was estimated by two approaches: a simplified analytical analysis and a finite element analysis. In the analytical approach, each punch was approximated by an assembly of three ring-shaped columns having different sections. This

⁴A more precise analysis should consider the overall elastic response of the press. However, in first approximation the equivalent stiffness of the press can be assumed equal to the stiffness of the punches, because they are the slenderest structural elements.

simplification allows to calculate the stiffness of each ring column (K_{sect}) by equation (2.3):

$$K_{sect} = \frac{E(D_e^2 - D_i^2)\pi}{4l} \quad (2.3)$$

Where:

- E , is the elastic modulus, assumed equal to 210 GPa;
- D_e , is the external diameter of the section investigated;
- D_i , is the internal diameter of the section investigated;
- l , is the length of the ring column investigated.

Finally, the stiffness of the punch is calculated by equation (2.4):

$$K_{analytic} = \left(\frac{1}{K_{sec-1}} + \frac{1}{K_{sec-2}} + \frac{1}{K_{sec-3}} \right)^{-1} \quad (2.4)$$

The second strategy adopted FEM analysis. The 3D model of the punch was imported in Ansys APDL software. As assumed for analytical model, the elastic modulus of the material was set equal to 210 GPa and the Poisson coefficient equal to 0.3. Two boundary conditions were applied to the model. A compression stress (P_{FEM}) of 600 MPa was imposed on the surface of the punch contacting the ring sample. On the opposite surface, axial and radial displacement were fixed equal to zero. The volume was discretized by a free mesh, whose element size is parametrically imposed. Then a solid 185 element was associated to the tetragonal elements of the mesh. For each punch geometry, the FEM problem was solved on increasing the number of discretized elements in order to obtain convergence. At each solution, the axial displacement ($disp$) of the punch induced by the compression load was extracted and saved. For each of the five solutions calculated, the stiffness of the punch was computed by equation (2.5).

$$K_{FEM} = \frac{P_{FEM}}{\frac{(D_{ext}^2 - D_{int}^2)\pi}{4} disp} \quad (2.5)$$

Where:

- D_{ext} is the external diameter of the ring sample,
- D_{int} is the internal diameter of the ring sample.

The convergence analysis of the FEM results is reported on figures 2.6.

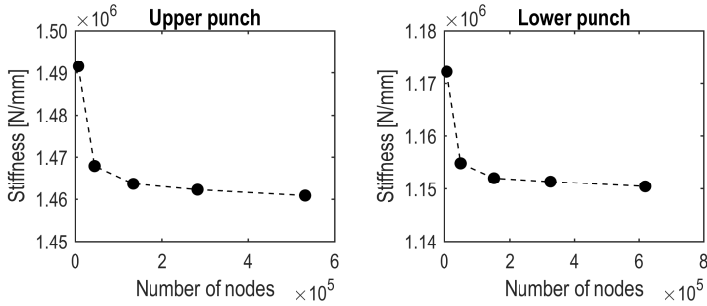


Figure 2.6. Convergence analysis of the stiffness of the upper punch (A) and lower punch (B) on increasing the number of discretized nodes.

	K_{punch} analytic [N/mm]	K_{punch} FEM [N/mm]	$\frac{(K_{FEM} - K_{analytic})}{K_{analytic}}$
Upper punch	1504862	1460878	-2.92%
Lower punch	1171793	1150461	-1.81%

Table 2.2. Numerical results of the punches stiffness by analytical and FEM analysis.

As displayed in figure 2.6, FEM results converge and stabilize on increasing the number of nodes. In table 2.2 the analytical and FEM results are compared. Both methods provide very similar results, though the analytical approach tends to overestimate the stiffness compared to FEM approach. The possible explanation can be ascribed to the approximation of the geometry in ring volumes, disregarding fillets and chamfers. The result derived by FEM method is thus supposed to be more reliable.

The knowledge of the actual height of the ring column allows the calculation of the in-situ density (ρ_{situ}) by equation (2.6):

$$\rho_{situ} = \frac{4m}{\pi(D_{ext}^2 - D_{int}^2)H_{situ}} \quad (2.6)$$

Where:

- m , is the mass of the sample.

The in-situ density corresponds to the mean density of the sample during compaction. Before compaction, in-situ height is equal to the filling height and consequently equation (2.6) provides the filling density (ρ_0).

The relative density is considered as a state variable of the material properties. The relative in situ density (relative density, from here on) is calculated by equation (2.7):

$$\rho_r = \frac{\rho_{situ}}{\rho_{th}} \quad (2.7)$$

Where ρ_{th} is the theoretical density of the powder mix derived by the theoretical density of bulk 316L stainless steel (ρ_{316L}) and Acrawax lubricant (ρ_{Lube}) by equation (2.8):

$$\rho_{th} = \frac{1}{\frac{\%wt_{316L}}{\rho_{316L}} + \frac{\%wt_{Lube}}{\rho_{Lube}}} \quad (2.8)$$

In order to quantify the densification of the powder mix, the compaction pressure should be determined. Actual compaction pressure is simply given by the applied force divided by the section of the die cavity, but the pressure in the powder column is determined by the geometry and the frictional forces. The mean compaction pressure must be calculated, as derived from the mean axial force.

It is well known that the force along compaction direction ($F(x)$) has an exponential decrement due to the frictional force. The relationship for ring geometry is given by equation (2.9):

$$F(x) = F_e^{-4 \frac{\mu_{Die}\sigma_R D_{ext} + \mu_{Core}\sigma_R D_{int}}{D_{ext} + D_{int}}} \frac{1}{\sigma_A} \frac{x}{H_{situ}} \frac{H_{situ}}{(D_{ext} - D_{int})} \quad (2.9)$$

Where:

- μ_{Die} is the friction coefficient of powder against the die surface;
- μ_{Core} is the friction coefficient of powder mix against the core-rod surface;
- σ_A is the mean axial stress along the column;
- σ_R is the mean radial stress.

Friction coefficients and radial stress are unknown variables. In the special condition of single action, equilibrium relationships between frictional forces and the

forces keeping the die and core rod firm can be established, as by equations (2.10) and (2.11) and schematic displayed on figure 2.7:

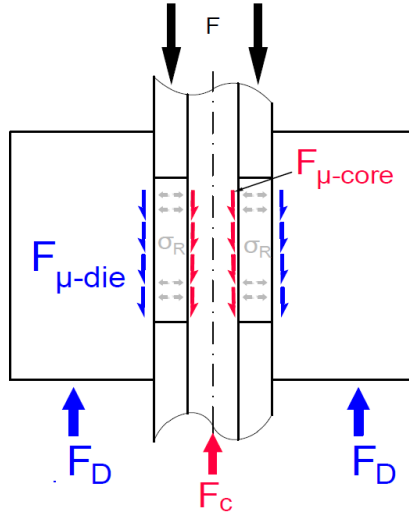


Figure 2.7. Schematic representation of the equilibrium between frictional forces and forces keeping the die and core rod firm.

$$F_D = F_{\mu-die} = \mu_{Die} \sigma_R \pi D_{ext} H_{situ} \quad (2.10)$$

$$F_C = F_{\mu-core} = \mu_{Core} \sigma_R \pi D_{int} H_{situ} \quad (2.11)$$

Since F_D and F_C are known, the mean axial stress can be easily derived by equation (2.12), obtained combining equations (2.9), (2.10), and (2.11).

$$\sigma_A = \left(\frac{-4}{\ln \left(\frac{F_l}{F} \right)} \right) \left(\frac{F_D + F_C}{\pi} \right) \left(\frac{1}{D_{ext}^2 - D_{int}^2} \right) \quad (2.12)$$

This work aims at determining the triaxial stress state as function of the density, so the radial stress has also to be determined. An equipment directly measuring radial

stress and friction coefficients was not available, so that these entities were estimated by introducing some assumptions. Two densification mechanisms are proposed. As reported in section 1.2.2, three main densification mechanisms occur during metal powder compaction: rearrangement, elastic deformation and plastic deformation. The complexity in the development of a model for porous materials consists in the superposition of these densification mechanisms. In this work, two distinct ranges are assumed for material behavior, which are:

- prevailing elastic behavior,
- prevailing plastic behavior.

The elastic behavior would correspond to the rearrangement and the elastic contact loading of particles, whereas the plastic behavior would represent the plastic deformation of metal particles. It must be underlined that plastic behavior does not correspond to irreversible deformation of the powder mix, because also rearrangement determines irreversible deformation. The identification of two prevailing behaviors provides a simplified description of the actual local condition. In fact, it is reasonable to assume that the loading condition of particles changes in relation to the axial gradient of force defined by equation (2.9). For instance, close to the upper punch where the applied force is higher, plastic deformation of the particles contact area could occur, while rearrangement and elastic loading are still occurring close to the lower punch, where the applied force is lower due to the dissipative frictional forces. However, relative density ranges corresponding to prevailing elastic deformation and prevailing plastic deformation can be reasonably assumed, aiming at deriving the relevant compaction mechanics relationships.

No radial deformation (ε_R) of die cavity as well as powder mix was also assumed. By Hooke equations (2.13÷2.15) for elastic material (in cylindrical coordinates), no radial deformation consequently determines no tangential deformation (ε_θ) and the equality between radial (σ_R) and tangential stresses (σ_θ).

$$\varepsilon_R = \frac{1}{E} \{ \sigma_R - \nu (\sigma_\theta + \sigma_A) \} \quad (2.13)$$

$$\varepsilon_\theta = \frac{1}{E} \{ \sigma_\theta - \nu (\sigma_A + \sigma_R) \} \quad (2.14)$$

$$\varepsilon_A = \frac{1}{E} \{ \sigma_A - \nu (\sigma_R + \sigma_\theta) \} \quad (2.15)$$

Consequently, the triaxial state of stress can be described by axial and radial stresses. As an additional consequence of this assumption, radial stress can be computed as a function of axial stress and Poisson coefficient (ν) by equation (2.16) while elastic behavior prevails.

$$\sigma_R = \sigma_A \frac{\nu}{1 - \nu} \quad (2.16)$$

In the literature, Poisson coefficient is generally derived by the measurement of axial and radial stresses during the unloading step of compaction cycle [104, 118].

In this work, Poisson coefficient is set equal to 0.25, based on previous result obtained for cylindrical samples [119]. Some papers supported the hypothesis of constant Poisson coefficient, whose value is independent on the relative green density [104], while other works identified a relationship between them [108, 120].

The assumption of no radial deformation is reasonable if the sample is compacted at low density. This hypothesis can be demonstrated by a preliminary assessment through the continuum mechanics of cylindrical shell theory [121]. The theory of cylindrical shell provides an analytical solution for the elastic stress-strain problem of axisymmetric geometry. In this theory, one of the main assumptions regards the constant loading along the axis reference system. This condition is not satisfied during compaction. In fact, just a part of the die cavity is loaded, and the radial stress is not uniform along the axis. Nevertheless, shell theory provides a useful overestimation to demonstrate that radial deformation is negligible for the density reached in this study⁵.

On the basis of the aforementioned statements, shell theory provides an analytical solution for the radial (σ_R) and tangential stresses (σ_θ), expressed by equations (2.17) and (2.18).

$$\sigma_R = \frac{EC_1}{1 - \nu} - \frac{EC_2}{1 + \nu} \frac{1}{r^2} = A - \frac{B}{r^2} \quad (2.17)$$

$$\sigma_\theta = \frac{EC_1}{1 - \nu} + \frac{EC_2}{1 + \nu} \frac{1}{r^2} = A + \frac{B}{r^2} \quad (2.18)$$

Where:

- E is the elastic modulus;
- ν is the Poisson coefficient;

⁵A FEM analysis provides a more precise estimation of the radial deformation of the die cavity. However, a negligible expansion of die cavity results by shell theory. Since the analytical solution provides an overestimation of the stress condition for the reasons stated, FEM analysis can be avoided.

- C_1, C_2, A, B are constants which depend on the boundary condition of the problem;
- r is the radius coordinate on cylinder reference system.

The displacement along the radial direction caused by the radial stress is computed by equation (2.19):

$$u = C_1 r + \frac{C_2}{r} \quad (2.19)$$

Core-rod can be assumed as a ring with an internal radius equal to zero, whereas the external radius is 7.5 mm. Based on this boundary condition, the diameter of the core-rod can be expressed as a function of the radial stress by equation (2.20).

$$D_{core-rod}(\sigma_R) = D_{core-rod} - 2 \frac{\sigma_R (1 - \nu_3)}{E_3} \frac{D_{core-rod}}{2} \quad (2.20)$$

Where:

- E_3 is the elastic modulus imposed equal to 210 GPa;
- ν_3 is the Poisson coefficient assumed equal to 0.3.

Figure 2.8 shows the change in diameter as a function of radial stress.

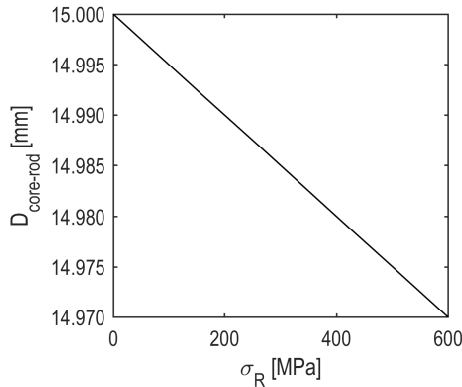


Figure 2.8. Actual core-rod diameter as function of the radial compression stress.

The study of the elastic deformation of the die is more complicated. Die is generally made of hard metal and it safely operates under compressive stress. To avoid the

generation of shear and tensile stresses, hard metal cavity is mounted by interference on a steel frame. Interference fit determines residual compression state of stress, which should be considered in addition to the stress originated during compaction cycle to evaluate die deformation. The residual stress field promoted by interference fit is firstly studied, and subsequently the compression stress condition caused by the powder compression. Then the principle of superposition is applied in order to derive the cumulative effect on stress-strain condition of the die cavity.

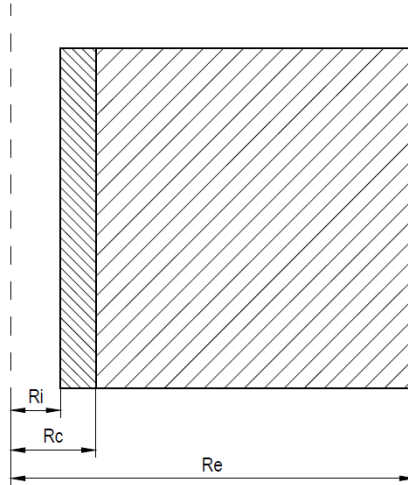


Figure 2.9. Scheme of the die mounted on steel frame.

The pressure (P_C) at the interface is determined by equation (2.21).

$$P_C = \frac{i}{R_c \left[\frac{1}{E_2} \frac{R_e^2 + R_c^2}{R_e^2 - R_c^2} + \frac{\nu_2}{E_2} + \frac{1}{E_1} \frac{R_c^2 + R_i^2}{R_e^2 - R_i^2} - \frac{\nu_1}{E_1} \right]} \quad (2.21)$$

Where:

- i is the interference fit.
- E_1 is the elastic modulus of hard metal, set equal to 500 GPa.
- ν_1 is the Poisson coefficient of hard metal, set equal to 0.3.

- E_2 is the elastic modulus of steel, set equal to 210 GPa.
- ν_2 is the Poisson coefficient of steel, set equal to 0.3.
- R_i is the internal radius of the die (17.5 mm).
- R_c is the radius at the interference.
- R_e is the external radius of the steel frame.

Knowing P_C and imposing a boundary condition of no radial stress at the internal (R_i) and external radius (R_e), it is possible to derive the residual state of stresses after the interference fit by equations (2.17-2.18). The resulting radial and tangential stresses along radius are expressed by equations (2.22÷2.25).

$$\sigma_{R-inter} = \frac{P_c R_c^2 - P_i R_i^2}{R_i^2 - R_c^2} - \frac{(P_c - P_i) R_i^2 R_c^2}{R_i^2 - R_c^2} \frac{1}{r^2} \text{ for } R_i < r < R_c \quad (2.22)$$

$$\sigma_{R-inter} = \frac{P_e R_e^2 - P_c R_c^2}{R_c^2 - R_e^2} - \frac{(P_e - P_c) R_c^2 R_e^2}{R_c^2 - R_e^2} \frac{1}{r^2} \text{ for } R_c < r < R_e \quad (2.23)$$

$$\sigma_{\theta-inter} = \frac{P_c R_c^2 - P_i R_i^2}{R_i^2 - R_c^2} + \frac{(P_c - P_i) R_i^2 R_c^2}{R_i^2 - R_c^2} \frac{1}{r^2} \text{ for } R_i < r < R_c \quad (2.24)$$

$$\sigma_{\theta-inter} = \frac{P_e R_e^2 - P_c R_c^2}{R_c^2 - R_e^2} + \frac{(P_e - P_c) R_c^2 R_e^2}{R_c^2 - R_e^2} \frac{1}{r^2} \text{ for } R_c < r < R_e \quad (2.25)$$

The stress condition caused by compaction cycle is again evaluated by equations (2.17÷2.18), assuming constant radial pressure at the internal diameter and no radial stress at the external diameter. Consequently, the radial and tangential stresses are determined by equations (2.26) and (2.27):

$$\sigma_{R-comp} = \frac{P_e R_e^2 - P_i R_i^2}{R_i^2 - R_e^2} - \frac{(P_e - P_i) R_i^2 R_e^2}{R_i^2 - R_e^2} \frac{1}{r^2} \quad (2.26)$$

$$\sigma_{\theta-comp} = \frac{P_e R_e^2 - P_i R_i^2}{R_i^2 - R_e^2} + \frac{(P_e - P_i) R_i^2 R_e^2}{R_i^2 - R_e^2} \frac{1}{r^2} \quad (2.27)$$

Hence, the actual stress condition of the die frame is evaluated by superposition principle. Figure 2.10 reports an example of stress and displacement along the radius

with the hypothesis of 0.02 mm interference and radial stress under compaction 300 MPa.

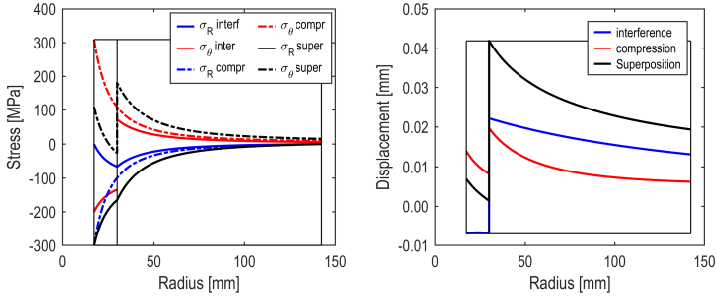


Figure 2.10. (A) Resulting radial and tangential stresses along the radius of die cavity for the interference, compression and superposition conditions. (B) displacement of die cavity at different radius coordinates in the case of interference, compression and superposition conditions.

The displacement of internal diameter of the die cavity is evaluated at different interference conditions and radial stresses. The graphical result is showed in figure 2.11(A). On increasing the radial pressure, diameter increases, as expected, while the increase of interference fit determines the reduction of the diameter.

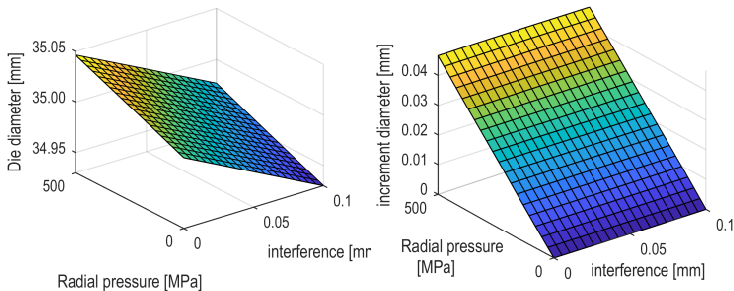


Figure 2.11. (A) die diameter and normalized die diameter (B) function of the radial pressure and the interference.

In order to better comprehend the dimensional change of the diameter of the die, the effect of interference fit is normalized. The increment of die diameter is

evaluated in comparison to the unloading condition when the radial stress is zero. The result is illustrated on figure 2.11(B), where the independency of diameter expansion by the interference fit is observed. Therefore, dimensional variation of die diameter only depends on the radial compression developed during compaction cycle, and the increment of diameter of the die can be expressed as a function of radial stress by equation (2.28).

$$D_{die}(\sigma_R) - D_{die}(0) = 2 \frac{\sigma_R}{E_1} \frac{R_i^3}{R_c^2 - R_i^2} \left[(1 - \nu_1) + (1 + \nu_1) \frac{R_c^2}{R_i^2} \right] \quad (2.28)$$

Combining equations (2.20) and (2.28) the actual section of the die cavity as a function of the radial stress can be evaluated. Figure 2.12 reports the percentage error of section and in-situ density obtained under the hypothesis of no radial deformation. Since error is below 1%, the hypothesis of no radial deformation seems reasonable.

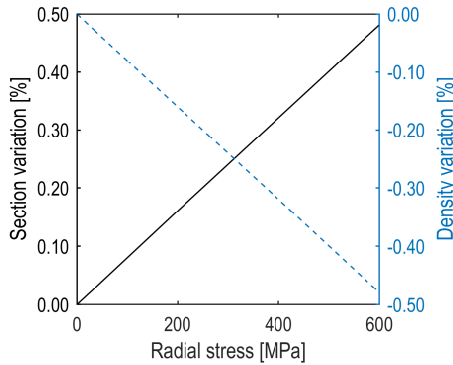


Figure 2.12. Percentage error of in-situ section and in-situ density of ring samples vs. radial stress under the hypothesis of no radial deformation of die cavity.

The deformation of the die is negligible, so that the volumetric strain of the powder mix can be evaluated by equation (2.29):

$$\varepsilon_{V-dens} = 1 - \frac{V_{situ}}{V_0} = 1 - \frac{H_{situ}}{H_0} = 1 - \frac{\rho_0}{\rho_{situ}} \quad (2.29)$$

Under the assumption of elastic behavior, the friction coefficient of the powder mix against the die and core-rod walls can be derived from equations (2.30) and (2.31),

respectively, resulting from the combination of equations (2.10) and (2.11) with equation (2.16).

$$\mu_{Die} = \frac{F_D}{\sigma_A \frac{\nu}{1-\nu} \pi D_{ext} H_{situ}} \quad (2.30)$$

$$\mu_{Core} = \frac{F_C}{\sigma_A \frac{\nu}{1-\nu} \pi D_{int} H_{situ}} \quad (2.31)$$

Equations (2.16), (2.30), and (2.31) are only valid while elastic deformation prevails, while, in plastic field, another formulation of radial stress and friction coefficients is required. Literature findings on friction coefficients suggest how to formulate the new relationships. Analyzing the frictional forces during compaction cycle, at the very beginning of densification (prevailing elastic behavior), powder-wall friction arises or rapidly changes whereas density increases. This result can be ascribed to the irregular sliding of particles against die walls, as a consequence of rearrangement. At the end of rearrangement, when plastic deformation becomes the prevailing densification mechanism, friction coefficient stabilizes around a constant value. According to main literature results, this work assumes that friction coefficient is kept constant on increasing relative density, on prevailing plastic deformation [106, 122–125].

As by other papers, friction coefficient tends to slightly decrease in close proximity of very high relative density [103, 113, 114]. Since in the present work samples are not compacted close to theoretical green density, the hypothesis of constant friction coefficient is still reasonable.

By the assumption of no radial deformation and constant friction coefficient, the radial stress can be expressed by equation (2.32):

$$\sigma_R = \frac{F_D}{\mu_{Die-avg} \pi D_{ext} H_{situ}} = \frac{F_C}{\mu_{Core-avg} \pi D_{int} H_{situ}} \quad (2.32)$$

The value of $\mu_{Die-avg}$ and $\mu_{Core-avg}$ correspond to the mean friction coefficients determined by equations (2.30) (2.31) in a small interval before the transition from the elastic to plastic behavior. Since the transition is gradual, the friction starts to stabilize in the end of elastic domain. Therefore, these average values are also kept in the plastic field.

The equations and assumptions describing the compaction mechanics of powder mix presented above, strictly need for the identification of the transition threshold from elastic to plastic field. As previously described in section 1.2.2, in porous materials different densification mechanisms simultaneously occur during compaction, as showed by the figure 1.2 describing the density versus compaction pressure. For this reason, a univocal transition point defining the transition from elastic to plastic deformation cannot be graphically derived from the densification curve.

A precise determination of the elasto-plastic transition should investigate the particle shape change on metallographic micrographs obtained by samples homogeneously compacted at different density. By this procedure, it should be possible to highlight the actual relative density at which plastic deformation induces a permanent change in powder morphology. However, this experimental activity is highly time consuming, and it was not affordable. Lots of samples should be compacted at different densities and should be investigated at different positions in order to obtain statistically reliable results.

A numerical recursive method was instead developed in this work. This procedure aims at individuating the relative density corresponding to the transition from a generalized elastic to plastic deformation by means of a recursive method based on specific criteria. The recursive method is schematized by the flowchart in figure 2.13.

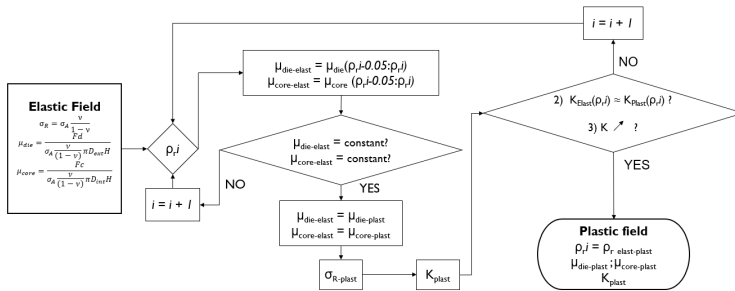


Figure 2.13. Schematic flowchart of the recursive method developed for determining the relative density corresponding to elasto-plastic transition.

The recursive method assesses the elastic to plastic transition at a low attempting value of relative density (ρ_{r-i}). In the elastic field, radial stress and friction coefficients can be derived by equations (2.16), (2.30), and (2.31). The obtained friction coefficients

are analyzed as function of relative density. As previously explained, constant friction coefficient can be related to the beginning of prevailing plastic behavior. Hence friction coefficients are evaluated in an interval before the transition ρ_{r-i} . In this work the interval was set equal to 0.05 of relative density. If friction coefficients do not stabilize around constant value, then the first condition of the recursive method is not satisfied. Therefore ρ_{r-i} is updated at higher value and the condition is tested once again, unless the friction coefficients show constant trend.

Friction coefficients settled around a constant value allow calculating $\mu_{Die-avg}$ and $\mu_{Core-avg}$ in the interval of relative density before the transition. Then radial stress is deduced by equation (2.32), and consequently the radial to axial stress transmission coefficient K_{σ_R/σ_A} by equation (2.33).

$$K_{\sigma_R/\sigma_A} = \frac{\sigma_R}{\sigma_A} \quad (2.33)$$

The second condition of the recursive method requires the continuity of radial to axial stress transmission coefficient at elasto-plastic transition threshold. The condition can be expressed by equation (2.34).

$$(K_{\sigma_R/\sigma_A})|_{elast\ cond} = (K_{\sigma_R/\sigma_A})|_{plast\ cond} \quad (2.34)$$

In elastic field K_{σ_R/σ_A} is constant, and depends on the Poisson coefficient as established by equation (2.16).

The third condition concerns the trend in the plastic field. K_{σ_R/σ_A} must increase, and tends towards 1 for physical reasons. In fact, by the closure of porosity and the increase of compact resistance, material exhibits a transition from a compressive to an incompressible response. Mathematically, in plastic field K_{σ_R/σ_A} should monotonically increase on increasing relative density.

If one of the two conditions above on K_{σ_R/σ_A} is not verified, higher relative density is considered, looking for transition value.

Summarizing, the recursive method aims at identifying the relative density at which the transition from the prevailing elastic to plastic behavior occur. The recursive method converges when the following three criteria are satisfied:

1. constant friction coefficients in interval of 0.05 before transition in the elastic field;
2. continuity of K_{σ_R/σ_A} at the transition;
3. increasing trend of K_{σ_R/σ_A} in the plastic field as function of relative density. step.

This numerical recursive method has an experimental confirmation. Heckel [126] identified a minimum strength, which allows safe handling of green part. In other words, plastic deformation begins when part has sufficient mechanical consistency. In a previous work [19], ring samples were compacted at different densities, and it was confirmed that parts can be safely handled only over the transition relative density found by this iterative procedure.

In conclusion, the whole method above provides the mean axial and radial stresses as function of in-situ density during compaction. The principal components of stress tensor allow obtaining the hydrostatic and effective stress by equations (2.35) and (2.36). These stress invariants are useful for the calibration of the constitutive material model for powder compaction, and for the further correlation with the anisotropy of dimensional changes presented in *Results and discussion* (chapter 2.5).

$$\sigma_{Hydr} = \frac{\sigma_A + 2\sigma_R}{3} \quad (2.35)$$

$$\sigma_{eff} = \sigma_A - \sigma_R \quad (2.36)$$

2.4 Estimation of the dimensional change

The dimensional changes of internal diameter, external diameter, and height were calculated by equations (2.37–2.39), respectively. In addition, the radial and tangential dimensional variations were estimated by equations (2.40) and (2.41):

$$\varepsilon_{Dint} = \frac{D_{int,s} - D_{int,g}}{D_{int,g}} \quad (2.37)$$

$$\varepsilon_{Dext} = \frac{D_{ext,s} - D_{ext,g}}{D_{ext,g}} \quad (2.38)$$

$$\varepsilon_H = \frac{H_s - H_g}{H_g} \quad (2.39)$$

$$\varepsilon_R = \frac{Th_s - Th_g}{Th_g} \quad (2.40)$$

$$\varepsilon_\theta = \frac{D_{Avg,s} - D_{Avg,g}}{D_{Avg,g}} \quad (2.41)$$

Where:

- Th is the thickness calculated by the difference between external and internal radii;
- D_{Avg} is the average diameter calculated as the mean value between the external and internal diameters.

The subscripts g and s refer to green and sintered parts, respectively.

The change in volume (ε_V) was also evaluated by equation (2.42) where the volume of the ring was determined by the average volume of diameters and height.

$$\varepsilon_V = \frac{V_s - V_g}{V_g} \quad (2.42)$$

Under the hypothesis of negligible volume distortion during the sintering process, the change in volume can be related to the dimensional change by equation (2.43). In addition, the isotropic dimensional change (ε_{ISO}) can be calculated by equation (2.44).

$$(\varepsilon_V + 1) = (\varepsilon_R + 1) (\varepsilon_\theta + 1) (\varepsilon_H + 1) \quad (2.43)$$

$$\varepsilon_{ISO} = \sqrt[3]{(\varepsilon_V + 1)} - 1 \quad (2.44)$$

ε_{ISO} relates the change in volume to the dimensional variation under the assumption of isotropic dimensional change on sintering. For this reason, ε_{ISO} represents an important indicator for the quantification of the anisotropic dimensional change on sintering. In addition, it could be a key parameter predicting the anisotropic behavior, as it will be described in sections 2.5.7 and 3.3.

In next chapter, dimensional changes on sintering are measured and put to relationship with the triaxial stress condition during compaction, in order to highlight the influence of the inhomogeneity of compaction stress on the anisotropy of dimensional changes.

2.5 Results and discussion

2.5.1 Introduction

This section discusses the main results regarding compaction mechanics and sintering dimensional changes of the ring samples made with different particle sizes. Compaction mechanics is firstly described. The compressibility behavior was investigated considering both the applied and the mean axial pressure in order to highlight the most effective variable describing the phenomenon. On the basis of some assumptions, the radial stress was evaluated in the field of prevailing plastic deformation. In this way, the triaxial state of stress was completely derived and the deviatoric stress tensor was computed, as well as the radial to axial stress transmission coefficient. The analysis of compaction mechanics also considers the frictional coefficients and the relative densities corresponding to the transition from prevailing elastic to prevailing plastic behavior.

The mean dimensional change on sintering was further discussed, as well as the dimensional variation of the diameters measured at three equally spaced levels. Finally, the stress field occurred in compaction has been related to the dimensional change on sintering. The proportionality between stress and shrinkage confirms the role of uniaxial compaction in the origin of the anisotropic dimensional variation, and a specific linear relationship has been highlighted for each particle size. Some hypotheses have been proposed in order to explain the different behavior.

2.5.2 Densification

Table 2.3 reports the comparison of the filling densities for the four particle sizes at the two geometries investigated, and table 2.4 displays the filling densities of ring samples made with standard powder.

$\frac{H}{2T}$	Standard [g/cm ³]	45 [g/cm ³]	45-90 [g/cm ³]	90 [g/cm ³]
0.5	3.17	3.36	2.59	2.23
1.5	3.11	3.34	2.57	2.20

Table 2.3. Filling density of ring samples made with the four particle sizes.

$\frac{H}{2T}$	Standard [g/cm ³]
0.25	3.28
0.50	3.17
1.00	3.11
1.50	3.11
2.00	3.13

Table 2.4. Filling densities computed from the different sample heights made with standard powder.

As listed in tables 2.3-2.4, the filling density appreciably increases moving from coarser to finer particles. The trend is confirmed by some experimental works [127]. A qualitative estimation of particles shape can be derived by the scanning electron micrographs reported in figures 2.14÷2.17.

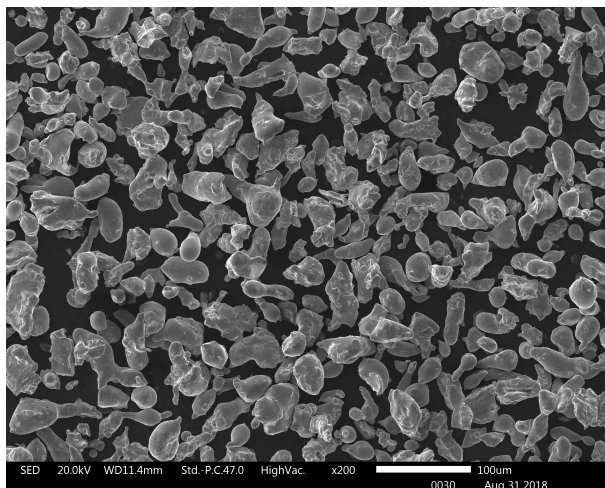


Figure 2.14. Scanning electron micrographs of particle size 45 - as-received state.

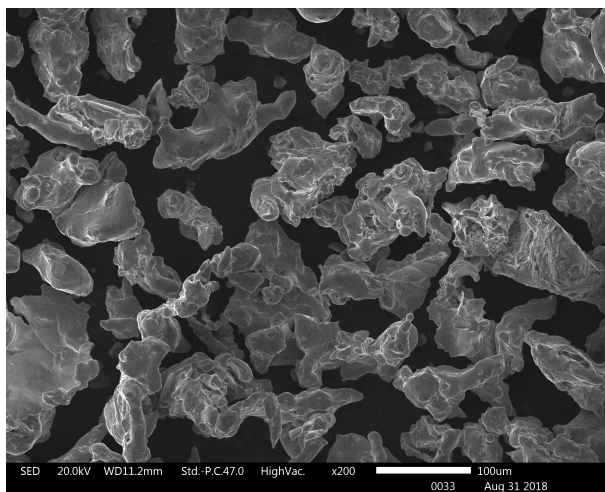


Figure 2.15. Scanning electron micrographs of particle size 45-90 - as-received state.

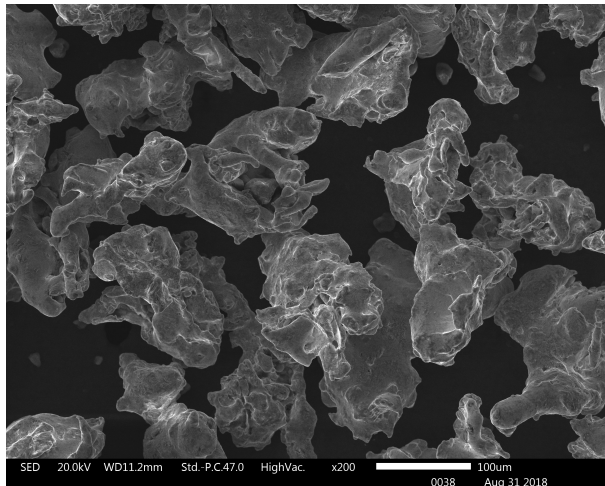


Figure 2.16. Scanning electron micrographs of particle size 90 - as-received state.

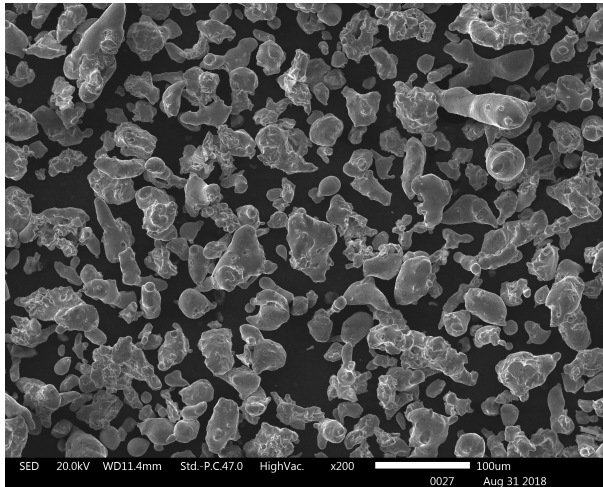


Figure 2.17. Scanning electron micrographs of standard powder - as-received state.

Morphology of coarser particles is highly irregular, while the aspect ratio⁶ should be statistically close to one in smaller particles. The lower aspect ratio and the smoother surface morphology could determine the denser packing, that is higher filling density, related to the finer particle size. The lower filling density measured in coarse particle size can be related to the asperities on the irregular particle surface. In further work, image analysis might be helpful to quantify the worsening of surface morphology on increasing particle size.

As by tables 2.3 and 2.4, a low effect of geometry on filling density is observed. Filling density slightly decreases on increasing height, likely due to the interaction of powders with the die wall cavity. The particles contacting the die could determine interparticle bridging, and consequently the lower packing. The hypothesis is strengthened by literature. Rice and Tengzelius discovered that the filling density decreases on decreasing die diameter [128]. On decreasing the diameter of the die, the number of particles in the section is reduced, and a relatively high number of powder particles is in contact with the die cavity. Nevertheless, the filling density of the highest ring is slightly against the trend, maybe due to the influence of gravity

⁶In this work, the aspect ratio refers to the ratio between the shortest and longest Feret diameters distinguished in the particle. Aspect ratio equal to one indicates spherical shape, and a decreasing value means transition towards elliptic shape.

force, which favors high packing.

The average filling density of the standard powder is more similar to that corresponding to the finer particle size (45), than to the intermediate one (45-90). The reason might be ascribed to the particle size distribution of standard powder. The powder supplier indicates that the commercial AISI 316L powder is formed by 41% of particles smaller than 45 microns, while just 1% are bigger than 150 microns [129]. According to this weight fractions, the filling densities of particle size 45 and 45-90 could be used in the rule of mixture to predict the filling density of the standard powder. However, filling density could be underestimated in this way, because homogeneous mixing determines a noticeable increase in packing, as explained by German, thus explaining the results above [130].

Filling density must not be mistaken for apparent density. In fact, apparent density of standard powder declared by the powder supplier (2.69 g/cm^3) is significantly lower than filling density in this work (3.1 g/cm^3). It has to be underlined that powder supplier measures apparent density according to the procedure reported in the standards [131–133]. The standard procedure recommends evaluating the apparent density by the weight of powders flowing through a standardized nozzle in a cylindrical cavity, whose dimensions are fixed. The filling density in this work was measured by mass and volume of samples. The mass of the green sample was measured after ejection, reasonably hypothesizing that the mass of the green compacts is equal to the mass of powders flowed in the die during the filling operation. The volume of the particles in the filling step was determined by the section of the die cavity and the corresponding height of the powder column, as derived from the position of the upper punch contacting the powder column before compaction (see figure 2.2).

Obviously the two methods are not comparable and the different results have to be attributed to the different flowability of powders through the nozzle in the standard apparatus and through the filling shoe in the industrial press. As by the standard used for reference, powder flows through a small nozzle, whose diameter is nominally 2–5 millimeters, while the filling shoe is generally larger than the die cavity, which means one order of magnitude bigger than the standard apparatus. The second great difference regards the effect of gravity on the powder flow. This force is negligible in standard apparatus, due to the small amount of powder used, but it is significant in the die filling, and it could be an important cause of the higher filling density obtained.

As outlined in section 2.2, the forces acting on punches, die and core-rod, and related displacements, were measured during the compaction cycle in order to study the densification of the four powder mixes. Considering the punch stiffness, the actual height of the samples during compaction was determined, and subsequently the actual relative density. The relative density is plotted as a function of the applied pressure in figure 2.18, and the volumetric strain is shown as a function of the applied pressure in figure 2.19 for the four particle sizes and the different geometries.

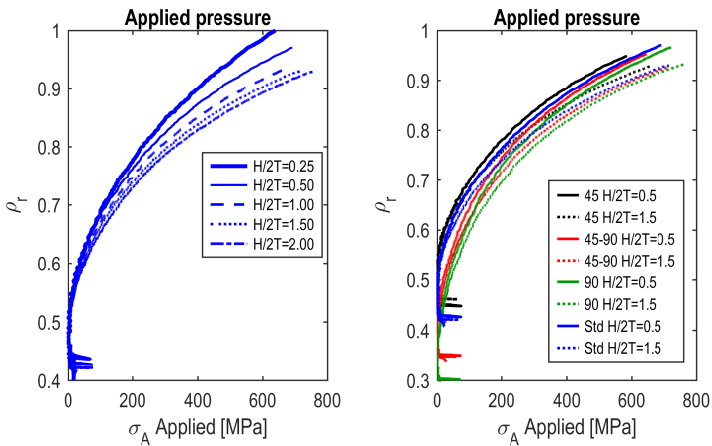


Figure 2.18. Relative density vs. applied compaction pressure for the standard powder (on the left) and the different particle sizes (on the right).

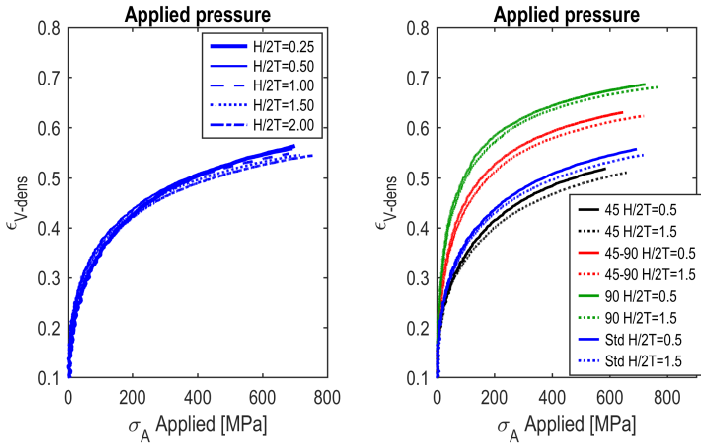


Figure 2.19. Volumetric strain vs. applied compaction pressure for the standard powder (on the left) and the different particle sizes (on the right).

These graphs distinctly depict the influence of particle size and sample geometry on the densification behavior. The influence of geometry is firstly analyzed. Considering each powder mix separately, as expected a higher pressure must be applied on increasing height in order to reach the same relative density, due to the dissipative frictional forces opposing the applied mechanical force. The sampling in this study is obtained by single action compaction, therefore the frictional forces are not balanced as in double action compaction. On the basis of the equilibrium of axial forces reported on equation (2.1), the applied force is proportional to the frictional forces which, in turn, are proportional to the surface areas as expressed by equations (2.10) and (2.11). Therefore, the increase in height generates higher frictional forces, determining the need for higher applied force to compact the sample. A different trend is shown in figures 2.20-2.21, which report the mean axial pressure instead of the applied pressure. The mean axial pressure corresponds to the average of the stresses determined by the gradient of force, as calculated by equation (2.12). Since a gradient of force implies a gradient of density, and the mean relative density was used in figure 2.18, the densification of the powder mix is more coherently described by the mean relative density as a function of the mean pressure.

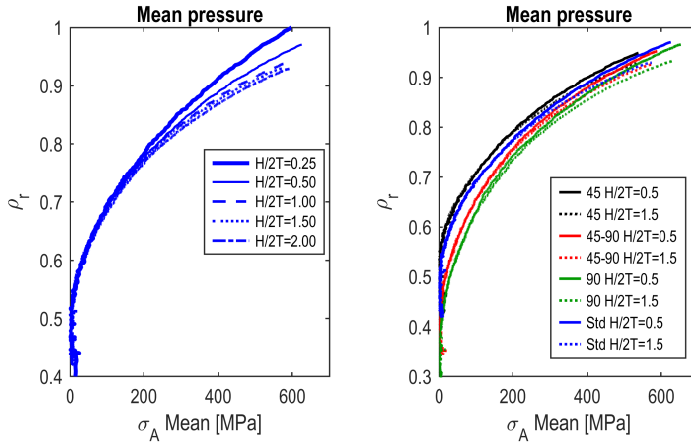


Figure 2.20. Relative density vs. mean compaction pressure for the standard powder (on the left) and different particle sizes (on the right).

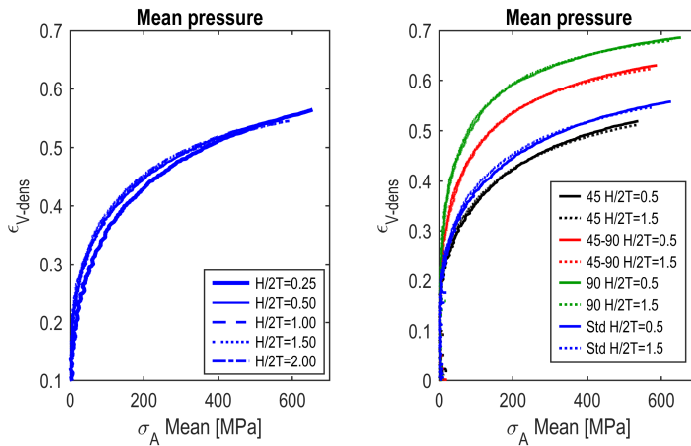


Figure 2.21. Volumetric strain vs. mean compaction pressure for the standard powder (on the left) and different particle size (on the right).

The densification curves in figure 2.21 for each particle size are quite overlapped, while in figure 2.20, low samples at high mean axial pressure show higher density, significantly higher for the lowest one. The same green density was measured in all the samples, so it is also hard to justify the theoretical green density reached during the compaction process. The possible deformation of the die cavity induced by the radial stress should be considered. In the above analysis, the die cavity is supposed constant during the overall compaction cycle, so that an overestimation of the relative density might result, showing an unexpected higher effect on the smaller samples⁷. The method used in this work is thus not completely satisfactory to investigate low samples. Another explanation might be related to the interparticle friction coefficient. If the dissipative interparticle frictional forces are assumed proportional to the volume of the sample, the mean axial stress should increase with the sample height.

In conclusion, the use of mean forces and relative densities allows to describe densification with limited influence of sample geometry, thus providing reliable data for modeling the compaction mechanics of complex components.

Finally, the densification behavior is analyzed as a function of the different particle size. Generally, on increasing particle size, an increasing axial pressure is required in order to reach the same density, as also reported in literature [134]. Coarse particles (90) show pronounced rearrangement in the initial compaction stage, the relative density rapidly increases by a small increment of axial pressure. This is particularly evident in figure 2.21. From a general point of view, particles rearrangement is less pronounced on decreasing particle size. The different densification in the beginning of compaction mainly depends on the filling density. Since coarse particles (90) are packed at low density, the relative density rapidly increases when the axial pressure is applied. On the contrary, the relative density is high for the finer particle size (45) in the beginning of compaction. Consequently, this powder rapidly moves from elastic to prevailing plastic behavior. The compressibility of the standard powder is similar to the finer particle size, being the filling density similar.

⁷In section 2.3 it was concluded that the hypothesis of negligible deformation of the die is reasonable for the hypothetical stress condition. However, the calculation shows that a small radial deformation occurred, likely determining a lower actual density. Since the analytical model supposed the radial stress to be constant along the axial direction, sample height does not affect the die expansion. However, it is known that there is a gradient of the axial and radial stress along the sample height, consequently height should also be considered estimating die expansion and therefore in-situ density.

2.5.3 Elasto-plastic transition threshold

Compaction mechanics analysis needs for accurate identification of the relative density corresponding to the transition threshold between elastic to prevailing plastic deformation. The iterative procedure described in 2.3 aims at identifying such relative density. The iterative procedure evaluates the required conditions on the friction coefficients and the radial to axial stress transmission coefficient. Specifically, the trend of frictional coefficients, as function of relative density, must be constant before the transition threshold, and the trend of the radial to axial stress transmission coefficient (K_{σ_R/σ_A}), as function of relative density, must be continuous at the threshold and continuously increasing after the threshold.

Some iterations of the recursive procedure are reported as example, referring to particle size 90 and geometry H/2T=0.5. Figures 2.22÷2.25 show the frictional coefficients and K_{σ_R/σ_A} , as calculated assuming the transition threshold at increasing relative density. It is reminded that the friction was evaluated in the elastic region in an interval of 0.05 of relative density before the hypothetical transition. Then K_{σ_R/σ_A} derived from the elastic domain was compared with the linear regression of K_{σ_R/σ_A} in the plastic field, in order to verify the continuity at the relative density transition.

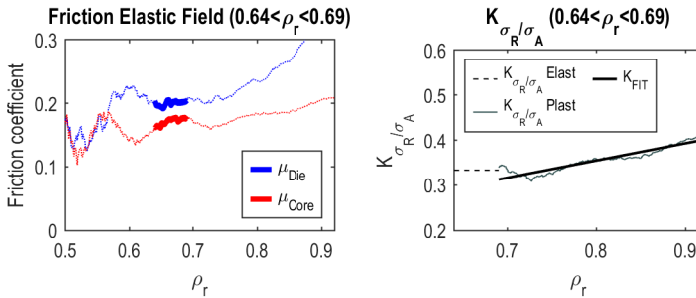


Figure 2.22. Friction coefficients (on the left) and radial to axial stress transmission coefficient (on the right) as function of the relative density - transition threshold at the relative density 0.69.

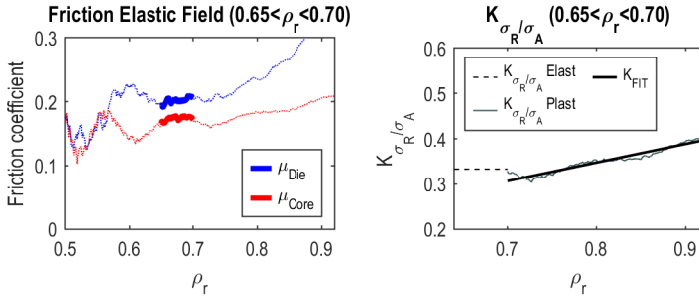


Figure 2.23. Friction coefficients (on the left) and radial to axial stress transmission coefficient (on the right) function of the relative density - transition threshold at the relative density of 0.70.

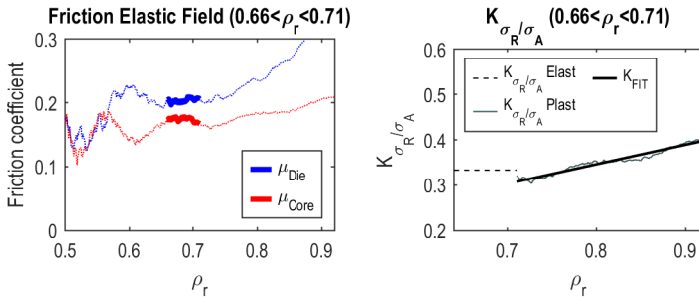


Figure 2.24. Friction coefficients (on the left) and radial to axial stress transmission coefficient (on the right) function of the relative density - transition threshold at the relative density of 0.71.

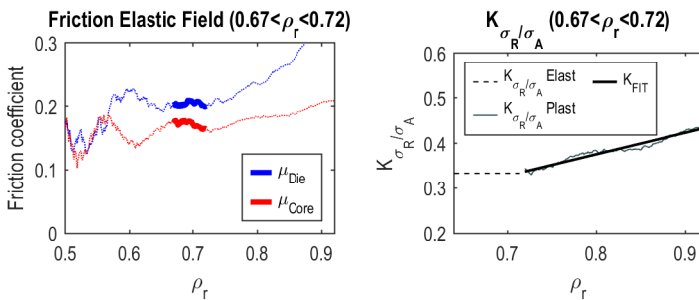


Figure 2.25. Friction coefficients (on the left) and radial to axial stress transmission coefficient (on the right) function of the relative density - transition threshold at the relative density of 0.72.

All the iterations in the figures satisfy the condition of an acceptably constant behavior of the friction coefficient in the elastic region. The continuity of K_{σ_R/σ_A} at the transition threshold is satisfied only at the relative density 0.72. The same analysis was repeated for all the powder mixes and table 2.5 summarizes the relative density corresponding to the transition from prevailing elastic to prevailing plastic behavior.

particle size	$\rho_{r, \text{elast-plast}}$	σ_A threshold [MPa]
Standard	0.74	160
45	0.77	174
45-90	0.74	186
90	0.72	183

Table 2.5. Relative density and mean axial stress corresponding to the transition threshold for the different particle sizes.

On decreasing particle size, the transition occurred at an increasing value of relative density. The standard powder showed the same transition as the intermediate particle size (45-90). This result is apparently contradicting the trend observed in densification curves, showing similarities between standard powder and the finer particle size (45). The result is not completely understood, the role played by the particle size distribution in standard powder should be considered.

Table 2.5 also reports the mean axial stress corresponding to the transition. It is interesting to observe that the values are practically the same for all the particle sizes, the standard powder just slightly differs. In the beginning of compaction, powders rearrange in a denser configuration. In this step, particles are elastically loaded, and the contact interaction can be described by Hertz model. On increasing the compaction force, particles plastically deform, and the contact area grows according to the material hardening rule. At the same time, plastic deformation prevails in the powder mix. Since all particle size were sieved by the same batch of AISI 316L, the yield strength and the hardening rule of the metal powders are independent on the particle size. However, the apparent mean axial pressure corresponding to yield occurred at different relative densities for the different particle sizes, and the higher relative density is linked to the higher filling density. Some authors partially proved that the compaction behavior of the powder mix is virtually ruled by the local deformation of particles [135, 136], thus

confirming the results in this work.

2.5.4 Friction coefficients

One of the assumptions of the recursive procedure implies the stabilization of the frictional coefficients around a constant value on increasing relative density. When the transition threshold was found, the mean frictional coefficient between the powder mix and the die (μ_{Die}) and core-rod (μ_{Core}) were determined. The results are reported in figure 2.26 and tables 2.6÷2.8 for the different particle sizes and geometries.

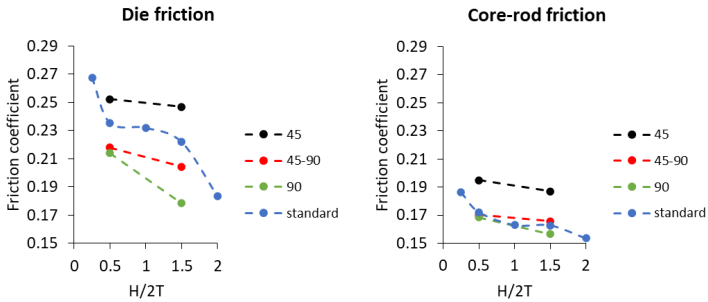


Figure 2.26. Friction coefficient against the die (on the left) and the core-rod (on the right) for the four particle sizes - different heights.

$H/2T$	Standard	45	45-90	90
0.5	0.22	0.25	0.22	0.21
1.5	0.21	0.25	0.20	0.18

Table 2.6. Mean friction coefficient between the powders and die surface for the four particle sizes.

$H/2T$	Standard	45	45-90	90
0.5	0.16	0.19	0.17	0.17
1.5	0.16	0.19	0.17	0.16

Table 2.7. Mean friction coefficients between the powders and the core-rod surface for the four particle sizes.

$H/2T$	Standard (die)	Standard (core)
0.25	0.27	0.19
0.50	0.24	0.17
1.00	0.23	0.16
1.50	0.22	0.16
2.00	0.18	0.15

Table 2.8. Mean friction coefficients between the powders and the die and core rod surface for standard powder - different geometries.

The data evidence a significantly higher friction coefficient of metal powders with the die surface in comparison to the core-rod. The difference is reasonable since the die is made of WC-Co alloys, while the core-rod is made of tool steel. Hence, the tribological interaction of the metal powders comprehensibly varies in contact with the two surfaces. In the literature the reduction of the friction coefficient on increasing the hardness of the counteract surface is reported [113]. This statement contradicts the results of the present work, being the hardness of WC-Co alloys higher than that of tool steels. However, the same paper proposes an interesting interpretation. The friction coefficient is also influenced by the surface finishing of the compaction tools. In particular, an improvement in the surface finishing appreciably reduces the friction coefficients, what must be taken into account when considering the results reported in figure 2.26 and tables 2.6÷2.8. The surface finishing of die cavity is relatively poor, due to the extensive use. Consequently, μ_{Die} is higher than μ_{Core} . Future studies should measure the roughness of the compaction tools in order to prove this explanation.

Figure 2.26 evidences a dependence of the frictional coefficients on the particle size. Specifically, μ_{Die} markedly reduces on increasing particle size, while the same

trend is less appreciable on μ_{Core} . The poor surface quality of the die might have determined the significant difference among μ_{Die} values obtained for the different particle size. Considering that particle size distribution directly influences the number of powders in contact with the die surfaces, decreasing the average diameter of the powders, the number of interactions with the asperities of the die surface increases, as well as the dissipative phenomena related to the friction coefficient. The larger number of particles in contact with the surface of die cavity might explain the increase of μ_{Die} on decreasing particle size, while μ_{Core} is approximately unaffected by particle size thanks to the better surface finishing.

Friction coefficients are almost unaffected by height in the different particle sizes. In the case of standard powder, height varies in a larger range, and friction coefficients tend to decrease on increasing height. This result might be reasonably related to an increased effectiveness of lubricant with relation to sample height. During compaction of taller samples a more pronounced sliding of powders against the die cavity occurred. The shear force likely determined a local heating, and consequently the softening, or solid to liquid transformation, of the lubricant close to the die walls. The better effectiveness of the lubricant could have determined the lower friction coefficient of higher samples.

2.5.5 Analysis of stresses⁸

The relationships between densification and mean axial stress have been described, for the different geometries and particle sizes. It is important to remind that densification curves were totally derived from the experimental data of force and displacement recorded by the press during the compaction cycle. Since additional measuring equipment was not employed, the radial force constraining the powder compacts in the die was not directly measured. A recursive procedure has been developed in order to estimate the radial stress.

Figure 2.27 reports the mean radial stress versus the relative density for the four particle sizes, and figure 2.28 shows the radial stress of standard powder compacted at different heights.

⁸In this work, the positive stress is conventionally associated to compression. For this reason, the radial stress is expressed through positive values, as the axial stress.

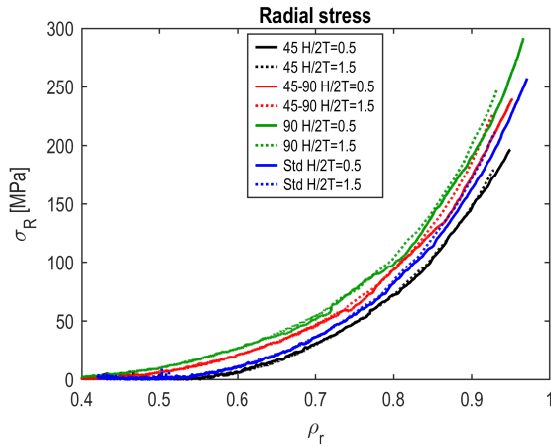


Figure 2.27. Radial stress vs relative density - different particle sizes and height.

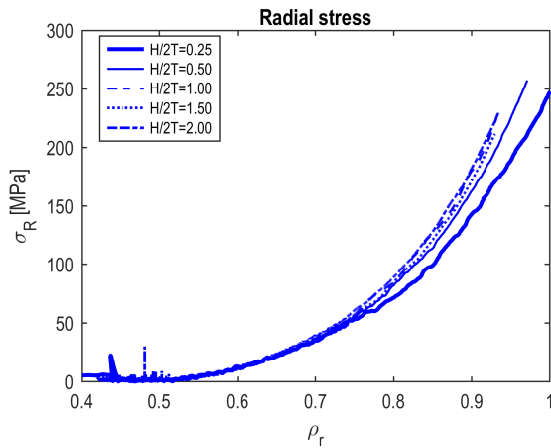


Figure 2.28. Radial stress vs. relative density - standard powder at different heights.

Neglecting the problem of the correct estimation of relative density for sample $H/2T=0.25$ ⁹. The influence of sample height is marginally perceptible as seen on axial stress.

As already observed for axial stress, on increasing particle size the radial stress is larger. As expected, above the elasto-plastic threshold, the radial to axial stress transmission coefficient is not constant, as shown in figures 2.29 and 2.30.

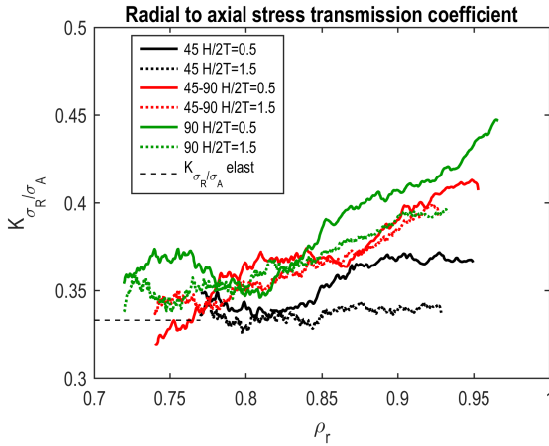


Figure 2.29. Radial to axial stress transmission coefficient vs relative density - different particle sizes and height.

⁹It could be claimed that the die expansion disproves the assumption of negligible radial deformation for samples $H/2T=0.25$. The iterative procedure cannot provide reliable result in this case, and the results associated to this sample are reported to test the limits of the assumptions of the recursive model.

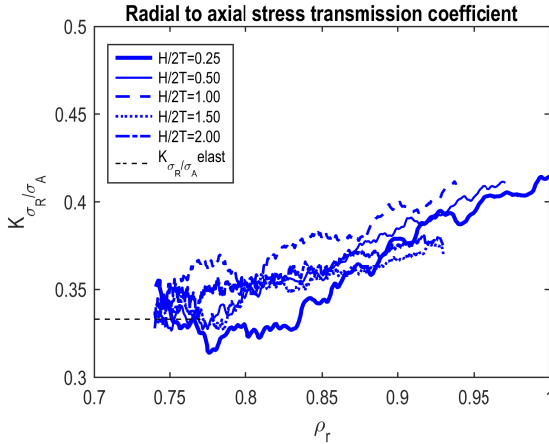


Figure 2.30. Radial to axial stress transmission coefficient vs relative density - standard powder, different heights.

The graphs show the radial to axial stress transmission coefficient K_{σ_R/σ_A} for the different geometries and particle sizes, increasing on increasing the relative density, as expected. However, an oscillating behavior can be recognized, in addition to slight noise.

As mentioned in the description of the methodology, the acquisition of forces and displacements introduced a noise signal, which was superimposed to the actual measurements. However, the irregular behavior showed in figures 2.29 and 2.30 is not ascribable to this problem. The irregularity of the trend is likely due to fluctuations of the die (Z) and core-rod ($Z1$) displacements. Aiming at obtaining the samples by single action compaction, die and core-rod have to be kept firm. This means, from a technological point of view, that the press is set-up imposing a fixed position to the die and core-rod, defined as set position. During compaction, the frictional force transmitted by the powder compacts determines a drift from the set position. Since the press has a close-loop control system on the displacement, a counterbalance force was consequently applied in order to re-establish the die and core-rod positions to the set positions. Therefore, during compaction an imperceptible fluctuation of the die and core-rod position occurred, determining a virtually undetected variation of the F_D and F_C . The oscillation of Z and $Z1$ positions can be observed in figure 2.31. The figure also highlights the influence of the fluctuation of the position on K_{σ_R/σ_A} , and

the amplified fluctuation due to the stress ratio. Nevertheless, it is possible to derive some clear information by the linear regression of the radial to axial stress transmission coefficients shown in figures 2.32 and 2.33.

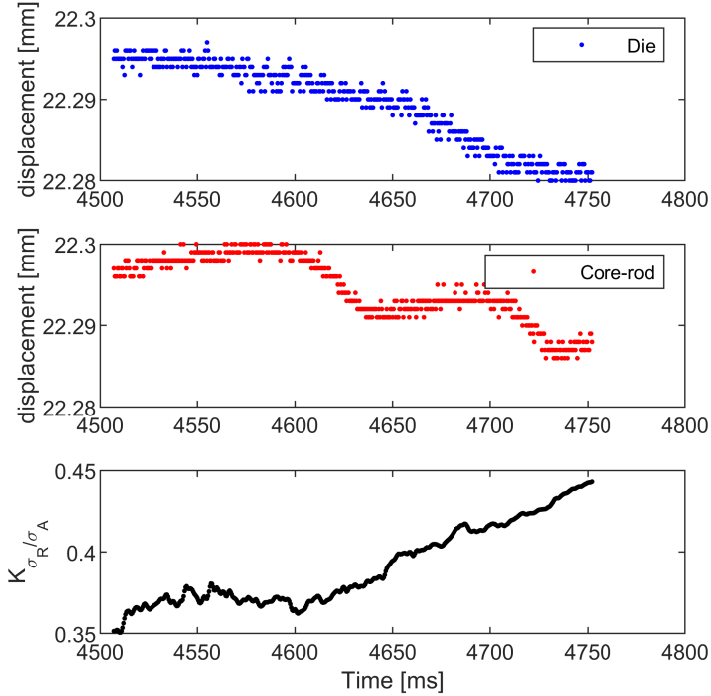


Figure 2.31. Comparison of the displacement fluctuations in the die and core-rod positions - similar behavior observed in the radial to axial stress transmission coefficient.

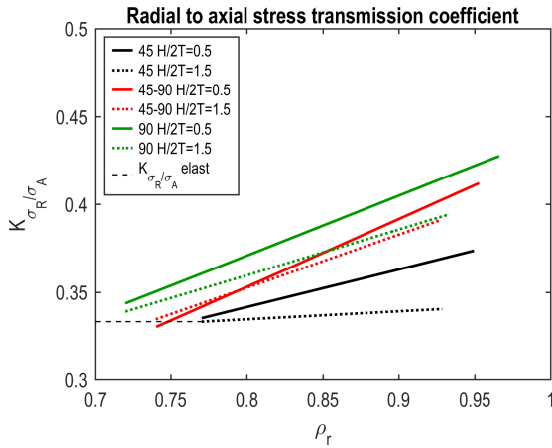


Figure 2.32. Linear regression of the radial to axial stress transmission coefficient vs relative density - different particle size.

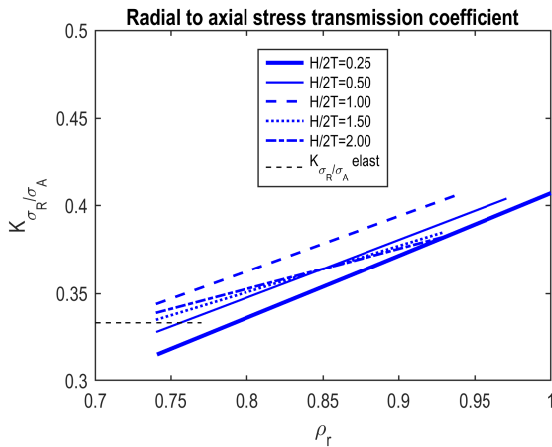


Figure 2.33. Linear regression of the radial to axial stress transmission coefficient vs relative density - standard powder, different heights.

The radial to axial stress transmission coefficient is appreciably lower for the finer particle size (45) with comparison to other particle sizes, showing approximately the same behavior. In addition, a slight influence of sample height can be highlighted.

The effect of geometry on K_{σ_R/σ_A} could likely be attributed to the interparticle friction coefficients, for the same reasons mentioned discussing the compaction curves. The different behavior of finer particle size (45) might be also related to the interparticle friction coefficient. Interparticle friction coefficient is reasonably the same for the four particle sizes, since metal powders and lubricant amount are the same. However, the number of particle contacts per unit of volume drastically increases lowering the average particle diameter. Consequently, a large number of contacts should determine a loss in the axial force transmitted in radial direction, which might justify the evident difference of finer particle size. Despite the standard powder is made of around half 45 and half 45-90 particle size, the radial to axial stress transmission coefficient is more similar to that of the intermediate particle size (45-90). Therefore, it is possible to conclude that the coarser particles play a prevalent role determining the radial to axial stress transmission coefficient. According to this hypothesis, the elasto-plastic transition relative density also depends on the radial stress. This interpretation should be confirmed by further analysis.

In conclusion, lower samples ($H/2T=0.5$ and 1.00) made of standard powder are slightly out of trend, thus highlighting that further work is needed to reliably apply the proposed method to low samples.

Tables 2.9 and 2.10, as well as figure 2.34, show the coefficients of the linear regression describing the radial to axial stress transmission coefficients vs. relative density. It could be observed that the slope tends to decrease on increasing height, while a clear influence of geometry cannot be concluded for the intercept, which varies around 0.33 (value of K_{σ_R/σ_A} in the elastic field, as by the Poisson modulus), due the aforementioned fluctuation of the die and core-rod positions.

$H/2T$	slope	intercept	R-squared-adj
0.25	0.354	0.315	0.829
0.50	0.329	0.328	0.853
1.00	0.313	0.344	0.878
1.50	0.264	0.335	0.800
2.00	0.229	0.339	0.821

Table 2.9. Coefficients of the linear regression describing the radial to axial stress transmission coefficient vs. relative density - standard powder, different heights.

Particle size	$H/2T$	slope	intercept	R-square-adj
45	0.50	0.201	0.340	0.643
45	1.50	0.096	0.331	0.281
45-90	0.50	0.363	0.332	0.906
45-90	1.50	0.301	0.333	0.837
90	0.50	0.358	0.335	0.829
90	1.50	0.288	0.335	0.805

Table 2.10. Coefficients of the linear regression describing the radial to axial stress transmission coefficient vs. relative density - different particle sizes.

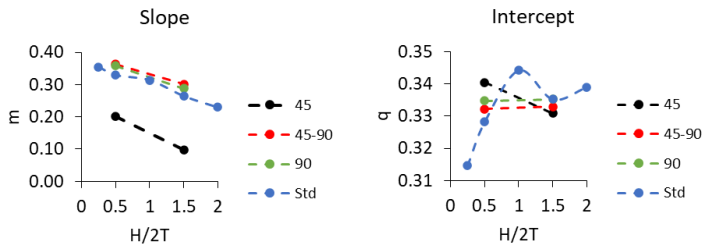


Figure 2.34. Slope and intercept coefficients of the linear regression describing the radial to axial stress transmission coefficient vs. relative density – different heights and particle sizes.

Under the hypothesis of negligible radial deformation of the die cavity, it was concluded that the radial and tangential stresses are equal. Therefore, the principal components of the stress tensor are completely derived, and the deviator stress tensor can be computed. The hydrostatic and the effective stress were calculated by equations (2.35) and (2.36), and the results are shown in figures 2.35 and 2.36.

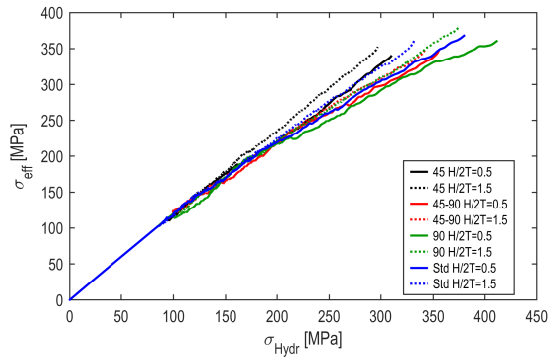


Figure 2.35. Effective stress vs. hydrostatic stress - different particle sizes.

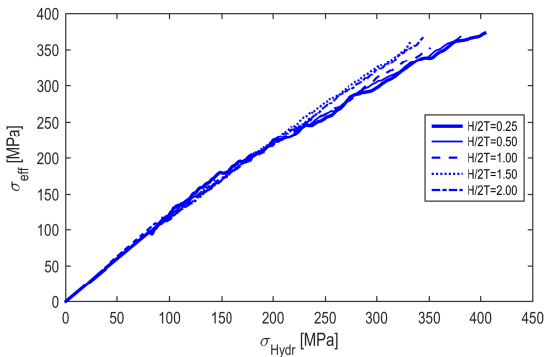


Figure 2.36. Effective stress vs. hydrostatic stress- standard powder, different heights.

The elastic behavior can be observed at low stresses, as characterized by Poisson's ratio determining the radial to axial stress transmission coefficient. Since the same Poisson coefficient was assumed for all the particle sizes, the behavior

is identical for the different particle sizes. Nevertheless, moving to the prevailing plastic deformation, the curves diverge, according to the different radial to axial stress transmission coefficients.

The relationship between hydrostatic and effective stress is fundamental for the constitutive model of materials, as for instance the Cam-Clay or the modified Drucker Prager Cap model. This result represents an added value for this work, looking for the origin of the anisotropic dimensional variation. This point will be discussed after the analysis of the dimensional change on sintering.

2.5.6 Dimensional change on sintering

Tables 2.11 ÷ 2.14 report the green and sintered densities of the samples studied, along with the sintering densification coefficient (Γ) defined by equation (2.45).

$$\Gamma = \frac{\rho_s - \rho_g}{\rho_{316L} - \rho_s} \quad (2.45)$$

$H/2T$	ρ_g [g/cm ³]	ρ_s [g/cm ³]	Γ
0.25	6.73	7.01	0.26
0.50	6.66	6.98	0.28
1.00	6.66	6.86	0.18
1.50	6.61	6.86	0.21
2.00	6.65	6.84	0.17

Table 2.11. Green and sintered densities, and densification coefficient - standard powder, different geometries.

$H/2T$	ρ_g [g/cm ³]	ρ_s [g/cm ³]	Γ
0.50	6.60	6.94	0.40
1.50	6.60	6.91	0.35

Table 2.12. Green and sintered densities, and densification coefficient – particle size 45, different geometries.

$H/2T$	ρ_g [g/cm ³]	ρ_s [g/cm ³]	Γ
0.50	6.63	6.81	0.18
1.50	6.63	6.76	0.13

Table 2.13. Green and sintered densities, and densification coefficient – particle size 45-90, different geometries.

$H/2T$	ρ_g [g/cm ³]	ρ_s [g/cm ³]	Γ
0.50	6.72	6.84	0.13
1.50	6.66	6.79	0.13

Table 2.14. Green and sintered densities, and densification coefficient – particle size 90, different geometries.

The densification coefficient (Γ) is higher for the finer particle size, and possible explanation will be given in the following. However, it is important to highlight that the different densification behavior of the different particle sizes is totally independent on the green density, because all samples were compacted at the same green density of 6.6 g/cm³.

The ring-shaped samples were measured in the green and sintered state, and the dimensional variations on sintering were computed for the four particle sizes. Figures 2.37 and 2.38 report the dimensional change of: external and internal diameters, thickness, average diameter, height and isotropic dimensional variation, as calculated by equations (2.37 ÷ 2.41, 2.44).

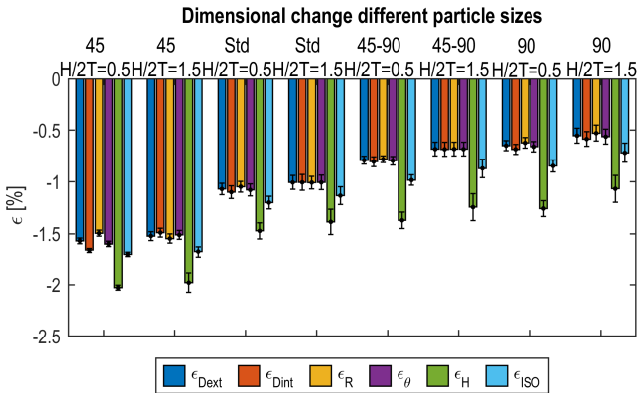


Figure 2.37. Dimensional change of: external diameter, internal diameter, thickness, average diameter, height and ϵ_{ISO} - different particle sizes, different geometries.

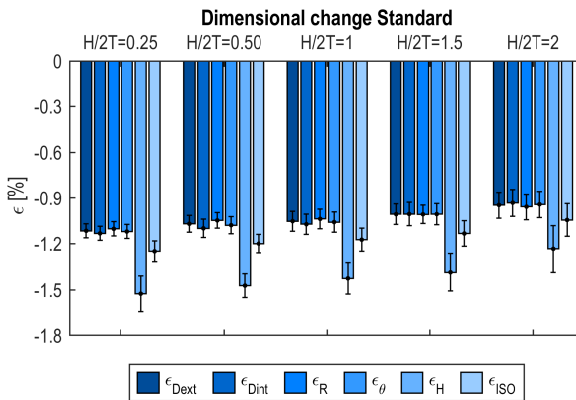


Figure 2.38. Dimensional change of: external diameter, internal diameter, thickness, average diameter, height and ϵ_{ISO} - standard powder, different geometries.

Clear anisotropy of the dimensional variation is highlighted, as expected. Height shrinks more than diameters, as commonly observed in solid-state sintering. The dimensional variation in the compaction plane is practically isotropic, except for a slightly higher shrinkage observed for the internal diameter in some cases.

Figure 2.37 clearly evidences the larger shrinkage on decreasing particle size. As by the literature, the specific surface area grows up, on decreasing particle size. Since the specific surface area is the driving force of the sintering process, fine particle size determines larger densification. The shrinkage of the standard powder is in-between the shrinkage of 45-90 and 45 particle sizes, as expected considering the particle size distribution of standard powder.

No significant effect of height on dimensional change can be highlighted. However, the analysis of the numerical data highlights slightly lower shrinkage for the highest samples, specifically for the $H/2T=1.5$ and 2 samples. Probably the different shrinkage has to be related to the effective isothermal holding time during the sintering operation. All samples were sintered in the same batch, in vacuum, so the samples were mainly heated by thermal irradiation. It is widely recognized that the heating rate is inversely proportional to the surface to volume ratio of the sample. Consequently, the tallest sample might have reached the isothermal sintering condition later than other geometries. This would imply a short permanence at the sintering isothermal condition, which might imply a consequent minor densification. Comparing the densities reported in tables 2.11 ÷ 2.14, lower sintered density of samples $H/2T=1.5, 2$ is reported, thus proving this explanation. In the future, the effective temperature of the samples during the sintering cycle should be measured to confirm this interpretation.

The anisotropy of the dimensional changes depends on particle size. Two coefficients are proposed to evaluate the anisotropy of the dimensional variation, defined by equations¹⁰ (2.46) and (2.47). The coefficients will be specifically defined in the following, they are used here in advance because they allow an effective comparison among the different particle sizes. The outcomes are shown in figure 2.39.

$$K_{anis} = \frac{\sqrt{(\varepsilon_R + 1)(\varepsilon_\theta + 1)} - (\varepsilon_{ISO} + 1)}{\varepsilon_{ISO}} \quad (2.46)$$

¹⁰The equation (2.46) will be defined in depth in section 3.3.

$$W_{anis} = \frac{(\varepsilon_H - \varepsilon_R)}{\varepsilon_{ISO}} \quad (2.47)$$

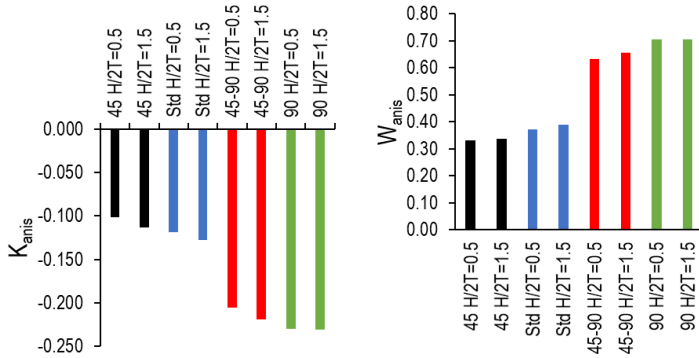


Figure 2.39. Anisotropy coefficients calculated by equations (2.46) and (2.47) for the four particle sizes.

The influence of particle size on the dimensional variation on sintering is extensively studied on literature, but it is not the same for the effect on the anisotropy (of dimensional variation). An interesting example is presented in [137]. The experimental results presented in this study show that the addition of fine spherical powders to commercial powder blend determined an increase of the radial to axial shrinkage ratio. The paper suggested that finer spherical powders might have determined a large number of particle contacts in axial and radial direction, which might have reduced the anisotropy of dimensional variation. Another possible explanation could be related to the preferential alignment of elongated particles and pores in the green state [79, 82, 92, 93]. Therefore, the substitution of irregular shaped particles with spherical ones might reduce the formation of the aligned structure during the compaction process.

The above interpretation might be helpful discussing the results shown in figure 2.39. The high anisotropy of coarse particle sizes (45-90, 90) could be related to the highly irregular powder shape in the as-built state, which in turn might determine the preferential alignment of particles and pores causing the high anisotropic coefficient. On the other side, finer particles might have a relatively spherical shape, so that a less oriented structure should be obtained at the end of compaction, and consequently the

lower anisotropy. Same for standard powder, due to the high amount of fine particles in the powder. Future analysis might compare the shape factors of particles before and after compaction in order to confirm:

1. decrease of the aspect ratio and increase of the irregular surface in coarse particles,
2. appreciable increase of particles and pores alignment in coarse particle size green compacts.

In order to investigate accurately the dimensional change in the transversal plane, the external and internal diameter were measured at different levels, 1/4, 2/4, and 3/4 of height, respectively. The height fraction refers to the distance from the surface of the sample contacting the lower punch (bottom surface) during compaction. Figures 2.40–2.43 show the dimensional change of: diameters, thickness and average diameter at the three height levels. In addition, in each plot the dimensional variation of the diameter of the reconstructed cylinder¹¹ is reported as reference.

The results do not show a clear trend for the smaller rings, the shrinkage at the three levels is practically the same. The result may be ascribed to the negligible stress gradient, and consequently density gradient, in low samples. A slight trend is instead observed for the tallest samples, where the dimensional change grows up moving away from the bottom surface, for all the three particle sizes. An inverse trend is instead observed for standard powder. The discrepancy might be associated to the sample orientation in the furnace (bottom plane might not be in contact with the furnace plates).

The gradient of shrinkage along the sample axis results from different mechanisms. The gradient of axial stress determines lower density close to the bottom surface, thus in principle higher surface energy and higher shrinkage. Nevertheless, the influence of spring-back after ejection must be considered, which determines an opposing, and in this case likely larger, effect. Further work will investigate a high number of samples and densities in order to identify a clear trend.

¹¹The diameters of the reconstructed cylinders (internal and external) were computed by the least squares best fit cylinder reconstruction of the three circle scans. The results have been presented in figures 2.37 and 2.38.

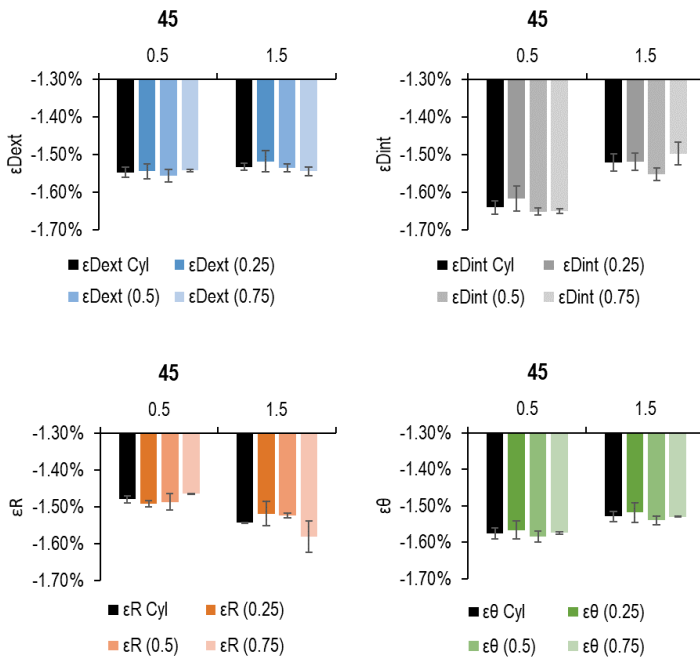


Figure 2.40. Clockwise: dimensional variation of external diameter, internal diameter, tickness and average diameter for the smaller particle size (45).

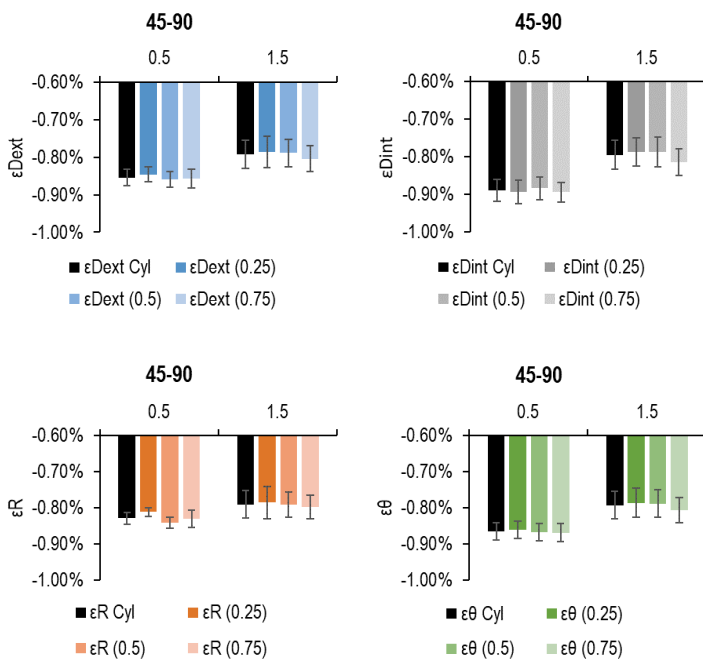


Figure 2.41. Clockwise: dimensional variation of external diameter, internal diameter, thickness and average diameter for the intermediate particle size (45-90).

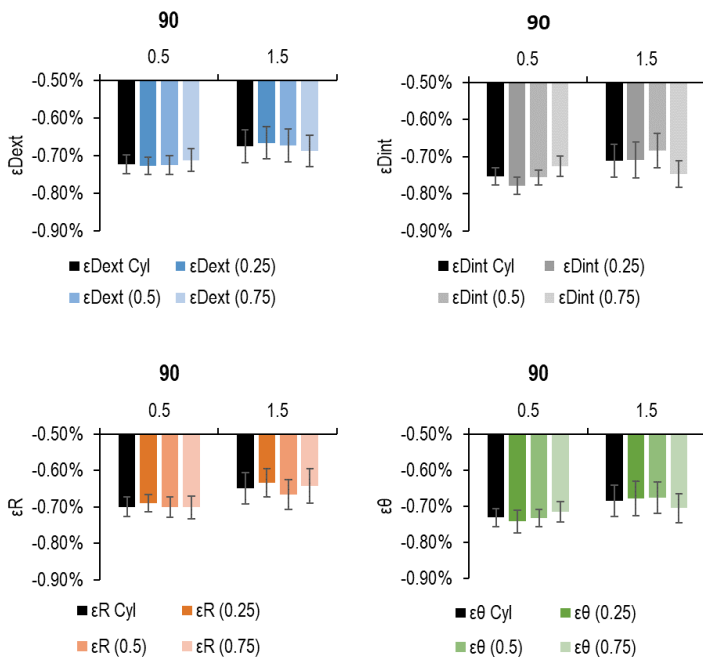


Figure 2.42. Clockwise: dimensional variation of external diameter, internal diameter, thickness and average diameter for the bigger particle size (90).

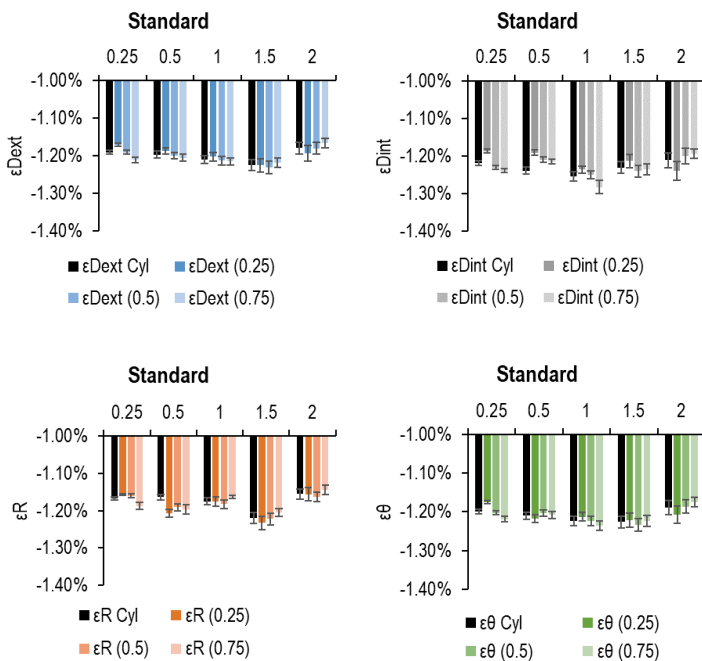


Figure 2.43. Clockwise: dimensional variation of external diameter, internal diameter, thickness and average diameter for the standard powder.

2.5.7 Compaction stress field and sintering shrinkage

Compaction mechanics and dimensional variation on sintering were analyzed in the previous paragraphs, now the triaxial state of stress is related to the anisotropic dimensional changes.

Figure 2.44 shows the dimensional variation of height and thickness¹² as function of the maximum axial and radial stresses in compaction. The figure clearly shows a proportional relationship between stress and shrinkage along the two principal directions for each particle size. However, the lines are not perfectly overlapped and the influence of height is highlighted in the coarser particle sizes, as well as in the standard powder highest samples.

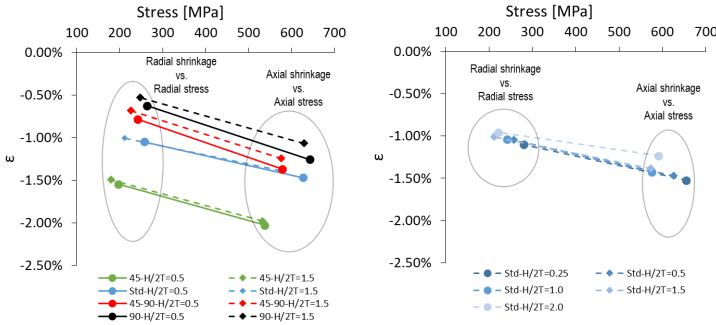


Figure 2.44. Dimensional changes vs. compaction stresses for the different particle size (on the left) and for the standard powder (on the right).

In order to better evidence the role of uniaxial compaction on the origin of anisotropic dimensional variation, the “deviatoric” axial ($\varepsilon_{H,dev}$) and radial ($\varepsilon_{R,dev}$) shrinkage were calculated by equations (2.48) and (2.49):

$$\varepsilon_{H,dev} = \varepsilon_H - \varepsilon_{ISO} \quad (2.48)$$

$$\varepsilon_{R,dev} = \varepsilon_R - \varepsilon_{ISO} \quad (2.49)$$

¹²It was observed that the dimensional change in the compaction plane is isotropic, therefore the radial stress can be related with ε_R of ε_θ . ε_R has been used, corresponding to the effective dimension defining the volume of powder.

The deviatoric stress represents the deviation of the stress from the hydrostatic behavior, so the deviatoric shrinkage would similarly identify the deviation from the isotropic dimensional change. The results of equations (2.48) and (2.49) are shown as a function of the deviatoric stress in figure 2.45.

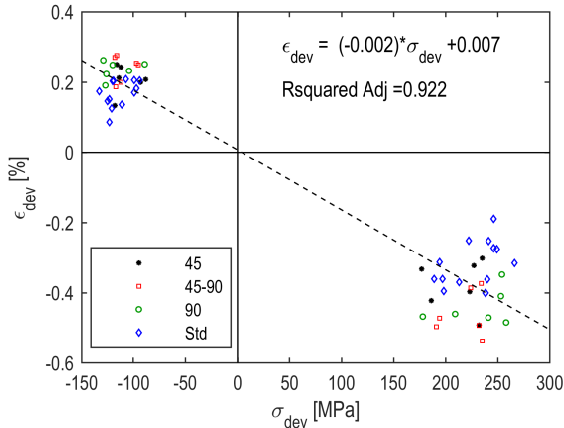


Figure 2.45. Deviatoric shrinkage versus deviatoric stress for the different particle size and geometry.

As by figure 2.45, a linear relationship between the deviatoric stress and the deviatoric shrinkage can be derived. When the deviatoric stress is positive, the deviatoric shrinkage is negative and vice versa. This means that a positive deviatoric stress would determine a shrinkage higher than the isotropic dimensional change in the considered direction, while a negative deviatoric stress would imply a lower dimensional change.

The experimental data were fitted by a linear regression, intercept close to zero. This result can be interpreted as follows. Would the triaxial stress field be hydrostatic, then isotropic dimensional variation would occur. This conclusion finds experimental evidence in samples produced by cold isostatic pressing, where the triaxial stress field is practically isotropic, as well as the dimensional variation [55]. Therefore, it might be concluded that the deviatoric stress components determine the anisotropic dimensional variation.

However, the linear regression of data is not completely satisfactory. The analysis of the residuals in figure 2.46 highlights the large scatter between the actual values

and the values predicted by the linear regression.

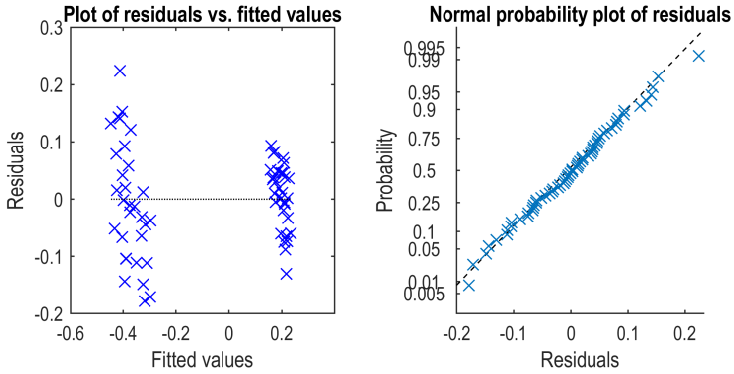


Figure 2.46. Residuals versus the fitted values (on the left) and probability distribution of residuals obtained by the linear regression of data displayed on figure 2.45 (on the right).

Aiming at obtaining a more reliable relationship, an alternative analysis was performed. Two new anisotropy coefficients were computed by equations (2.50) and (2.51). These coefficients represent the deviatoric shrinkage along axial (G_H) and radial direction (G_R).

$$G_H = \frac{\varepsilon_H - \varepsilon_{ISO}}{\varepsilon_{ISO}} \quad (2.50)$$

$$G_R = \frac{\varepsilon_R - \varepsilon_{ISO}}{\varepsilon_{ISO}} \quad (2.51)$$

The results of the new equations were related to the deviatoric stress in axial and radial direction divided by the hydrostatic stress, as shown in figure 2.47 for each particle size.

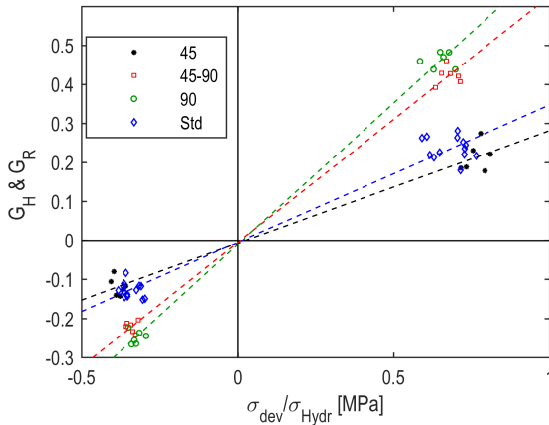


Figure 2.47. Anisotropic coefficient along axial (G_H) and radial (G_R) direction versus the axial and radial deviatoric stress normalized by the hydrostatic stress.

Linear relationships between the deviatoric stresses and the deviatoric dimensional change coefficients, specific for the different particle sizes, are identified in figure 2.47. Table 2.15 reports the slope and intercept determined by the linear regression for the four particle sizes.

Particle size	slope	intercept	R-squared-adj
45	0.290	-0.007	0.968
45-90	0.633	-0.006	0.995
90	0.726	-0.011	0.993
Standard	0.353	-0.005	0.972

Table 2.15. Slope, intercept and R-squared-adjusted coefficients determined by the linear regression of data displayed in figure 2.47 for the four particle sizes.

The residuals of the linear regression drastically improved, and further studies will enlarge the experimental data in order to confirm the trend.

The anisotropy coefficients shown in figure 2.39 are higher for the coarser particle sizes, and the reason was ascribed to the powder morphology. This explanation does

not conflict with the new interpretation based on the relationship between deviatoric shrinkage and deviatoric stress, as explained in the following.

In [85] the uniaxial compaction of spherical particles was simulated. The calculation showed a significant increase of powder contacts in axial direction than in transversal one. On the basis of this result, the origin of the anisotropic dimensional variation is ascribed to the inhomogeneity of stress field in uniaxial compaction. This interpretation agrees with the actual conclusion that the absolute deviatoric shrinkage increases on increasing the deviatoric stress.

The theoretical model in the paper mentioned above is developed on spherical particles, does not consider the actual powder shape in the as-built state. The compaction process determines the plastic deformation of the metal particles, but in the first step of compaction it might also cause the alignment of the particles during rearrangement. In this initial phase, the powders could rotate and slide in order to reach a denser configuration. Before the beginning of plastic deformation, it is reasonable to suppose that particles and pores already present an alignment favoring the inhomogeneity between axial and radial stress. The analysis of the literature on ceramic materials corroborates this hypothesis, since anisotropic dimensional change is also observed after uniaxial compaction of elongated particles. Since no plastic deformation occurred on ceramic materials, the alignment of the particle structure is clearly caused by the rearrangement during compaction.

Summarizing, the anisotropic dimensional variation is certainly originated by the inhomogeneity of stress field in compaction. Conventional metal powders used in P&S are slightly elongated in as-built state. After rearrangement in the compaction process, the particles likely show a preferential alignment due to the different components of principal stresses. Subsequently, during plastic deformation the stress field promotes an increment of the contact area between powders, which is more relevant in axial than radial direction, again on the basis of the inhomogeneity of the stress field. Therefore, during the sintering process, the structural and geometrical activities promote a more evident shrinkage on the bigger contact area. It might be concluded that deviatoric stress field originates the anisotropic dimensional change. The intensity of the dimensional change depends on:

- the grade of particle orientation during the rearrangement,
- the absolute deviatoric stress component,
- the base material, meaning the irregularity of the particle shape in the as-built state.

- The sintering conditions (temperature and time).

If the validity of the proportional behavior presented on figure 2.47 is confirmed, this might represent an interesting opportunity for sintering simulation. In fact, the stress field in compaction can be quite easily modelled by continuum mechanics. The simulation of the stress-strain behavior occurred during compaction would provide the map of the deviatoric stress field in the component. This map would be the input parameter to calculate the anisotropy coefficients G_H , G_R using the proposed linear regression on each node. Subsequently, knowing the isotropic dimensional change, the sintered dimensions could be easily derived. Further work will investigate the compaction mechanics and sintering dimensional change of a multilevel geometry in order to verify the effectiveness of this model.

2.6 Conclusion

The present work investigated the compaction mechanics and the sintering dimensional change of ring-shaped samples. Standard commercial powder was sieved in three particle sizes: lower than $45\ \mu\text{m}$, bigger than $90\ \mu\text{m}$ and the intermediate one. The three particle sizes and the standard powder were mixed with 0.6% of Acrawax lubricant and further compacted in ring-shaped samples having different heights. The samples were produced by single action compaction in order to exploit the data continuously recorded by the press to derive the compaction mechanics relationships. After compaction, the samples were sintered in a batch furnace.

The analysis of the compaction mechanics reveals a significant influence of the particle size and minor effect of sample geometry on the compressibility of metal powders. Increasing the particle size, high densification is observed, which has been ascribed to the lower starting density. Higher samples required a slightly higher axial pressure in order to reach an equivalent green density, due to the enhanced dissipative phenomena. The mean radial stress derived from an iterative procedure is less than half the mean axial pressure, thus confirming the expected inhomogeneity of the stress field. The radial stress is also affected by the particle size and sample geometry, even if less evidently than the axial stress. The radial to axial stress transmission coefficient is also influenced by particle size and geometry, through the interparticle friction and the number of particle contacts in the compaction section. The friction coefficient between the powders and the die and core-rod surfaces have been also derived, revealing an increase of the friction coefficient on decreasing particle size and increasing sample height. The surface finishing of die and core rod also plays a significant role on friction coefficients.

The measurement of the dimensions of the samples at the green and sintered state quantified the dimensional changes on sintering. The dimensional changes are smaller on increasing the particle size. A slightly lower shrinkage occurred on tallest samples, maybe due to a lower permanence at the isothermal sintering stage caused by the higher volume to surface ratio.

Generally, the shrinkage is higher in the direction parallel to the compaction direction, than in the compaction plane, in agreement with the anisotropic dimensional variation expected in solid-state sintering. Significantly larger anisotropic dimensional change was observed in coarser particle size. The relationship between deviatoric stress and deviatoric shrinkage supports the hypothesis that the inhomogeneity of the triaxial stresses originates the anisotropic dimensional change. However, further

analysis demonstrated that the anisotropic behavior occurred on different particle sizes cannot be completely referred to the intensity of the deviatoric stress, due to the influence of the irregular shape of the powder particles in the as-built state. During compaction, the applied pressure could determine an initial rearrangement of the elongated particles in a preferential orientation, whereas in the plastic domain, the triaxial stress field might promote a higher increment of longitudinal than transversal contacts. In conclusion, the anisotropic of the dimensional changes might be linearly dependent on the inhomogeneity of the stress field, but the influence of particle size and particle size distribution has also to be considered.

3 Part B: Design method accounting for the anisotropic dimensional change on sintering

3.1 Aim of the work

The development of a new product involves several design aspects. The new component must provide some functions, whose mechanical strength and correct assembly are the predominant ones in the case of structural parts. In order to satisfy these functional requirements, proper shape must be defined in accordance with the material properties, the production process, the economic affordability, the lifespan of the product, and other aspects. On the development of a new P&S product, all these aspects should be considered during the integrated product process development. This chapter will focus on the need for designing the shape considering the dimensional change occurred in the different stages of the production process. A design procedure accounting for the anisotropic dimensional change on sintering is presented and tested on real industrial parts.

3.2 Introduction

In conventional P&S technology, the dimensional change of the product occurs both in the compaction and in the sintering process¹³. During compaction, metal powders are plastically deformed by triaxial state of stress. When the applied load is removed and the part is ejected out of the die cavity, the compact recovers the elastic deformation in axial and radial direction, this is generally called “spring-back”. The elastic recovery causes an expansion of all the dimensions, except for the diameter of the holes, which generally shrink. As described in depth in chapter 1, further anisotropic dimensional change occurs on sintering, depending on the prior uniaxial compaction, and it is different in radial and axial directions.

As mentioned in section 1.3, the actual dimensional change can be split in an average (absolute) variation \pm a deviation attributable to the process capability. The absolute dimensional change can be partially controlled in the design phase and adjusted in the set-up of the P&S process. For instance, powder mix which guarantees high stability can be chosen developing a new product, or the sintering temperature and time can be modified during the set-up of the process. However, the modification of the sintering procedure is limited by the achievement of the metal densification and

¹³Secondary operations can also modify the product geometry but they are not considered in this analysis.

the required mechanical resistance. Therefore, in order to guarantee the dimensional precision of P&S products, the correct design of the compaction tools (die, punches, core-rod) is crucial. The dimensions of compaction tools are designed considering:

- the product specification (drawing dimensions and tolerances);
- dimensional change of the product during the compaction and sintering processes.

Accounting for the different dimensional changes in P&S process, the die cavity can be designed according to figure 3.1.

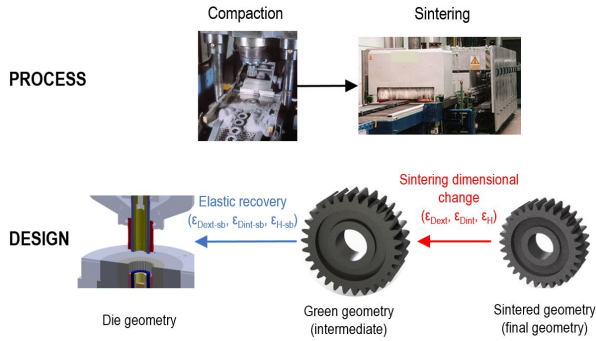


Figure 3.1. Schematic representation of the dimensional changes occurred during the production process to be used designing the die cavity.

A ring-shaped geometry is considered. The nominal dimensions of the external ($D_{ext,nom}$) and internal ($D_{int,nom}$) diameters, and the height (H_{nom}) are specified in the drawing. Disregarding secondary operations, at the end of sintering the dimensions ($D_{ext,s}$, $D_{int,s}$, H_s) should be equal to the nominal ones, in the range of capability of the process. Providing that the relationships between the green and sintered dimensions, both for diameters ($\varepsilon_{D_{ext}}$, $\varepsilon_{D_{int}}$) and height (ε_H), are known and expressed by equations (3.1÷3.3), then the green dimensions ($D_{ext,g}$, $D_{int,g}$, H_g) can be determined by equations (3.4÷3.6).

$$\varepsilon_{D_{ext}} = \frac{D_{ext,s} - D_{ext,g}}{D_{ext,g}} \quad (3.1)$$

$$\varepsilon_{D_{int}} = \frac{D_{int,s} - D_{int,g}}{D_{int,g}} \quad (3.2)$$

$$\varepsilon_H = \frac{H_s - H_g}{H_g} \quad (3.3)$$

$$D_{ext,g} = \frac{D_{ext,s}}{1 + \varepsilon_{D_{ext}}} = \frac{D_{ext,nom}}{1 + \varepsilon_{D_{ext}}} \quad (3.4)$$

$$D_{int,g} = \frac{D_{int,s}}{1 + \varepsilon_{D_{int}}} = \frac{D_{int,nom}}{1 + \varepsilon_{D_{int}}} \quad (3.5)$$

$$H_g = \frac{H_s}{1 + \varepsilon_H} = \frac{H_{nom}}{1 + \varepsilon_H} \quad (3.6)$$

In the same way, if the elastic recovery due to spring-back of the green dimensions is known and expressed by equations (3.7÷3.9), then the diameters ($D_{ext,situ}$; $D_{int,situ}$) and the height (H_{situ}) of the ring inside the die cavity can be determined by equations (3.10÷3.12).

$$\varepsilon_{D_{ext-sb}} = \frac{D_{ext,g} - D_{ext,situ}}{D_{ext,situ}} \quad (3.7)$$

$$\varepsilon_{D_{int-sb}} = \frac{D_{int,g} - D_{int,situ}}{D_{int,situ}} \quad (3.8)$$

$$\varepsilon_{H-sb} = \frac{H_g - H_{situ}}{H_{situ}} \quad (3.9)$$

$$D_{ext,situ} = \frac{D_{ext,nom}}{(1 + \varepsilon_{D_{ext-sb}})(1 + \varepsilon_{D_{ext}})} \quad (3.10)$$

$$D_{int,situ} = \frac{D_{int,nom}}{(1 + \varepsilon_{D_{int-sb}})(1 + \varepsilon_{D_{int}})} \quad (3.11)$$

$$H_{situ} = \frac{H_{nom}}{(1 + \varepsilon_{H-sb})(1 + \varepsilon_H)} \quad (3.12)$$

According to these relationships, the dimensions of the compact inside the die cavity can be calculated. In addition, hypothesizing that the in-situ diameters of the compact are equal to the diameters of the die and core, the die cavity can be designed. The same procedure can be applied to a more complex shape in order to determine the diameters of die and punches. The die height is designed on the basis of the filling

height, derived by equation (1.1) and the displacement and stiffness of the punches during the compaction cycle.

The knowledge of the dimensional changes in P&S process is thus needed for an effective design of the compaction equipment. However, it is difficult to predict the dimensional change of a new product, depending on the material, the product geometry and the set-up of the process.

Despite the lack of a complete comprehension of the spring-back, the major problem in industrial production is related to the anisotropic dimensional change on sintering. In sections 1.2.3 and 1.5 the most promising models for simulating the dimensional variation on sintering were presented. In spite of the solid physical background, these models are currently not adequate for practical design procedure, mainly due to the following reasons:

- the models need for material constants not available in literature,
- few models could predict the anisotropic dimensional change and shape distortion for complex geometries.

Due to these limitations, in industrial practice the die cavity is generally designed on the basis of company know-how, and adjusted by trial and error iterative procedure. This procedure is not accurate, and dramatically time consuming, generally lasting 12÷16 months before starting with the production of the new part [138, 139]. In addition, the high cost of compacting equipment affects the overall design process. Die and other tools are made of valuable materials, and they are manufactured by special forming technology in order to reach tight tolerances and outstanding surface finishing. The die is generally made of cemented carbide, whereas punches and core-rod are formed by tool steel. Cemented carbide offers a superior wear resistance and stiffness, whereas tool steel is an optimal compromise among toughness, stiffness, and wear resistance. Therefore, these materials are particularly suitable for P&S large production series, because they maintain the dimensional precision and surface finishing longer in time. However, the iterative design procedure can require reshaping operation or, in the worst case, the disposal of tools in favour of a new geometry, thus determining a dramatic increase of the design cost, which is later spread on the cost of the product.

Aiming at determining an effective design procedure for P&S products, Cristofolini et al has been developing a new design methodology, accounting for the anisotropy of dimensional change. The anisotropy of dimensional variations was studied in

order to highlight the contribution of: material, geometry and process conditions. Several powder mixes were investigated in order to study the influence of material on the sintering mechanisms and the related dimensional change. In previous works, Fe-Cr-Mo-C [140] and pure iron mixed with P additive [141, 142] were investigated. In these powder mixes the dimensional change led to shrinkage, induced by solid state sintering mechanism. Whereas, the analysis of other powder mixes composed by: Fe-Cu-P [143] and Fe-Cu-C [144, 145] displayed swelling or shrinkage on account of the copper content. The influence of the alloying elements on the dimensional change is undisputable, and further analysis showed an additional effect of the alloying method [140].

The role of process parameters on dimensional variation was also investigated. In [146] the influence of green density on the anisotropic dimensional change was studied. At low green density the diameters shrink more than height, while an opposite trend was observed at high density. In [147] the increase of sintering temperature was investigated, highlighting that very high sintering temperature determine the expected increase of dimensional changes, along with an unexpected decrease of anisotropy. In further works the role played by the geometry of the components on the anisotropic dimensional variation was also studied [141, 148]. The relationship between density distribution and dimensional variations was studied in [146].

All of this knowledge, based on a huge experimental work, was collected in order to develop an analytical design method accounting for the anisotropy of dimensional change.

In the following sections, the design procedure is described in depth. The results of the DfS project are discussed within the limits of confidential agreements.

3.3 Design procedure

This section describes:

- the assumptions of the design procedure,
- the analytical equations,
- the empirical relationships accounting for the sintering anisotropy derived from experimental evidence.

Different experimental campaigns were performed in the past, so the derived empirical relationships used in the design procedure may slightly differ. For this reason, two alternative databases can be used, according to the material investigated. Finally, it is explained how the dimensional variation of a complicate axial-symmetric part can be predicted by means of break down approach and further assembly of ring-shaped elements.

The current design procedure has been developed for axi-symmetric geometry because this is the basic shape for most of P&S parts, as displayed in figure 3.2.



Figure 3.2. Example of axial-symmetric components produce by P&S [149].

Pulleys, sprockets, hubs, support brackets, gears, rotors, clutch hubs, synchronizer hubs, shock absorbers are some examples of axi-symmetric structural parts produced by P&S. A symmetric profile is particularly suitable and adequate in accordance to P&S design guidelines¹⁴. The reason depends mainly on the compaction procedure. An axi-symmetric die cavity can be easily filled with powders. The stress field is more homogeneous and theoretically independent on the position in the compaction plane.

¹⁴Design guidelines accounting for the P&S process capability can be found in [150, 151].

The design procedure was thus developed for disks and ring-shaped geometries. Cylinder and ring correspond to the simplest geometrical units having an axisymmetric shape. For this reason, the dimensional change on sintering was initially investigated in these geometries, in order to investigate the influence of material, geometry and process parameters.

The dimensional variation of diameters and height can be computed by equations (3.1÷3.3), whereas, the change in volume and the radial and tangential dimensional changes of a ring can be calculated by equations (3.13÷3.15):

$$\varepsilon_V = \frac{V_s - V_g}{V_g} \quad (3.13)$$

$$\varepsilon_R = \frac{Th_s - Th_g}{Th_g} \quad (3.14)$$

$$\varepsilon_\theta = \frac{D_{avg,s} - D_{avg,g}}{D_{avg,g}} \quad (3.15)$$

Where:

- Th is the thickness calculated by the difference between external and internal radii;
- D_{Avg} is the average diameter calculated as the mean value between the external and internal diameters.

The subscripts g and s refer to green and sintered parts, respectively.

At this point, the first fundamental hypothesis of the design methodology is introduced. The model assumes a negligible volume distortion on sintering, which implies that the volume change can be correlated to the dimensional variations, as expressed by (3.16).

$$(\varepsilon_V + 1) = (\varepsilon_R + 1) (\varepsilon_\theta + 1) (\varepsilon_H + 1) \quad (3.16)$$

In order to identify a reference parameter for the anisotropy, the isotropic dimensional change (ε_{ISO}) is defined by equation (3.17).

$$\varepsilon_{ISO} = \sqrt[3]{(\varepsilon_V + 1)} - 1 \quad (3.17)$$

Under the hypothesis of isotropic dimensional change, the dimensional variation defined by equations (3.3, 3.14÷3.15) are equal to the isotropic dimensional change, as expressed by equation (3.18).

$$\varepsilon_{ISO} = \varepsilon_H = \varepsilon_R = \varepsilon_\theta \quad (3.18)$$

Combining equations (3.16) and (3.17), it is possible to derive equation (3.19), which represents the relationship between the dimensional change in the compaction direction (on the left) and in the compaction plane (on the right), as derived from the change in volume.

$$\sqrt{\frac{(\varepsilon_{ISO} + 1)^3}{(\varepsilon_H + 1)}} = \sqrt{(\varepsilon_R + 1)(\varepsilon_\theta + 1)} \quad (3.19)$$

The proposal for quantification of the anisotropic dimensional change is based on this distinction. The graph in figure 3.3 reports the left and right terms of equation (3.19) in the y-axis and x-axis of the plot, respectively.

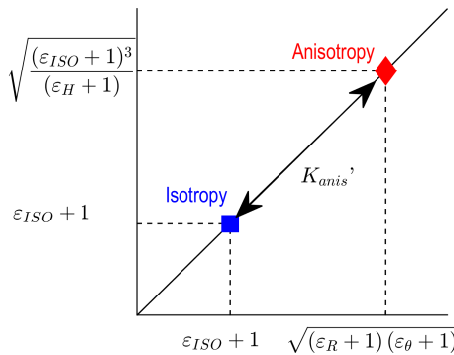


Figure 3.3. Graphical representation of the anisotropy of dimensional changes.

By definition, in figure 3.3 the points satisfying equation (3.19) belong to the bisector line. Along this line, it is possible to theoretically identify a point representing the isotropic condition (dimensional changes in the compaction plane equal to dimensional change in the compaction direction), as defined by equation (3.18).

The point representing the actual anisotropic dimensional changes is shown in figure 3.3 on the bisector line at a certain distance from the isotropic condition. This distance is an entity quantitatively representing the anisotropic dimensional change, so it is defined in the model as the anisotropy coefficient K'_{anis} which corresponds to the distance between the points on the graph representing the isotropic and anisotropic

conditions. The resulting expression of K'_{anis} is reported on equation (3.20).

$$K'_{anis} = \sqrt{2} \left[\sqrt{(\varepsilon_R + 1)(\varepsilon_\theta + 1)} - (\varepsilon_{ISO} + 1) \right] \quad (3.20)$$

The parameter K'_{anis} normalized by ε_{ISO} , K_{anis} as expressed by equation (3.21), provides an anisotropy parameter independent on the absolute dimensional change .

$$K_{anis} = \frac{\sqrt{(\varepsilon_R + 1)(\varepsilon_\theta + 1)} - (\varepsilon_{ISO} + 1)}{\varepsilon_{ISO}} \quad (3.21)$$

Defining the geometrical parameter R given by equation (3.22), equation (3.21) can be expressed as a function of the dimensional change of external and internal diameter of a ring-shaped, as by equation (3.23).

$$R = \frac{D_{int,g}}{D_{ext,g}} \quad (3.22)$$

$$K_{anis} = \frac{\sqrt{\frac{(\varepsilon_{Dext} + 1)^2 - R^2 (\varepsilon_{Dint} + 1)^2}{1 - R^2}} - (\varepsilon_{ISO} + 1)}{\varepsilon_{ISO}} \quad (3.23)$$

A second anisotropic parameter was introduced in the design model to consider any anisotropy in the compaction plane. This parameter is called α and expresses the difference of the dimensional change of the external and internal diameter. Two similar mathematical relationships of α were derived fitting experimental data, as derived considering large change in volume ($|\varepsilon_{ISO}| > 1\%$) and small change in volume ($|\varepsilon_{ISO}|$ close to 0%).

3.3.1 Design procedure for large change in volume

Large change in volume was observed for Fe-Cu alloys as reported in [141]. In this study, the anisotropic dimensional change in the compaction plane (α) was identified by equation (3.24).

$$\alpha = \frac{\varepsilon_{Dint} + 1}{\varepsilon_{Dext} + 1} \quad (3.24)$$

The measured dimensional changes of disks and rings provided empirical relationships for α and K_{anis} . As shown in figure 3.4, the ratio between dimensional

changes in the compaction plane is independent on the geometry and the material investigated. Therefore, the experimental data were fitted by a linear regression providing a slope coefficient equal to $1 + 0.25 * 10^{-3}$ and an intercept value equal to zero.

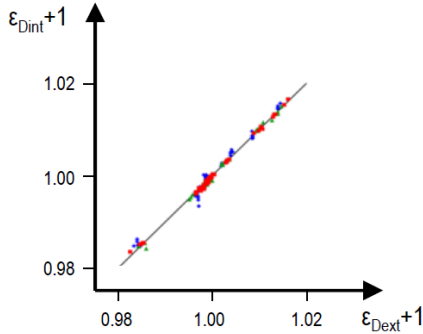


Figure 3.4. Dimensional variation of internal and external diameter for the three geometries investigated on [141].

K_{anis} was calculated by equation (3.21) on the basis of the experimental dimensional changes of disks and rings. The results were plotted as function of the isotropic dimensional change in figure 3.5. These experimental evidences confirm that anisotropy depends on sintering shrinkage/swelling. As observed in other works, on increasing shrinkage/swelling, anisotropy tends to decrease. Aiming at enlarging the sampling to be fitted, thus obtaining a more reliable relationship, shrinking and swelling data have been grouped using $|\epsilon_{ISO}|$.

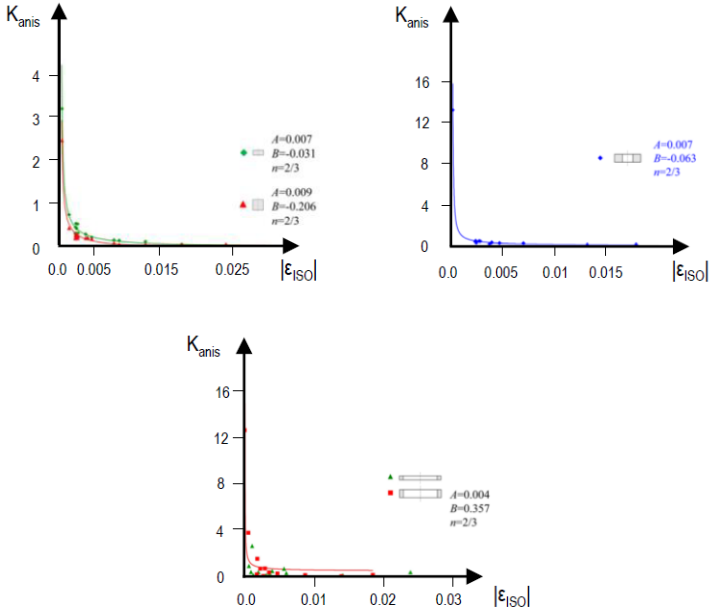


Figure 3.5. Experimental relationships between K_{anis} and isotropic dimensional change determined for disks and rings [141].

The experimental points shown in figure 3.5 were fitted by equation (3.25).

$$K_{anis} = \frac{\varepsilon_{ISO}}{|\varepsilon_{ISO}|} \left[\exp \left(\frac{A}{|\varepsilon_{ISO}|^{2/3}} + B \right) - 1 \right] \quad (3.25)$$

Where A , B are the fitting coefficients, whose values are reported in table 3.1 for different geometries.

Combining equations (3.23) and (3.24) the relationship (3.26) was derived:

$$K_{anis} = \frac{(\varepsilon_{Dext} + 1)\gamma - (\varepsilon_{ISO} + 1)}{\varepsilon_{ISO}} \quad (3.26)$$

Where γ is equal to:

$$\gamma = \sqrt{\frac{1 - \alpha^2 R^2}{1 - R^2}} \quad (3.27)$$

Geometry	A	B
Low disk	0.007	-0.031
High disk	0.009	-0.206
Thin ring	0.007	-0.063
Thick ring	0.004	0.357

Table 3.1. Fitting coefficients derived from the experimental measurement on disks and rings [141].

The dimensional change of any ring-shaped geometry can thus be predicted by a system of equations (3.22, 3.25, 3.27÷3.30). The above procedure is limited to the cases of large change in volume ($|\varepsilon_{ISO}| > 1\%$), alternative relationships are proposed for small change in volume ($|\varepsilon_{ISO}|$ close to 0%).

$$\varepsilon_{Dext} = \frac{\varepsilon_{ISO} * K_{anis} + (\varepsilon_{ISO} + 1)}{\gamma} - 1 \quad (3.28)$$

$$\varepsilon_{Dint} = \alpha(\varepsilon_{Dext} + 1) - 1 \quad (3.29)$$

$$\varepsilon_H = \frac{(\varepsilon_{ISO} + 1)^3}{\frac{(\varepsilon_{Dext} + 1)^2 - R^2 (\varepsilon_{Dint} + 1)^2}{1 - R^2}} - 1 \quad (3.30)$$

Providing that the green dimensions are known, sintered dimensions can be easily predicted solving the above system of the equations (3.22, 3.25, 3.27÷3.30). Nevertheless, designing a new ring-shaped product, the sintered dimensions are the input, whereas the green dimensions are the output of the design procedure. In this case, a recursive approach can be employed as illustrated in the flow chart in figure 3.6. The recursive procedure starts assuming that the ratio between internal and external sintered diameters provides the first tentative value of R . Then the dimensional changes can be calculated, as well as the first estimation of the green diameters. Consequently, R is calculated using the internal and external diameters of the green (as by its definition) and compared with the value of R previously hypothesized in the design procedure. If the discrepancy between the trial and output R is below a given tolerance limit, the green dimensions are determined. On the contrary, the green dimensions are newly calculated updating R value until the procedure converges.

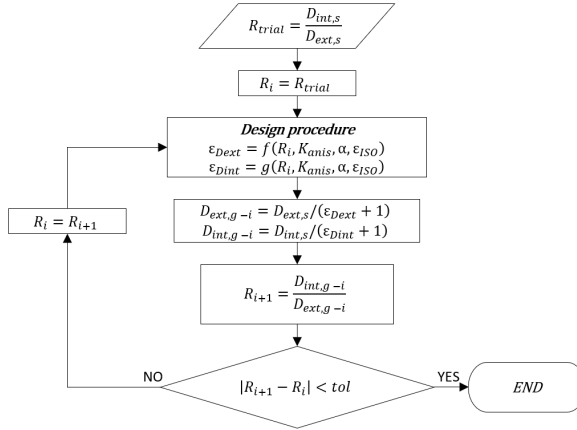


Figure 3.6. Flow chart of the iterative procedure aimed at deriving the green dimension of a ring from the sintered dimensions.

3.3.2 Design procedure for small change in volume

The dimensional change of pure iron disks and ring-shaped samples (ASC100.29 powder) was studied in [152]. This material shows a very small change in volume, that is an isotropic dimensional change close to zero. Alternative empirical relationships for α and K_{anis} were consequently derived.

In this study, the alternative relationship for the anisotropic dimensional change in the compaction plane is given by equation (3.31).

$$\alpha = \frac{\varepsilon_{Dint}}{\varepsilon_{Dext}} \quad (3.31)$$

Measuring the dimensional changes of ASC100.29 disks and rings, the trend of α as a function of the geometry has been derived, showing a linear dependency. This relationship is expressed by equation (3.32).

$$\alpha = mR + q \quad (3.32)$$

Where R is the ratio between the internal and the external diameters defined by equation (3.22) and the coefficients m and q depend on the geometry of the rings. The fitting values are reported in table 3.2 and in figure 3.7A.

Ring height	m	q
5, 10	-0.977	1.923
20	-0.304	1.307

Table 3.2. m and q parameters as function of the ring geometry for the small change in volume [152].

Combining equations (3.23) and (3.31), equation (3.33) is obtained.

$$K_{anis} = \frac{\sqrt{\gamma^2 \varepsilon_{Dext}^2 + \delta \varepsilon_{Dext} + 1} - (\varepsilon_{ISO} + 1)}{\varepsilon_{ISO}} \quad (3.33)$$

Where γ parameter is given by equation (3.27), whereas δ is expressed by equation (3.34):

$$\delta = 2 \frac{1 - \alpha R^2}{1 - R^2} \quad (3.34)$$

Equation (3.21) was used to determine the experimental value of the anisotropy parameter K_{anis} . Due to the extremely small change in volume, equation (3.25) previously derived did not accurately fit the data, so that an alternative empirical relationship was proposed to relate the experimental results of K_{anis} and ε_{ISO} . The new relationship is reported by equation (3.35) and plotted in figure 3.7B.

$$K_{anis} = \frac{C}{\varepsilon_{ISO}} + D \quad (3.35)$$

Where C , and D are the fitting coefficients of equation (3.35). C depends on the geometry as expressed by the polynomial equation (3.36), whereas D has not a clear trend with respect to the ring geometry. Fitting values are reported in tables 3.4÷3.6.

$$C = C_0 + C_1 R + C_2 R^2 \quad (3.36)$$

The coefficients C_0 , C_1 , C_2 are reported in table 3.3.

C_0	C_1	C_2
$7 \cdot 10^{-4}$	$-7 \cdot 10^{-4}$	$7 \cdot 10^{-4}$

Table 3.3. Fitting coefficients of equation (3.36) [152].

R	0	0	0	0.2	0.2	0.2
height	5	10	20	5	10	20
D	0.04	0.09	0	0.08	0.02	-0.005

Table 3.4. D coefficient as function of the ratio between the internal and external diameter (R) and the height of the rings analyzed [152].

R	0.4	0.4	0.4	0.6	0.6	0.6
height	5	10	20	5	10	20
D	0.01	0.045	-0.065	0.005	0.04	-0.05

Table 3.5. D coefficient as function of the ratio between the internal and external diameter (R) and the height of the rings analyzed [152].

R	0.9	0.9	0.9
height	5	10	20
D	0.005	0.005	-0.01

Table 3.6. D coefficient as function of the ratio between the internal and external diameter (R) and the height of the rings analyzed [152].

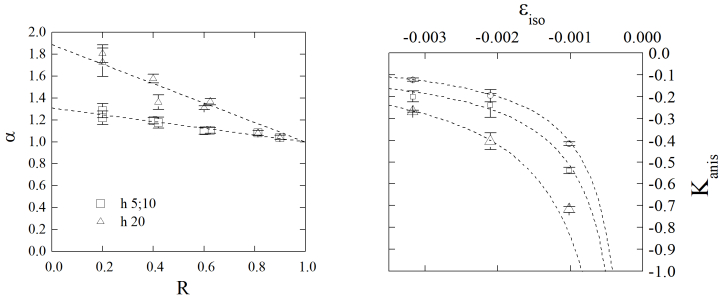


Figure 3.7. On the left the dependence of α on diameter ratio. On the right the experimental dependence between K_{anis} and isotropic dimensional change [152].

Again, using the anisotropy parameters K_{anis} and α derived by the empirical relationships in the case of small change in volume ($|\epsilon_{ISO}|$ close to 0%), the dimensional change of a ring-shaped geometry can be predicted by system of equations (3.22, 3.27, 3.34 ÷ 3.39)¹⁵.

$$\epsilon_{Dext} = \frac{-\delta + \sqrt{\delta^2 - 4\gamma^2\{1 - [\epsilon_{ISO}(K_{anis} + 1) + 1]^2\}}}{2\gamma^2} \quad (3.37)$$

$$\epsilon_{Dint} = \alpha\epsilon_{Dext} \quad (3.38)$$

$$\epsilon_H = \frac{(\epsilon_{ISO} + 1)^3}{(\epsilon_{Dext} + 1)^2 - R^2(\epsilon_{Dint} + 1)^2} - 1 \quad (3.39)$$

As previously mentioned, the solution of the system of equations (3.22, 3.27, 3.34 ÷ 3.39) provides the sintered dimensions if the green dimensions are known. On opposite case, the iterative procedure reported on figure 3.6 can be used in order to calculate the green dimensions.

¹⁵In order to explicit ϵ_{Dext} from relation (3.33), two possible solutions are determined by the solution of a second order equation. However, one of the solutions has no physical meaning, and the valid one is reported in equation (3.37).

3.3.3 Design procedure applied to multilevel parts

In sections 3.3.1 and 3.3.2 the design procedure predicting the dimensional change on sintering of a ring-shaped geometry has been described. However, most of the P&S parts are not simple disks or rings. In order to adapt the design procedure to a more complex geometry, a second fundamental assumption is introduced, while confirming the first hypothesis of negligible shape distortion on sintering. The second assumption is that a complex axi-symmetric geometry can be modelled as an assembly of simple rings. Therefore, any axi-symmetric geometry can be broken down under ring-shaped elements, according to two possible approaches, defined as column-based approach and maximum section-based approach.

The column-based approach splits the multilevel geometry in coaxial rings, whose height correspond to the powder columns during compaction. In the maximum section-based approach, the ring-shaped element corresponding to the larger volume is firstly identified. Then the rings having progressively small sections are identified, until the whole volume of the multilevel parts is broken down under ring-shaped elements. The two breakdown strategies are shown in figures 3.8 and 3.9.

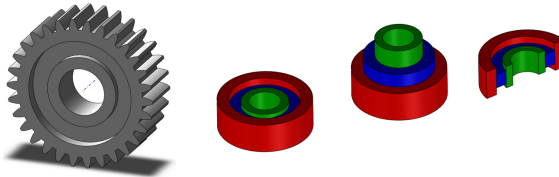


Figure 3.8. Example of column-based approach for a multilevel part.

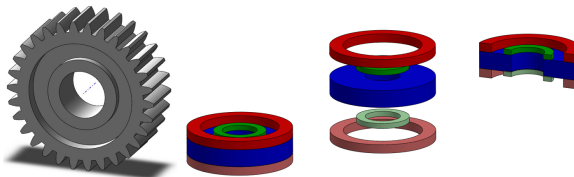


Figure 3.9. Example of maximum section-based approach for a multilevel part.

The design procedure is used in order to calculate the dimensional changes of each rings. When the predicted dimensions are derived, it is necessary to restore the geometry of the multilevel part by re-assembling the rings. Some problems can occur when there are different predictions, coming from the analysis of the single rings, for the common diameters. In this case, the geometrical congruence is established by an equivalent predicted diameter, whose dimension is determined by the weighted average expressed by equation (3.40).

$$D_i = \frac{\sum_{j=1}^N (D_j V_j)}{\sum_{j=1}^N (V_j)} \quad (3.40)$$

Considering the example in figure 3.9, the external diameter of the multilevel part corresponds to the external diameter of three ring-shaped elements: the blue, the red and the magenta ones. Consequently, the design procedure might provide three different predictions for the same diameter. The equivalent dimension is calculated by equation (3.40), where n is equal to 3, D_j are the predicted ring diameters and V_j are the volumes of the three rings.

In conclusion, the flow chart in figure 3.10 summarizes the main steps of the model predicting the dimensional change on sintering of a multilevel axi-symmetric component.

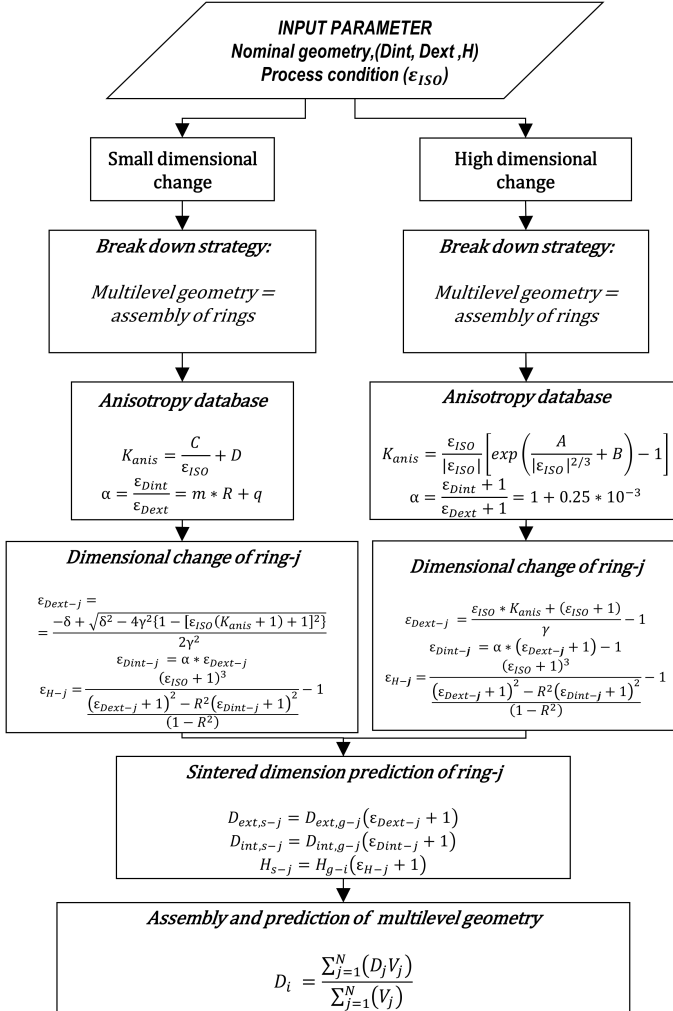


Figure 3.10. Flow chart of the design process of a multi-level axi-symmetric geometry.

3.4 Experimental procedure

DfS project was developed in order to evaluate the accuracy of the design procedure in the prediction of the dimensional change on sintering of real structural parts. The test-bed was designed as following described.

The components were measured before and after sintering. The sintered dimensions were estimated by the design procedure, using the dimensions of the green parts as input parameters. Then the predicted dimensions were compared with the measured dimensions of the sintered parts in order to check the accuracy of the model.

As mentioned above, five companies were involved in the DfS project. Each company provided one complex axi-symmetric part. Table 3.7 summarizes the part name, the material and green density of the components provided by each company. In figure 3.11 the shape and the different size of the parts can be appreciated.

Part name	Powder mix	Lubricant	Green density [g/cm ³]
1	2.00% Cu, 1.47% Mo, 0.6%C/UF4	0.8%	6.93-7.03
2	Ancorsteel: DWP200-12%D10Cu, 0.65%C	0.6%	7.0
3	Astaloy CrA, 0.6%C	/	7.15
4	AISI 316L	/	6.45
5	AISI 430L	/	6.30-6.45

Table 3.7. Name, material, and green density of the five axi-symmetric parts provided by the company partners.

Figures 3.12 ÷ 3.16 show the schematic drawings of the parts, along with the main dimensions. All the dimensions were measured, but only minimum and maximum ones are reported, for the sake of clarity. The drawings do not report details, such as grooves, threaded holes, and slots because the analysis of the dimensional change of these elements is not crucial in this study. For the same reason, the tooth profiles were not measured.

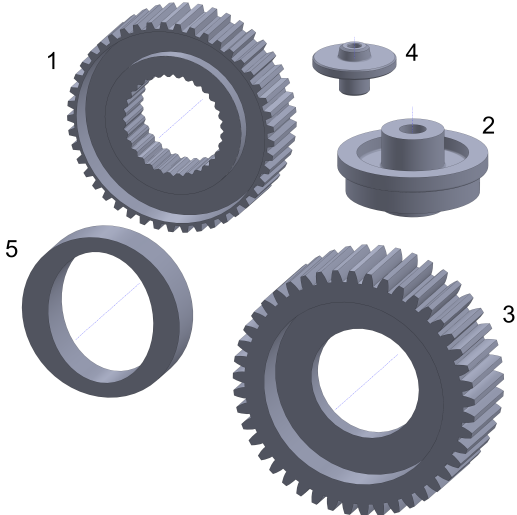


Figure 3.11. The parts studied.

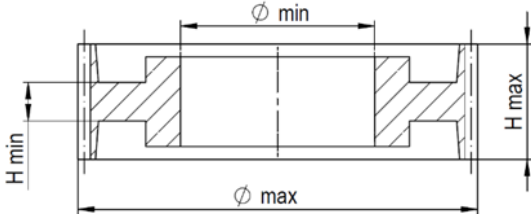


Figure 3.12. Schematic drawing of the part 1.

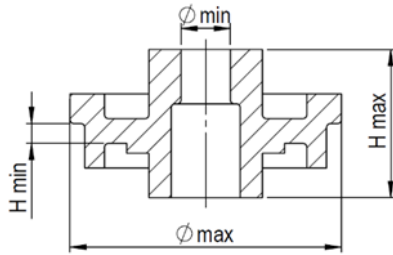


Figure 3.13. Schematic drawing of part 2.

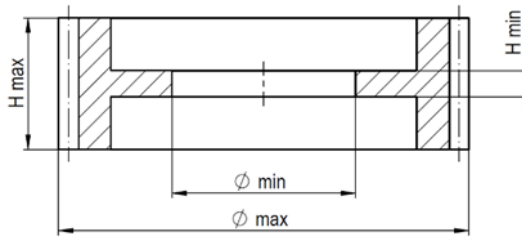


Figure 3.14. Schematic drawing of part 3.

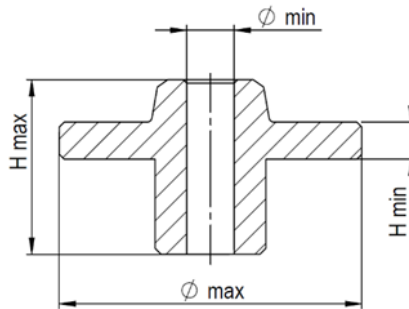


Figure 3.15. Schematic drawing of part 4.

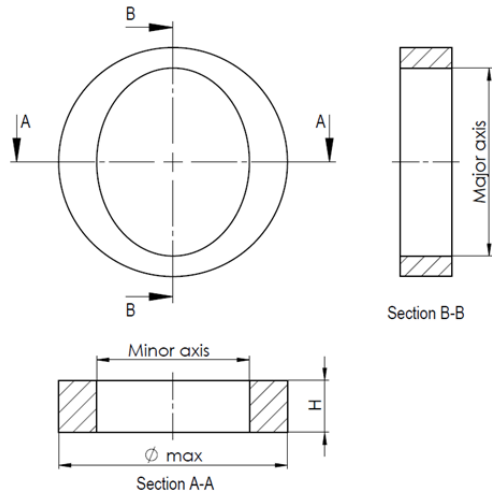


Figure 3.16. Schematic drawing of part 5.

Due to confidential agreement, the nominal dimensions are not disclosed. In order to comprehend the range of dimensions, table 3.8 describes the approximate smallest and largest diameters and heights for each geometry.

Part name	D_{min} [mm]	D_{max} [mm]	H_{min} [mm]	H_{max} [mm]
1	37	81	7	23
2	10	55	5	30
3	42	94	6	30
4	5	30	4	18
5	40	60	/	18

Table 3.8. Approximate minimum and maximum dimensions of each geometry.

Each company provided around twenty green parts, which were pressed according to the conventional compaction strategy of the company producer. Due to the low number of parts investigated, each sample was marked with an ID number on the upper plane¹⁶ of the part, in a position that does not influence the measurement. This action allowed to track the samples before and after the sintering process. In addition, the dimensional change was analysed sample by sample.

The green components were carefully packed and sent to the University of Trento, where the dimensions were measured by means of a coordinate measuring machine (CMM). The CMM is a DEA Global image 07-07-07 which is equipped by a continuous scanning head SP600 Renishaw with an accuracy of 3.4/120 $\mu\text{m/s}$ according to ISO 10360-4 [97]. The length of the stylus and the dimension of the probe were properly selected considering the different dimensions and geometries, as summarized in table 3.9.

Part name	Extension [mm]	Approaching length/diameter [mm]	Tip sphere [mm]
1	25	30-1.5	2
2	25	30-1.5	2
3	30	30-1.5	2
4	30	30-1.5	2
5	/	100-4.5	8

Table 3.9. Summary of the tip equipment used for measurements.

A specific clamping system was designed for each geometry in order to guarantee an optimal access to all the sample surfaces. Internal holes can be scanned completely, whereas some diameters and planes can be scanned in an angular range close to 300°. Examples are shown in figure 3.17.

¹⁶In this study the upper plane is defined as the plane of the part in contact with the upper punches during the compaction process, whereas the bottom plane refers to the plane in contact with the lower punches.

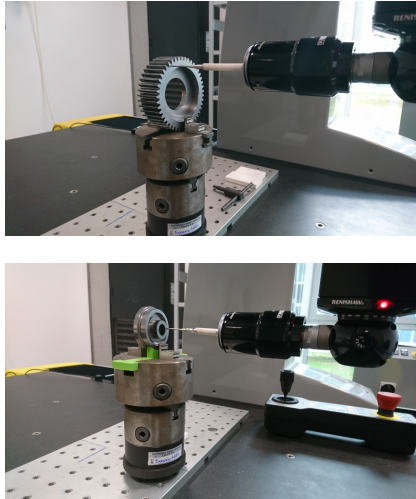


Figure 3.17. Examples of clamping configuration designed for the components.

For each geometry, a measuring routine was programmed on PC-Dmis 2016 software suite. The routine guarantees a measurement procedure common for the samples in the green and sintered state.

Each routine firstly identified the part reference system in order to align the part to the machine reference systems. A common alignment procedure was defined for the different geometries. Since all the geometries are axi-symmetric, the reference alignment required at least the definition of a plane and an axis. The bottom plane having the major surface area was used for the plane alignment. The axis alignment was defined by the axis of the internal hole or by the axis of the external cylindrical surface.

Afterwards, planes were scanned in order to reconstruct the planar surfaces. The points acquired during the continuous scans were firstly filtered out the values outside the 3σ interval of the normal distribution and the remaining ones were fitted by least squares method. Then the heights were calculated by the distance between the planes. In a similar way, diameters were scanned at one or more height levels. When the same diameter was scanned at different levels, all the points acquired were fitted by least squares method in order to reconstruct a cylindrical surface, from which the diameter was derived.

It is important to mention that a huge number of points were acquired on each

part. This improves the reliability of the measurement and, in addition, enables the reconstruction of the shape, which is fundamental to verify any possible distortion with relation to the nominal shape.

When all components were measured in the green state, 10 samples for each geometry were carefully packaged and sent back to the producer to be sintered. The sintering conditions are reported in table 3.10.

Part name	Temperature [°C]	Time [min]	Atmosphere	Furnace
1	1120	30	90 N ₂ -10 H ₂	Belt furnace
2	1120	25	95 N ₂ -5 H ₂	Modular furnace
3	1120	30	90 N ₂ -10 H ₂	Belt furnace
4	High T	/	/	/
5	/	/	/	/

Table 3.10. Known sintering conditions.

In the sintering process, the components were positioned according to a standard procedure, providing that the bottom plane of the part was in contact with the sintering support inside the furnace. This procedure avoided random orientation, which could affect the dimensional change. In fact, in literature the influence of gravity on the shape distortion and on the anisotropy of the dimensional change is reported [153–155].

After the sintering process, sintered parts were shipped back to the University of Trento, where the sintered dimensions were measured using the same routine developed for the green parts. Finally, the actual dimensional changes were determined by equations (3.1÷3.3,3.13÷3.15,3.17).

3.5 Results and discussion

3.5.1 Introduction

In the next sections the results of the test-bed are reported. Actual dimensional changes are firstly calculated and discussed. Afterwards, the column-based and maximum section-based approaches are compared in order to evaluate the more representative break down strategy for axi-symmetric geometries. Ring-shaped elements were identified, and the design procedure was used in order to predict the sintered dimensions starting from the green measurements. The predicted dimensions are compared with the measured dimensions. By this way, the accuracy of the design model is evaluated. The results are discussed and some hypotheses are proposed in order to interpret the lack of accuracy in dimensional prevision. The model has been tested on the four axial-symmetric components, and on a non-cylindrical geometry. In conclusion, a critical analysis summarizing the limits of the design procedure and the anisotropic empirical relationships is proposed, aiming at identifying ways for improvement of the design method.

3.5.2 Measurement results

Figures 3.18 to 3.22 show the dimensional change of diameters and heights for each geometry, along with the isotropic dimensional change. It is reminded that only maximum and minimum dimensions are shown in the schematic drawings (figures 3.12 to 3.16) but all the dimensions (diameters and heights) have been measured in each part and the related dimensional changes are following reported.

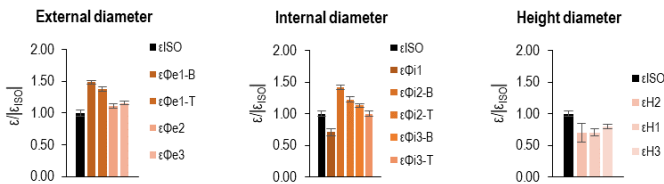


Figure 3.18. Dimensional change of external diameters (on the left), internal diameters (center) and heights (on the right) of part 1.

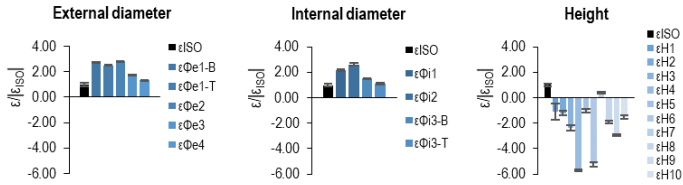


Figure 3.19. Dimensional change of external diameters (on the left), internal diameters (center) and heights (on the right) of part 2.

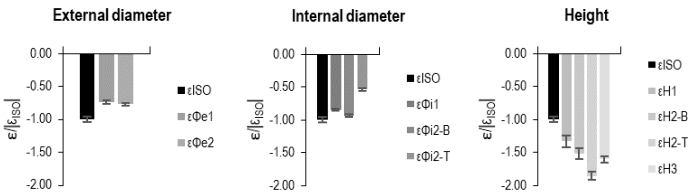


Figure 3.20. Dimensional change of external diameters (on the left), internal diameters (center) and heights (on the right) of part 3.

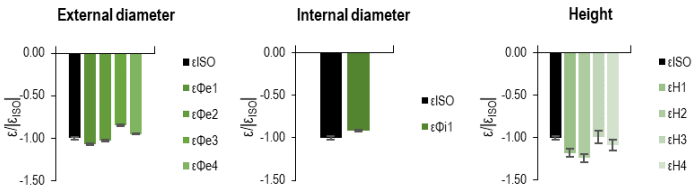


Figure 3.21. Dimensional change of external diameters (on the left), internal diameters (center) and heights (on the right) of part 4.

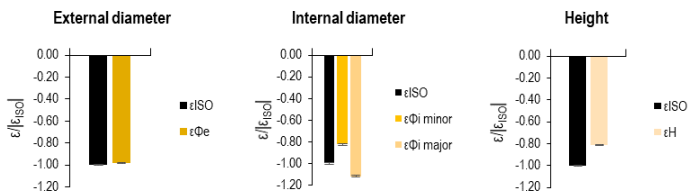


Figure 3.22. Dimensional change of external diameters (on the left), internal diameters (center) and heights (on the right) of part 5.

The dimensional changes of diameters and heights were ordered on each graph from the minimum to the maximum size. Results are normalized to the absolute value of the isotropic dimensional change because the actual dimensional change cannot be revealed due to confidential agreement. For this reason, the isotropic dimensional change is reported on the figures as reference parameter. The normalization does not affect the sign of the dimensional change (the shrinkage and swelling behavior remaining unchanged), neither the relative entity, being each dimensional variation just scaled by a multiplier factor. Also the scatters, which correspond to 1σ interval of the dispersion, were normalized by the same multiplier factor.

The proposed representation clearly shows the anisotropic dimensional change on sintering. The analysis of the figures confirms that anisotropic dimensional change occurred both in longitudinal (height) and in transversal (diameters) directions. Analyzing the different geometries, a higher shrinkage of heights than diameters occurred in components 3 and 4, whereas the outcome is the contrary on part 5. The higher shrinkage of heights confirms the expected result in solid-state sintering. The inverse trend observed in component 5 is not completely understood.

The increase in volume in geometries 1 and 2 is due to the liquid-phase sintering mechanisms. In part 1, a higher swelling of diameters than heights occurred, as generally expected in liquid phase sintering. On the other hand, heights of geometry 2 exhibited both shrinkage and swelling.

An additional analysis of the figures reveals the difference between the dimensional change of the internal and the external diameters. This is particularly evident on geometry 5, where the major and minor axis of the oval hole behaves in a completely different way with respect to the external diameter. Since the explanation of this case is postponed to section 3.5.6., it is now discussed the anisotropy in the compaction plane for the four axi-symmetric geometries.

From a general point of view, the dimensional variation of heights strongly differs from the dimensional variation of diameters, and the dimensional change in the compaction plane is also anisotropic. In the same geometry, the dimensional variation of diameters can be higher or lower than the isotropic dimensional change. An explanation concerning the origin of anisotropy in the compaction plane is proposed on the basis of the literature review.

During compaction of simple ring-shaped geometry, the radial and tangential stresses in the compaction plane are theoretically equal. Consequently, the dimensional variation of the diameters should be ideally isotropic. However, shear stresses may arise during compaction of complicated multilevel parts, so that

inhomogeneous distribution of powder occur. The alignment of powder particles and elongated pores along the shear stress direction could cause the anisotropic dimensional change between the external and internal diameters.

Further analysis highlights that the absolute dimensional variation of diameters decreases on increasing the nominal size, whereas no general trend can be highlighted for heights.

Unexpected behavior was observed in the geometries having two diameters of the same nominal size symmetrically positioned with respect to the neutral zone, as schematically displayed in figure 3.23.

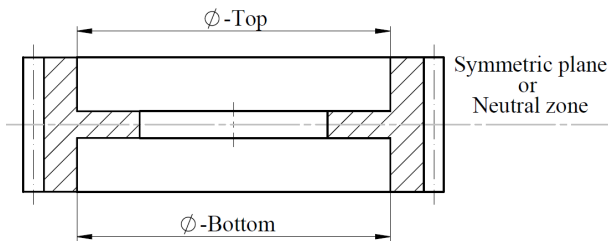


Figure 3.23. Example of diameters having the same nominal size positioned symmetrically to the neutral compaction zone.

The diameters below the neutral axis (B diameter) show higher dimensional change with respect to the diameters placed above the neutral axis (T diameters). The difference is almost negligible in all the cases, except for component 3. These results are under investigation and two explanations may be proposed. Double action compaction might not be properly set up, and the density gradient might be different in the two sides opposite to the neutral axis. Consequently, a different dimensional change might occur on sintering, due to the different density. Concerning sintering, the part might be not homogeneously heated. The bottom surface is heated up through the thermal conduction with the furnace support, while the upper surface is heated up by thermal radiation and convective mechanisms. Therefore, inhomogeneous heating of the surface might produce the slightly different dimensional changes in the lower and upper side.

A final consideration regards the distortion of the shape. The geometrical characteristics of flatness, planarity, circularity and cylindricity were measured for the geometries investigated, resulting lower or comparable with conventional P&S

product specification [74]. Therefore, the hypothesized negligible volume distortion was confirmed. This result validates the first assumption of the design model, which requires negligible volume distortion on sintering.

3.5.3 Isotropic dimensional change

The test-bed was developed in order to compare the measured and predicted dimensions at the sintered state. Predicting the dimensional variation, the design procedure needs the green dimensions and the isotropic dimensional change as input parameters. The isotropic dimensional change is the keystone of the design procedure. Indeed, the anisotropy coefficient K_{anis} is calculated by empirical relationships as a function of ε_{ISO} . The design procedure is based on the difference between anisotropic and isotropic dimensional change to assess the actual dimensional variation. Hence, an accurate determination of the ε_{ISO} is fundamental for a reliable application of the design procedure.

In this project, the isotropic dimensional change was calculated from equation (3.17). In order to derive the change in volume, the axi-symmetric geometries were broken down in ring-shaped elements. The volume of rings can be easily calculated by the measurements of the diameters and heights. Subsequently the volume of the complex geometry was calculated by the assembly of ring-shaped volumes. As previously established, the profile of the teeth was not measured and the related ring-shaped part was defined by the top of the teeth as external diameter.

Both the column and maximum section-based approaches can be adopted to break down the complex geometry on ring-shaped elements, and the change in volume obtained by the two methods was calculated. The comparison showed an equivalent result. Therefore, it was concluded that the break down method does not affect the calculation of the isotropic dimensional change.

Concerning sample 5, the volume was computed by the difference of the volume of the cylinder defined by the external diameter and the volume of the oval hole, assumed as elliptical.

As shown in figures 3.18÷3.22, isotropic dimensional change is positive for parts 1 and 2 (swelling), and negative for parts 3, 4, and 5 (shrinkage). It is possible to reveal that the ε_{ISO} is close to zero for parts 1, 2 and 3, while parts 4 and 5 exhibited large change in volume. Therefore, the design procedure and the empirical relationships described in section 3.3.2 were used for parts 1, 2, and 3, while the design procedure

and the anisotropic database reported in section 3.3.1. were used for parts 4 and 5.

In this work the isotropic dimensional change was computed by the change in volume. However, on the development of a new P&S product the change in volume is unknown in principle, as well as the dimensional variations. Therefore, alternative approaches must be used in order to evaluate the isotropic dimensional change. The simplest one correlates the change in volume to the change in density, as by equation (3.41), neglecting the mass loss occurring on dewaxing¹⁷. When a new product is developed, the sintered density could be derived by customer specification, whereas the green density might be estimated by the knowledge of starting density and powder compressibility in the compaction operation.

$$\varepsilon_{ISO} = \frac{V_s - V_g}{V_g} = \frac{\rho_g - \rho_s}{\rho_s} \quad (3.41)$$

However, the isotropic dimensional change determined by volume and by density measurements may differ. Generally, the accuracy of density measurement is one order of magnitude less accurate than mass and dimensional measurements. In addition, the density of PM product is hard to be precisely evaluated, due to the open and close porosity. In this study, no wide experimental measurement of density was performed, so that this approach was not suitable. Another approach would estimate ε_{ISO} by dilatometric tests, but this method is also complicated, and needs for a deep knowledge of the sintering operation procedure, so that it was also excluded in this project. In conclusion, the change in volume was calculated by the dimensional measurements because this is the more reliable method.

3.5.4 Geometry Break Down

In the previous section, it was mentioned that the two break-down strategies estimated the same change in volume, and consequently the same isotropic dimensional change. However, the two methods do not provide the same prediction of anisotropic dimensional changes. A numerical example demonstrates this assertion. In figure 3.24, the ring-shaped elements identified by the two break-down approaches are reported.

The design procedure was applied to each of these rings and the resulting sintered geometry was calculated by ring assembly. The inaccuracy of the design procedure

¹⁷The result of equation (3.41) is more reliable if the mass loss will be assessed by the lubricant weight fraction.

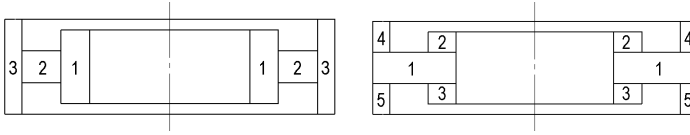


Figure 3.24. Example of the ring-shaped elements identified by the column (left) and maximum section (right) break-down approaches.

was then evaluated by equation (3.42).

$$\begin{aligned}\varepsilon_{inaccuracy} &= \frac{\phi_{Predicted} - \phi_{Measured}}{\phi_{Measured}}; \\ &= \frac{H_{Predicted} - H_{Measured}}{H_{Measured}}\end{aligned}\quad (3.42)$$

Where:

- $\phi_{Predicted}$; $H_{Predicted}$ corresponds to the sintered dimension predicted by the design procedure,
- $\phi_{Measured}$; $H_{Measured}$ corresponds to the measured dimension at the sintered state.

In figure 3.25 the results of equation (3.42) related to the two break-down approaches are shown. The example concerns part 1.

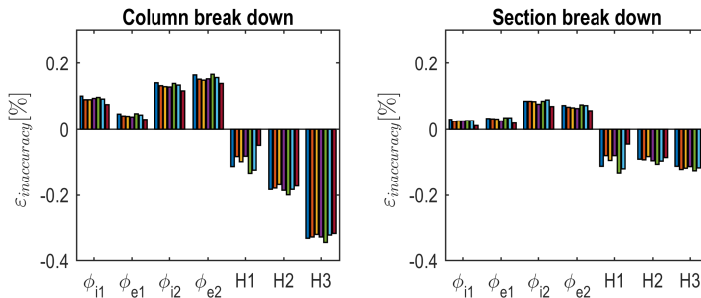


Figure 3.25. Discrepancy between the predicted and measured diameters and heights. On the left results obtained by the column-based break-down approach, on the right results obtained by the maximum section-based approach.

Figure 3.25 clearly demonstrates that the dimensional change of diameters and heights is better predicted by maximum section-based approach. The same analysis was repeated for the other geometries and comparable results were obtained. Therefore, it is concluded that the maximum section-based approach is the most effective break-down strategy in the estimation of the dimensional change.

A possible explanation is suggested. Defining the geometry of the rings in terms of the parameter $H/2T$, the rings identified by maximum section approach are more similar to the ring samples investigated on the development of the material database. Therefore, the empirical relationships of the anisotropic database may provide a better estimation of the dimensional change.

Consequently, the results deriving from the maximum section-based approach will be presented.

In figure 3.26 the rings recognized by the maximum section-based approach are shown for the axi-symmetric geometries.

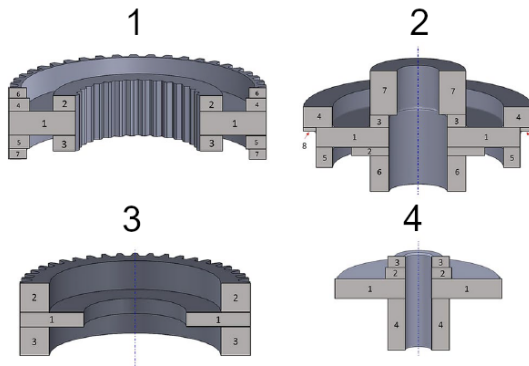


Figure 3.26. Rings derived from the maximum section-based approach for the four geometries having axi-symmetric geometry.

Since the geometry 5 has not a cylindrical shape, this shape will be discussed separately. It is important to mention that parts 1 and 4 present a slightly conical surface, as showed in figures 3.12 and 3.15. In order to describe this geometry, two rings having different section approximate the conical shape. Concerning the gear teeth, the profile is not object of the current analysis, and, as previously mentioned, the design procedure estimates the dimensional change of the diameters defined by the top of the gear teeth.

3.5.5 Prediction Results

Figures 3.27 ÷ 3.31 show the prediction inaccuracy, as by equation (3.42), for the external, internal diameters and heights, distinguishing the results obtained for each batch investigated. The geometries with small change in volume are firstly discussed.

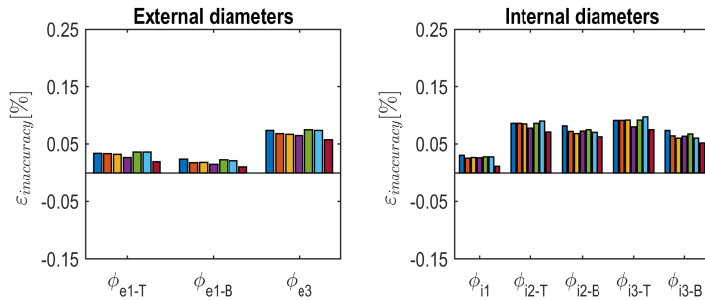


Figure 3.27. Inaccuracy of the prediction of: external diameters (on the left) and internal diameters (on the right) - part 1.

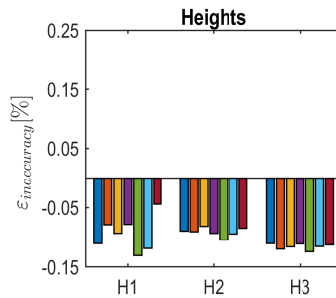


Figure 3.28. Inaccuracy of heights prediction - part 1.

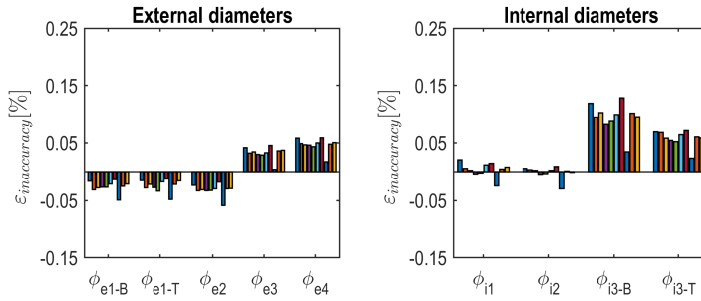


Figure 3.29. Inaccuracy of prediction of: external diameters (on the left) and internal diameters (on the right) - part 2.

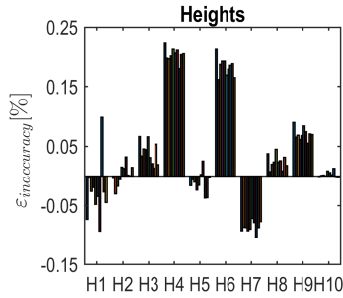


Figure 3.30. Inaccuracy of heights prediction - part 2.

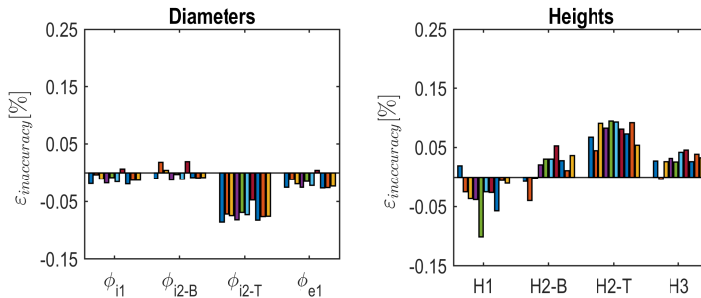


Figure 3.31. Inaccuracy of the prediction of: external diameters and internal diameters (on the left) and heights (on the right) - part 3.

The prediction inaccuracy for diameters and heights is lower than 0.15% in the geometries showing a small change in volume (parts 1, 2, 3), with the only exception of two dimensions. In these geometries, diameters are more accurately predicted than heights, and, in addition, the external diameters display a slightly lower inaccuracy than the internal diameters. In order to explain the discrepancy between the predicted and measured dimensions, each geometry is discussed separately.

In part 1, the prevision inaccuracy is lower than 0.10% for diameters and 0.15% for heights. The inaccuracy has been ascribed to the anisotropic relationships used in the design procedure, deriving from samples differently shrinking. As further evidence, the bigger inaccuracy is observed in height estimation, because the design procedure predicts higher dimensional change for heights than for diameters, whereas, the opposite behavior occurred in the real situation. Another point concerns the prediction of diameters having the same size but placed below and above the symmetric plane. As previously mentioned, commenting figures 3.18 ÷ 3.20, the actual, slightly different dimensional change of the diameters placed above and below the neutral zone might be due to the different heating in upper and lower surface. Different heating means different ε_{ISO} , and since the average ε_{ISO} was used, the design procedure cannot predict the different dimensional changes of dimensions with the same nominal size.

The inaccuracy in the prevision of diameters of part 2 is lower than 0.05%, around 0.10% for just two internal diameters (ϕ_{i3-B} , ϕ_{i3-T}). This result is likely related to the anisotropic empirical relationships. In fact, the design procedure hypothesizes higher dimensional change of internal diameter than external diameter, while in this case it is more or less constant and equal to 0.05%.

The bigger inaccuracy was observed in height estimation. Analyzing the actual dimensional change of heights, both shrinkage and swelling occurred, while the design procedure assumed only swelling. Therefore, the prediction inaccuracy mainly depends on the limit of the material and geometry database, which is currently not able to describe both shrinkage and swelling simultaneously occurring.

Excellent results were observed in part 3, prediction inaccuracy being $\pm 0.05\%$ with the exception of the dimensions below the symmetric plane (ϕ_{i2-B} , H_{2-B}). As a possible explanation, it must be considered that components were produced in a research laboratory, compaction was not as carefully controlled as in industrial production process. Therefore, the density gradient resulting from the double action compaction process might be different than expected with respect to the theoretical neutral zone. The inhomogeneity of the green density gradient might cause a different

densification on sintering, thus determining the observed prediction inaccuracy for dimensions ϕ_{i2-B} , H_{2-B} .

The prediction inaccuracy of part 4 is reported in figure 3.32. The error on diameters and height prediction is below 0.30% and 0.75%, respectively.

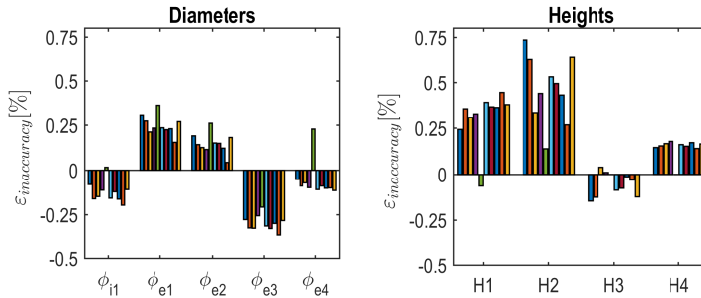


Figure 3.32. Inaccuracy of the prediction of: external diameters and internal diameters (on the left) and heights (on the right) - part 4.

In this case, too, the inaccuracy can be attributed to the lacking database. In the case of high change in volume, the anisotropic empirical relationships were derived from data coming from swelling samples, while part 4 showed large shrinkage. Again, the same interpretation proposed for part 1 could explain the poor accuracy in height prediction.

3.5.6 Non-cylindrical geometry: oval shape

In part 5 two planes of symmetry can be identified, corresponding to the major and minor axes of the oval hole. Therefore, the design procedure will be modified according to this complex profile.

As first trial, dimensional changes were estimated in three possible ring-shaped geometries, having the same external diameter and height of part 5, and different internal diameter, equal to the minor, major, and average axis, respectively. The design procedure was used for these ring-shaped geometries. The difference between the predicted and measured dimensions is shown in figure 3.33 which reports the results for the three conditions.

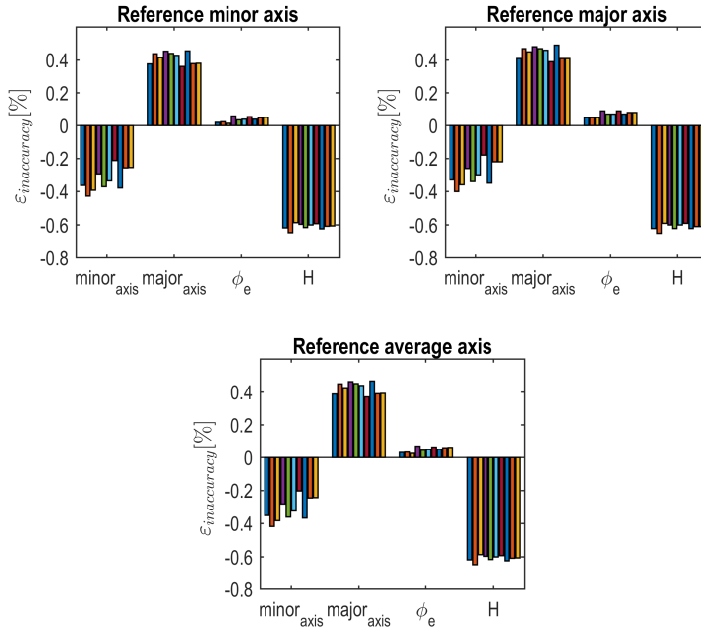


Figure 3.33. Inaccuracy between the predicted and measured dimensions based on the three different ring-shaped representation of part 5.

The three ring-shaped geometries provided more or less the same result. The external diameter is correctly assessed, while the height and the internal axes are poorly estimated in any case.

The inaccuracy of height estimation still depends on K_{anis} coefficient. As previously reminded, in case of high isotropic dimensional change, the design procedure uses an empirical relation for K_{anis} determined on the basis of swelling sampling (Fe, 2%Cu, Fe-4%Cu), while in this case study shrinkage occurs. Again, this database is not suitable for the current investigation, and, in fact, the design procedure estimated a higher dimensional change for height than for diameters, contrarily to the actual results.

As seen in figure 3.33, the dimensional changes of the axes were inaccurately predicted in all of the three conditions. The reason for such inaccuracy depends on the model, which supposes an isotropic behavior in the compaction plane, whereas

the actual dimensional change is strongly anisotropic. As underlined in figure 3.22, the shrinkage of the major axis is higher than that of the minor axis.

It can be concluded that the procedure failed on evaluating the dimensional change of the height and the internal profile due to the inadequacy of the empirical relationships of anisotropy. Since these relationships were derived for different materials and process conditions, they are not valid for the actual case of study.

Despite this poor result, the possibility to apply the design procedure to non-cylindrical geometries has been evaluated. In order to evaluate the dimensional change of the internal profile, the following method is proposed.

The internal profile was measured by continuous scans at the green and sintered state at different height levels. An example of the experimentally derived points is shown in figure 3.34.

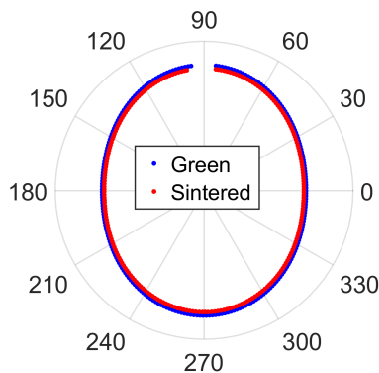


Figure 3.34. Example of the points measured at the green and sintered state along the profile of the internal hole for the same sample.

The coordinates of the experimental points can be translated from cartesian to a polar reference system as shown in following. In this way, the radial coordinate of the experimental points can be assumed equal to the internal radius of a fictitious rings. However, another problem occurred on evaluating the accuracy of the dimensional change. As seen in figure 3.35, the angular coordinate for green and sintered experimental points is not the same. For this reason, the sintered dimension predicted on the basis of a green point cannot be compared with the measured dimension based on the point at the sintered state, because they correspond to different angular

coordinates.

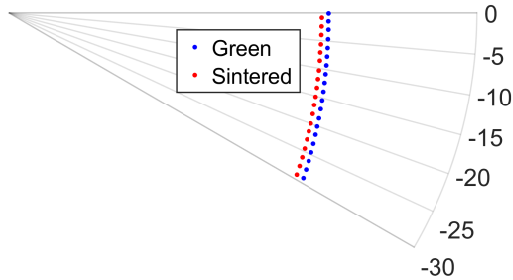


Figure 3.35. Example of different angular position between the experimental points collected during the scan of the internal profile at the green and sintered state .

Since a direct comparison between the measured and predicted points cannot be performed, an alternative approach was developed in order to predict the sintered profile. The experimental points were fitted by Lamé curve, equation (3.43). In this way, the oval profile can be parametrically defined.

$$\left(\frac{x}{a}\right)^n + \left(\frac{y}{b}\right)^n = 1 \quad (3.43)$$

Where:

- x, y are the cartesian coordinate of the measured points,
- a, b are respectively the semi axes of the oval profile,
- n is the exponent which describes the type of ellipse¹⁸

The x, y coordinates of the experimental points were known by the continuous scanning acquisitions. The semi axes of the oval hole were consequently derived. Therefore, the n exponent was the only unknown coefficient, which was derived by the fitting operation for each sample at the green and sintered state. An example of the comparison of the experimental points and the fitting trend is illustrated in figure 3.36.

¹⁸Equation (3.43) is a generalization of the classical ellipse formula. When the $n > 2$ the figure is called hyper-ellipse whereas when $n < 2$ the figure is called hypo-ellipse.

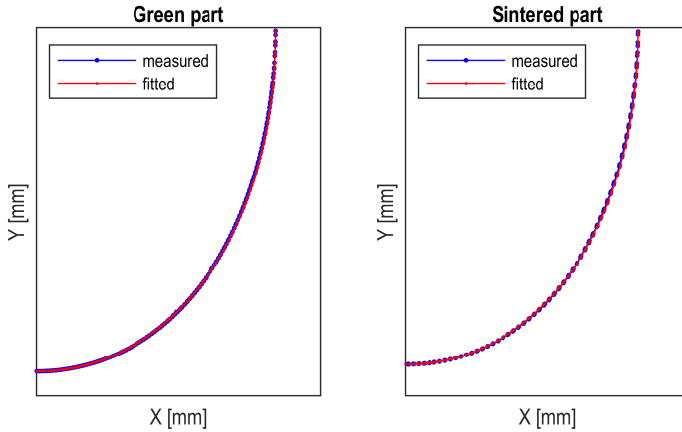


Figure 3.36. Example of the experimental points and the fitting trend derived by equation (3.43) for the green and sintered state.

The fitting curve showed a very good overlap with the experimental points. Therefore, the oval shape can be approximated by a hyper-ellipse, whose exponent n is always slightly higher than 2.

In order to introduce the result of the fitting operation in the design procedure, it is more convenient to express equation (3.43) in polar coordinates (τ, θ) , as represented by equation (3.44).

$$\left(\frac{\tau * \cos \theta}{a}\right)^n + \left(\frac{\tau * \sin \theta}{b}\right)^n = 1 \quad (3.44)$$

In this way the radial coordinates of the internal profile can be derived by the angular position (θ) and the coefficients a, b, n , both at the green and sintered state.

The prediction of the dimensional change of the internal profile is accomplished as follows. At an established angular position, the green radial coordinate is calculated by equation (3.44). Then the radial coordinate is assumed equal to the internal radius of a ring¹⁹. By this way, the design procedure can estimate the predicted sintered dimension. Then at the same angular position the measured sintered radius

¹⁹The external diameter and height are supposed equal to the dimensions of part 5.

is calculated by equation (3.44) using the different fitting coefficients. Repeating the same calculation at different angular positions, the predicted sintered profile can be obtained and compared to the measured one.

An example of the difference between the predicted and sintered internal profile is shown in figure 3.37.

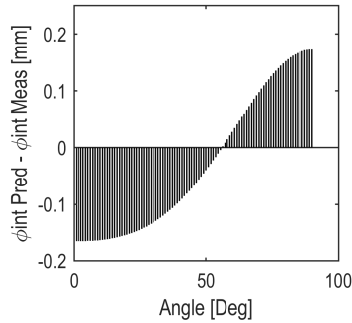


Figure 3.37. Example of the difference between the predicted and the measured internal profile versus the angular coordinate.

By this method, it is demonstrated that the design procedure can be extended to non-cylindrical geometry. On the other hand, the analysis of figure 3.37 shows that the discrepancy between the predicted and measured profile has a minimum, and the error increases moving towards the minor and major axis as already observed in figure 3.33. An interesting point is the position of the minimum error, which occurred around the same angular position for all the samples investigated. At this angular position, the radial coordinate (R_{eq}) satisfies the volume conservation expressed by equation (3.45) between part 5 and a ring having the same external diameter and height of part 5.

$$V_{part5} = H\pi (R_{ext}^2 - R_{eq}^2) \quad (3.45)$$

For all the samples investigated, the difference between the predicted and measured oval profile was plotted as function of the difference between the radial coordinate and the equivalent radius, as displayed in figure 3.38.

The figure confirms the repeatability of the prevision error, and the lowest discrepancy occurring close to the equivalent radius.

Different interpretation could be proposed. For axi-symmetric geometries, the

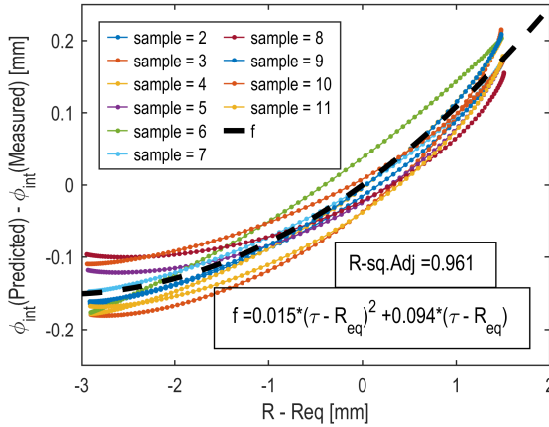


Figure 3.38. Difference between the predicted and measured internal profile as function of the difference between the radial coordinate and the equivalent radius.

anisotropy in the compaction plane was attributed to the inhomogeneity of the stress field acting on powder columns with different heights. In this case the stress field occurring during compaction is unknown, and the geometry is not multilevel.

An influence of the geometry on the anisotropy in the compaction plane could be hypothesized. Maybe the use of the curvature radius instead of radial coordinate could provide a better prediction of the internal profile. Further work, investigating ring samples having the same $H/2T$ in proximity of the major and minor axis, may clarify the effect of geometry.

Due to the predictable trend of errors, the corrective function derived in figure 3.38 was proposed, expressed by equation (3.46).

$$\phi_{int}Pred - \phi_{int}Meas = 0.015(\tau - R_{eq})^2 + 0.094(\tau - R_{eq}) \quad (3.46)$$

By equation (3.46), the internal “diameter” of the cavity can be predicted by equation (3.47).

$$\phi_{int}Pred\ corr = \phi_{int}Pred - \left[0.015(\tau - R_{eq})^2 + 0.094(\tau - R_{eq}) \right] \quad (3.47)$$

Examples of the dimensional prediction of internal profile before and after the application of the corrective function is showed in figures 3.39 and 3.40.

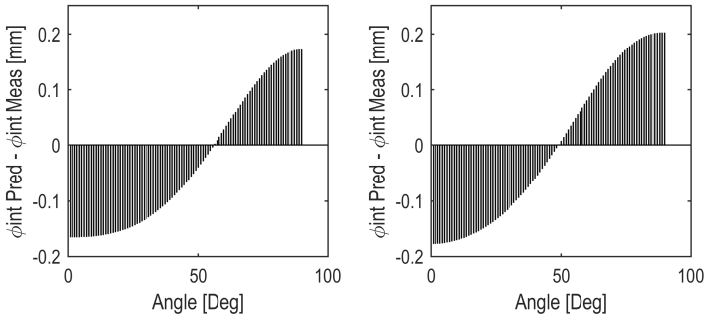


Figure 3.39. Example of difference between the predicted and measured internal profile as derived by the design procedure.

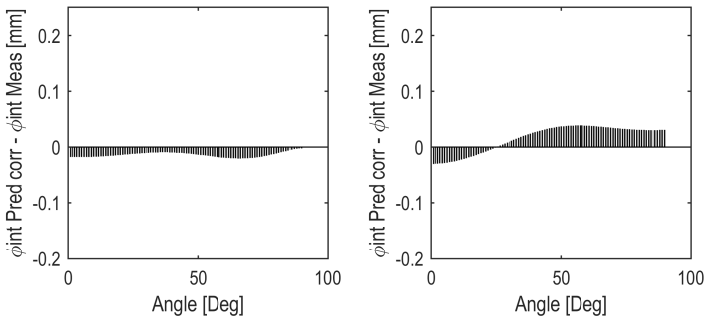


Figure 3.40. Example of the effect of the corrective function expressed by equation (3.47) on the difference between the predicted and measured profile displayed in figure 3.39.

By the corrective function, the discrepancy between the predicted and measured profile is dramatically reduced, within the tolerance limit of ± 0.050 millimeters.

In conclusion, the analysis of the non-cylindrical geometry demonstrates that the design procedure can be also employed for the prevision of the complex profiles, providing that it is implemented with proper corrective functions.

3.5.7 ISO IT tolerance classes

In section 1.3, the quantitative description of the product dimensional accuracy through the ISO IT classes was explained. The conventional P&S process guarantees a tolerance range between IT8-10 in accordance to the reference. The prevision of the anisotropic dimensional change must be related to the attainable tolerance.

Under the hypothesis that the discrepancy between the nominal and actual dimensions derives from the inaccurate estimation of the dimensional change, the design procedure can be considered from a new perspective. The measured dimensions at the sintered state must be compared to the nominal dimensions, then the difference between the predicted and measured dimensions must be compared to the tolerance achievable by the production process. Following this logical sequence, the ISO IT classes were calculated for the dimensions of the five parts, and they were grouped in tolerances related to external, internal diameters and height, as shown in figure 3.41. The results are grouped by the increasing size.

The IT classes of the internal diameters improve on decreasing the size, whereas other dimensions do not display a clear trend. The tolerances associated to the diameters are in some case comparable with the attainable values by conventional process, whereas in other cases are lower. Concerning the heights, the tolerance classes are always lower with respect to the conventional process capability.

By the comparison of the three graphs, it is concluded that IT9 is the maximum value obtained, and in most of the cases the IT tolerances are lower or much lower. Therefore, these results demonstrate the accuracy and the effectiveness of design procedure. Despite the limits highlighted during this test-bed, the design procedure accounting for anisotropic dimensional changes could strongly improve the precision of the produced PM parts.

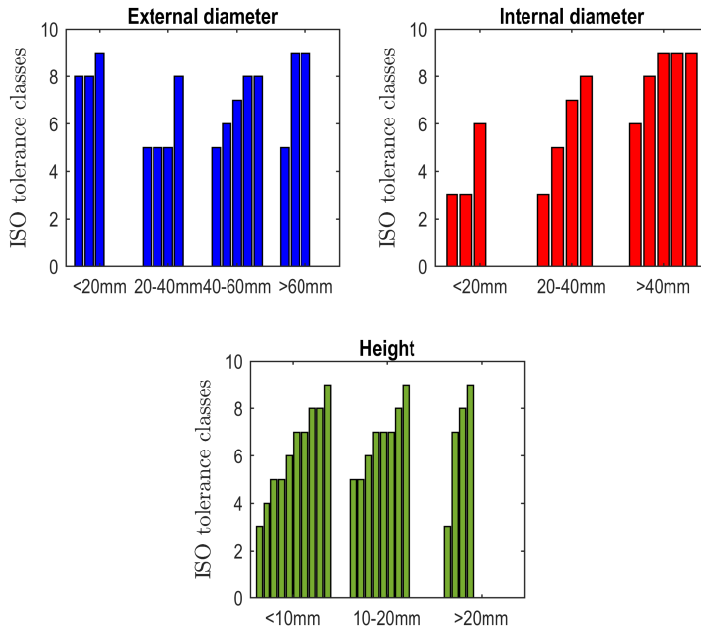


Figure 3.41. ISO IT classes determined for external diameters (left), internal diameters (right) and heights (center) of the five parts investigated.

3.6 Critical analysis of anisotropic parameters K_{anis} , α

The difference between the measured and predicted dimensions was attributed to the improper estimation of the actual anisotropic behavior by the design procedure. In order to assess the effectiveness of the anisotropic empirical relationships, K_{anis} and α used in the model were compared with the corresponding values experimentally determined by the dimensional changes of the ring elements identified on the five geometries. The experimental values of K_{anis} were calculated by equation (3.23), and α values by equation (3.31). Despite the fictitious rings²⁰ identified by the geometry break down cannot strictly represent real simple rings, as in the previous experimental

²⁰The actual anisotropic behavior of the complex geometries was described in section 3.5.2, while the anisotropic variation of the fictitious rings identified by the break down approach is an approximate representation of the actual condition. The limitations of the design procedure were highlighted by comparing the different results.

campaign, the comparison provides interesting conclusions.

In figure 3.42, K_{anis} calculated as above described and K_{anis} derived from the relationship used for the design procedure are reported, distinguishing small and high change in volume.

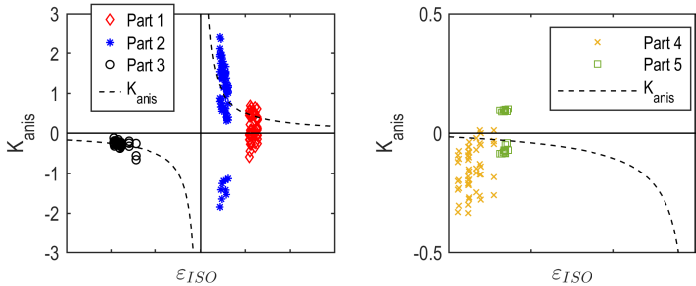


Figure 3.42. K_{anis} anisotropic coefficient determined by the fictitious rings derived from the break down of the complex geometries versus the isotropic dimensional change . On the left the geometries showing small change in volume, on the right the geometries showing large change in volume.

Preliminary analysis evidences that experimental K_{anis} values are just partially overlapped with the relationship employed by the design procedure, due to the different materials and process condition investigated, compared to the original database.

Further analysis showed that the calculated values of K_{anis} may be both negative and positive at the same ϵ_{ISO} values. This result is in contrast with the hypothesis that the anisotropy between the axial and radial direction exclusively depends on ϵ_{ISO} . Two explanations are proposed.

As previously hypothesized, ϵ_{ISO} might not be constant in all the ring-shaped elements identified by the break-down strategy. Therefore, an overestimation or an underestimation of the local change in volume might determine the misleading estimation of K_{anis} . An additional interpretation is based on the influence of the anisotropy in the compaction plane, which might also affect the dimensional change of height. As a consequence, the anisotropy parameters K_{anis} and α would be correlated and not independent from each other.

α experimental coefficients were calculated by equation (3.31) and the results are shown in figure 3.43.

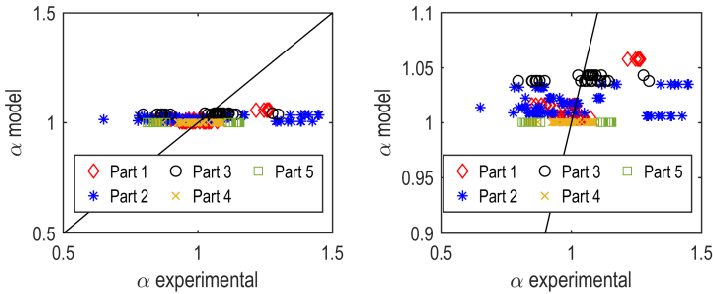


Figure 3.43. α coefficients calculated by the experimental measurements of the fictitious rings derived from the break down of the complex geometries

The experimental data in figure 3.43 are spread within a large range ($0.65 \div 1.45$). Only 50% of data were included within the range ($0.9 \div 1.1$), which could represent isotropic dimensional changes in the compaction plane. No relation with the geometry was identified.

The wide dispersion of α clearly evidences the complexity of the description of anisotropy in P&S. The results might be related to the inhomogeneity of the stress field developed in the compaction plane during the compaction operation. A preferential orientation of particles and pores in the compaction plane could originate the observed anisotropy, as observed in the compaction direction. Therefore, α cannot be defined simply on the basis of the geometry.

3.7 Conclusion

The design procedure accounting for the anisotropic dimensional changes has been validated on real parts in order to evaluate its accuracy in predicting dimensional changes.

The discrepancy in diameters and heights prediction in the case of small change in volume is lower than 0.15% and would correspond to tolerance classes lower than IT9. The difference in the case of high change in volume is lower than 0.25%, and corresponds to the tolerance class IT9. After a deep analysis, it was highlighted that the inaccuracy of the prediction depends on:

- the anisotropic relationships. They were determined on limited amount of materials, geometries and process conditions, not strictly corresponding to the parts studied. For this reason, the anisotropic behavior of the five parts was not exactly predicted in all the cases. Concerning K_{anis} relationship, its dependence on isotropic dimensional change is confirmed, but there is also an effect of geometry. The analysis of the dimensional change in the compaction plane (α) showed an anisotropy behavior difficult to be interpreted. This result might depend on the stress field in the compaction plane, which is more or less constant in a ring-shaped sample, whereas in a complex geometry it might be influenced by the shear stress between adjacent powder columns. The correct modeling of α is one of the most challenging tasks in the future development of the design procedure.
- The assumption of an independent behavior of the anisotropy in the compaction plane (α) and in the compaction direction (K_{anis}). The analysis of the five parts evidenced that large inhomogeneity of the dimensional variation in the compaction plane also affects the dimensional change in the compaction direction. Again, the reason might be the stress anisotropy occurred in compaction.
- The isotropic dimensional variation. In this project, it was calculated on the basis of the sintered and green dimensions. However, for future employment of the design procedure it should be determined by alternative methods. Measurement of density variation or dilatometer test might be possible alternatives. In addition, the measurement of dimensions which are placed above and below the neutral axis evidence a different dimensional change. The reason might be the difference in densification due to the inhomogeneity in green density, or the inhomogeneous heating on sintering. To properly describe

such inhomogeneities, the design procedure should use a local definition of the isotropic dimensional change instead of the average value.

In conclusion, the test-bed demonstrated that the design procedure can be an effective tool for the prediction of anisotropic dimensional change on sintering. The most valuable characteristic is the simplicity of the application, which does not require the use of complicated design tools or material models.

The industrial partners demonstrated deep interest on improving the design procedure and financed a dedicated three years project, investigating different materials, geometries and process conditions in order to enlarge the database, thus providing more effective empirical relationships describing the anisotropic behavior.

Conclusions and future works

This work investigated the complex phenomenon of the anisotropic dimensional change on sintering of prior uniaxially cold compacted products. The phenomenon is scientifically relevant, and has strong industrial implications, so the study has been approached from both a scientific and a practical perspective. The related mechanisms have been investigated in depth, and a design procedure to predict the anisotropic dimensional changes has been proposed and validated on real parts.

The origin of the anisotropic dimensional change on sintering, as determined by prior uniaxial compaction, was firstly investigated. The measured dimensional changes of ring-shaped parts have been related to the triaxial stress field in compaction, as derived from the forces and displacements recorded by the press. A linear relationship between the deviatoric components of the stress tensor and the deviatoric components of the dimensional changes has been obtained. This result confirms the role of uniaxial compaction on the origin of anisotropic dimensional change on sintering as commonly accepted in literature. The novelty of the work consists in the quantification of the anisotropic behavior as a function of the stress state, which might be implemented in an integrated tool for development of P&S products from compaction to sintering. Future work will test and validate the application of this novel description of stress-shrinkage behavior on a multilevel geometry. In addition, further works should strength the experimental observation of the linear dependence of stress-shrinkage behavior on a wide range of compaction and sintering process conditions.

From an industrial perspective, a design procedure for the prediction of the anisotropic of dimensional changes has been tested on real parts within an EPMA Club Project. The parts were different for material, geometry, size, and process conditions. Despite some inaccuracy, this procedure proved to be an effective tool for estimating the anisotropic dimensional changes on real parts. Deep analysis of the results allowed highlighting directions for further improvement. The procedure uses experimentally derived relationships, and the need for enlarging the database emerged from this study. A new extensive experimental campaign has been planned in agreement with the company partners, which are now supporting a further project to investigate new materials and process conditions.

In conclusion, it can be assumed that further investigation on phenomenological

mechanisms, to be implemented in a more reliable design procedure, thanks to the enlarged database, will allow obtaining a powerful design tool predicting anisotropic dimensional changes.

References

- [1] Furrer, D. and S. Semiatin, *ASM Handbook: Metals Process Simulation. Volume 22B*. ASM International, **2010**.
- [2] Wollaston, W. H. *Phil. Trans. Roy. Soc.*, **1829**, 119: 1–8.
- [3] Sobolevsky, P. G. *Ann. Der Physik und Chemie*, **1834**, 33(7): 99–109.
- [4] Coolidge, W. D., *Tungsten and method of making the same for use as filaments of incandescent electric lamps and for other purpose*. U.S. Patent No. 1,082,938, **1913**.
- [5] Lowendahl, V., *Process of Manufacturing Porous Metal Blocks*. U. S. Patent 1,051,814, **1913**.
- [6] Schroter, K., *Hard-metal alloy and the process of making same*. U.S. Patent 1,549,615, **1925**.
- [7] Dowson, G., *Introduction to powder metallurgy: the process and its products*. EPMA, **1990**.
- [8] *Vision 2025 – Future Developments for the European PM Industry*. <https://www.epma.com/>, **accessed: 14.04.2020**.
- [9] Šalák, A., *Ferrous Powder Metallurgy*. Cambridge International Science Pub., **1995**.
- [10] B331-95, A., *Standard Test Method for Compressibility of Metal Powders in Uniaxial Compaction*. ASTM International.
- [11] Heckel, R., *A normalized density-pressure curve for powder compaction*. *Trans Metall Soc AIME*, **1962**, 224(5): 1073–1074.
- [12] Cytermann, R. and R. Geva, *Development of new model for compaction of powders*. *Powder Metallurgy*, **1987**, 30(4): 256–260.
- [13] Rong-de, G., *A new powder compaction equation*. *International journal of powder metallurgy* (1986), **1991**, 27(3): 211–216.

- [14] Li, S., P. B. Khosrovabadi, and B. H. Kolster, *New compaction equation for powder materials*. International journal of powder metallurgy (1986), **1994**, 30(1): 47–57.
- [15] Panelli, R. and F. Ambrozio Filho, *Compaction equation and its use to describe powder consolidation behavior*. Powder metallurgy, **1998**, 41(2): 131–133.
- [16] Secondi, J., *Modelling powder compaction: from a pressure-density law to continuum mechanics*. Powder metallurgy, **2002**, 45(3): 213–217.
- [17] Parilak, L., E. Dudrova, R. Bidulsky, and M. Kabatova, *Derivation, testing and application of a practical compaction equation for cold die-compacted metal powders*. Powder Technology, **2017**, 322: 447–460.
- [18] Aryanpour, G. and M. Farzaneh, *Application of a piston equation to describe die compaction of powders*. Powder Technology, **2015**, 277: 120–125.
- [19] Molinari, A., I. Cristofolini, G. Pederzini, and A. Rambelli, *The densification equation in uniaxial cold compaction of a water-atomized 316L stainless steel powder*. International Journal of Powder Metallurgy, **2017**, 53(3): 41–48.
- [20] Molinari, A., I. Cristofolini, G. Pederzini, and A. Rambelli, *A densification equation derived from the stress-deformation analysis of uniaxial cold compaction of metal powder mixes*. Powder Metallurgy, **2018**, 61(3): 210–218.
- [21] Montes, J., F. Cuevas, J. Cintas, F. Ternero, and E. Caballero, *On the compressibility of metal powders*. Powder Metallurgy, **2018**, 61(3): 219–230.
- [22] Cristofolini, I., A. Molinari, M. Zago, G. Pederzini, and A. Rambelli, *The analysis of the densification curve of metallic powders in uniaxial cold compaction*. Advances in Powder Metallurgy and Particulate Materials - 2019: Proceedings of the 2019 International Conference on Powder Metallurgy and Particulate Materials, **2020**, pp. 30–41.
- [23] Fischer, A. and K. Bobzin, *Friction, Wear and Wear Protection*, vol. Part II Lectures. Wiley, **2011**.
- [24] Bocchini, G., *Friction effects in metal powder compaction. I. Theoretical aspects*. Advances in Powder Metallurgy and Particulate Materials–1995., **1995**, 1: 2.

- [25] AB, H., *Höganäs Handbook for Sintered Components, Production of sintered components*. <https://books.google.it/books?id=B-nVZwEACAAJ>, **2004**, 2: 17.
- [26] H. H. Hausner, I. S., *Friction and lubrication in powder metallurgy*. Metal Powder Assoc: Proceedings of the Eleventh Annual Meeting New York (USA), **1954**, pp. 6–27.
- [27] Timoshenko, S. and J. Goodier, *Theory of Elasticity*. Engineering societies monographs, McGraw-Hill, **1982**.
- [28] Fahad, M., *Stresses and failure in the diametral compression test*. Journal of Materials Science, **1996**, 31(14): 3723–3729.
- [29] Martin, C. L., D. Bouvard, and G. Delette, *Discrete element simulations of the compaction of aggregated ceramic powders*. Journal of the American Ceramic Society, **2006**, 89(11): 3379–3387.
- [30] Bierwisch, C., T. Kraft, H. Riedel, and M. Moseler, *Die filling optimization using three-dimensional discrete element modeling*. Powder technology, **2009**, 196(2): 169–179.
- [31] Green, R., *A plasticity theory for porous solids*. International Journal of Mechanical Sciences, **1972**, 14(4): 215–224.
- [32] Shima, S. and M. Oyane, *Plasticity theory for porous metals*. International Journal of Mechanical Sciences, **1976**, 18(6): 285–291.
- [33] Gurson, A. L., *Continuum Theory of Ductile Rupture by Void Nucleation and Growth: Part 1-Yield Criteria and Flow Rules for Porous Ductile Media*. Journal of Engineering Materials and Technology, **1977**, 99: 2–15.
- [34] Roscoe, K., A. Schofield, and A. Thurairajah, *Yielding of clays in states wetter than critical*. Geotechnique, **1963**, 13(3): 211–240.
- [35] Schofield, A. and P. Wroth, *Critical state soil mechanics*. McGraw-hill, **1968**.
- [36] Parry, R. and K. Roscoe, *Stress-Strain Behaviour of Soils: Proceedings of the Roscoe Memorial Symposium, Cambridge University, 29-31 March 1971*. Foulis, **1971**.

- [37] Drucker, D. C. and W. Prager, *Soil mechanics and plastic analysis or limit design*. Quarterly of applied mathematics, **1952**, 10(2): 157–165.
- [38] 3252:1999, I., *Powder Metallurgy - Vocabulary*, **1999**.
- [39] German, R., *Powder Metallurgy of Iron and Steel*. Wiley, **1998**.
- [40] Kang, S., *Sintering: Densification, Grain Growth and Microstructure*. Elsevier Science, **2004**.
- [41] Kingery, W., *Densification during sintering in the presence of a liquid phase. I. Theory*. Journal of Applied Physics, **1959**, 30(3): 301–306.
- [42] Cannon, H. and F. Lenel, *Some observations on the mechanism of liquid phase sintering*. Pulvermetallurgie (Plansee Proceedings 1952). Reutte: Metallwerk Plansee GmbH, **1953**, pp. 106–22.
- [43] German, R., *Sintering: From Empirical Observations to Scientific Principles*. Elsevier Science, **2014**.
- [44] German, R., *Sintering Theory and Practice*. Wiley, **1996**.
- [45] German, R., *Powder Metallurgy Science*. Metal Powder Industries Federation, **1994**.
- [46] German, R., *Liquid Phase Sintering*. Springer US, **2013**.
- [47] Kingery, W. D. and M. Berg, *Study of the initial stages of sintering solids by viscous flow, evaporation-condensation, and self-diffusion*. Journal of Applied Physics, **1955**, 26(10): 1205–1212.
- [48] Coble, R. L., *Sintering crystalline solids. I. Intermediate and final state diffusion models*. Journal of applied physics, **1961**, 32(5): 787–792.
- [49] Skorokhod, V. and S. Solonin, *Kinetics of interparticle contact growth in the sintering of unpressed powders*. Soviet Powder Metallurgy and Metal Ceramics, **1972**, 11(2): 141–145.
- [50] Kuczynski, G., *Statistical approach to the theory of sintering*. In *Sintering and Catalysis*, Springer, pp. 325–337, **1975**.
- [51] Kuczynski, G., *Statistical Theory of Sintering*., **1976**.

- [52] Kuczynski, G., 'Science of sintering', *Monographs of the Serbian Academy of Sciences and Arts*. Serbian Academy of Sciences and Arts, **1978**, 59(17): 67–606.
- [53] Exner, H., *Solid-state sintering: critical assessment of theoretical concepts and experimental methods*. Powder Metallurgy, **1980**, 23(4): 203–209.
- [54] Cahn, R. and P. Haasen, *Physical Metallurgy*. No. v. 1 in Physical Metallurgy, Elsevier Science, **1996**.
- [55] Molinari, A., E. Bisoffi, C. Menapace, and J. Torralba, *Shrinkage kinetics during early stage sintering of cold isostatically compacted iron powder*. Powder metallurgy, **2014**, 57(1): 61–69.
- [56] Molinari, A., C. Menapace, E. Torresani, I. Cristofolini, and M. Larsson, *Working hypothesis for origin of anisotropic sintering shrinkage caused by prior uniaxial cold compaction*. Powder metallurgy, **2013**, 56(3): 189–195.
- [57] Molinari, A., E. Torresani, C. Menapace, and M. Larsson, *The anisotropy of dimensional change on sintering of iron*. Journal of the American Ceramic Society, **2015**, 98(11): 3431–3437.
- [58] Baselli, S., E. Torresani, M. Zago, S. Amirabdollahian, I. Cristofolini, and A. Molinari, *Sintering shrinkage of uniaxial cold compacted iron: influence of the microstructure on the anisothermal and isothermal shrinkage of uniaxial cold-compacted iron*. Powder Metallurgy, **2018**, 61(4): 276–284.
- [59] Baselli, S. and A. Molinari, *Sintering shrinkage of uniaxial cold compacted iron: a new shrinkage kinetic equation accounting for the microstructure of green parts*. Powder Metallurgy, **2019**, 62(1): 1–7.
- [60] Moitra, A., S. Kim, S.-G. Kim, S. J. Park, R. M. German, and M. F. Horstemeyer, *Investigation on sintering mechanism of nanoscale tungsten powder based on atomistic simulation*. Acta Materialia, **2010**, 58(11): 3939–3951.
- [61] Zachariah, M. R. and M. J. Carrier, *Molecular dynamics computation of gas-phase nanoparticle sintering: a comparison with phenomenological models*. Journal of Aerosol Science, **1999**, 30(9): 1139–1151.

- [62] Strobel, M., K.-H. Heinig, and W. Möller, *Three-dimensional domain growth on the size scale of the capillary length: Effective growth exponent and comparative atomistic and mean-field simulations*. *Physical Review B*, **2001**, 64(24): 245422.
- [63] Bouvard, D. and R. McMeeking, *Deformation of interparticle necks by diffusion-controlled creep*. *Journal of the American Ceramic Society*, **1996**, 79(3): 666–672.
- [64] Martin, C. and R. Bordia, *The effect of a substrate on the sintering of constrained films*. *Acta Materialia*, **2009**, 57(2): 549–558.
- [65] Skorohod, V., *Rheological basis of the theory of sintering*. Kiev: Naukova Dumka, **1972**, p. 1972.
- [66] Olevsky, E. A., *Theory of sintering: from discrete to continuum*. *Materials Science and Engineering: R: Reports*, **1998**, 23(2): 41–100.
- [67] Olevsky, E. A., V. Tikare, and T. Garino, *Multi-scale study of sintering: a review*. *Journal of the American Ceramic Society*, **2006**, 89(6): 1914–1922.
- [68] Su, H. and D. L. Johnson, *Master sintering curve: a practical approach to sintering*. *Journal of the American Ceramic Society*, **1996**, 79(12): 3211–3217.
- [69] Bollina, R., S. Park, and R. M. German, *Master sintering curve concepts applied to full-density supersolidus liquid phase sintering of 316L stainless steel powder*. *Powder metallurgy*, **2010**, 53(1): 20–26.
- [70] Blaine, D. C., S.-J. Park, and R. M. German, *Linearization of master sintering curve*. *Journal of the American Ceramic Society*, **2009**, 92(7): 1403–1409.
- [71] Park, S. J., R. M. German, J. Martin, J. Guo, and J. Johnson, *Densification behavior of tungsten heavy alloy based on master sintering curve concept*. *Metallurgical and Materials Transactions A*, **2006**, 37(9): 2837–2848.
- [72] Chang, I. and Y. Zhao, *Advances in Powder Metallurgy: Properties, Processing and Applications*. Woodhead Publishing Series in Metals and Surface Engineering, Elsevier Science, **2013**.
- [73] Schatt, W., E. P. M. Association, and K. Wieters, *Powder metallurgy: processing and materials*. European Powder Metallurgy Association, **1997**.

- [74] Assinter, *Guida alla progettazione dei componenti sinterizzati*. Associazione Italiana di Metallurgia.
- [75] German, R. M., *Introduction to Liquid Phase Sintering*, Springer US, Boston, MA, pp. 1–11, **1985**.
- [76] Lenel, F., H. Hausner, E. Hayashi, and G. Ansell, *Some Observations on the Shrinkage Behaviour of Copper Compacts and of Loose Powder Aggregates*. Powder Metallurgy, **1961**, 4(8): 25–36.
- [77] Wanibe, Y., N. Fujitsuna, T. Itoh, and H. Yokoyama, *Anisotropic shrinkage and thermal expansion during sintering of cylindrical nickel and iron compacts*. Powder metallurgy, **1989**, 32(3): 191–194.
- [78] Mizuno, Y., A. Kawasaki, and R. Watanabe, *In situ measurement of sintering shrinkage in powder compacts by digital image correlation method*. Powder metallurgy, **1995**, 38(3): 191–195.
- [79] Cutler, I. B. and R. E. Henrichsen, *Effect of particle shape on the kinetics of sintering of glass*. Journal of the American Ceramic Society, **1968**, 51(10): 604–604.
- [80] Giess, E. A., C. F. Guerci, G. F. Walker, and S. H. Wen, *Isothermal Sintering of Spheroidized Cordierite-Type Glass Powders*. Journal of the American Ceramic Society, **1985**, 68(12): C–328.
- [81] Raj, P. M. and W. R. Cannon, *Anisotropic shrinkage in tape-cast alumina: Role of processing parameters and particle shape*. Journal of the American Ceramic Society, **1999**, 82(10): 2619–2625.
- [82] Shui, A., N. Uchida, and K. Uematsu, *Origin of shrinkage anisotropy during sintering for uniaxially pressed alumina compacts*. Powder technology, **2002**, 127(1): 9–18.
- [83] Heaney, D., *Handbook of Metal Injection Molding*. Woodhead Publishing Series in Metals and Surface Engineering, Elsevier Science, **2019**.
- [84] Binet, C., D. Heaney, J. Piemme, and P. Burke, *An Investigation of Particle Orientation and How it Relates to Anisotropic Shrinkage*. Advances in Powder Metallurgy and Particulates Materials, **2002**, (10): 10–210.

- [85] Zavaliangos, A., J. Missiaen, and D. Bouvard, *Anisotropy in shrinkage during sintering*. Science of Sintering, **2006**, 38(1): 13–25.
- [86] Cyunczyk, A., *Anisotropy of shrinkage during sintering of iron powder compacts pressed under static or vibrating load*. PMI. Powder metallurgy international, **1979**, 11(4): 162–164.
- [87] El-Shanshoury, I., *Radial and axial contraction of metal powder pressings*. Soviet Powder Metallurgy and Metal Ceramics, **1965**, 4(4): 342–345.
- [88] El-Shanshoury, I. and M. Nazmy, *Factors affecting the radial and axial shrinkage in soft-metal powder compacts*. Powder Metallurgy, **1968**, 11(21): 63–72.
- [89] Roman, O. V. and H. H. Hausner, *Investigation in the linear shrinkage of metal powder compacts during sintering*. Journal of the Japan Society of Powder and Powder Metallurgy, **1962**, 9(6): 228–236.
- [90] Kuroki, H., *Anisotropic spring-back and shrinkage of iron powder compact*. In *Key Engineering Materials*, Trans Tech Publ, vol. 29, **1988** pp. 365–372.
- [91] Kuroki, H. and M. Hiraishi, *Mechanism of anisotropic dimensional changes during sintering of metal powder compact*. In *Science of sintering*, Springer, pp. 91–98, **1989**.
- [92] Lame, O., D. Bellet, M. Di Michiel, and D. Bouvard, *Bulk observation of metal powder sintering by X-ray synchrotron microtomography*. Acta materialia, **2004**, 52(4): 977–984.
- [93] Vagnon, A., O. Lame, D. Bouvard, M. Di Michiel, D. Bellet, and G. Kapelski, *Deformation of steel powder compacts during sintering: Correlation between macroscopic measurement and in situ microtomography analysis*. Acta Materialia, **2006**, 54(2): 513–522.
- [94] Olevsky, E. and V. Skorohod, *Deformation aspects of anisotropic-porous bodies sintering*. Le Journal de Physique IV, **1993**, 3(C7): C7–739.
- [95] Olevsky, E., B. Kushnarev, A. Maximenko, V. Tikare, and M. Braginsky, *Modelling of anisotropic sintering in crystalline ceramics*. Philosophical Magazine, **2005**, 85(19): 2123–2146.

- [96] Torresani, E., D. Giuntini, C. Zhu, T. Harrington, K. Vecchio, A. Molinari, R. K. Bordia, and E. A. Olevsky, *Anisotropy of Mass Transfer During Sintering of Powder Materials with Pore–Particle Structure Orientation*. Metallurgical and Materials Transactions A, **2019**, 50(2): 1033–1049.
- [97] ISO-10360-2, *Geometrical product specifications (GPS)–acceptance and reverification tests for coordinate measuring machines (CMM)–part 2: CMMs used for measuring linear dimensions*, **2009**.
- [98] Flack, D., *Good practice guide no. 43 CMM probing*. National Physical Laboratory, **2014**, pp. 6–11.
- [99] Amirabdollahian, S., I. Cristofolini, and A. Molinari, *Coordinate Measuring Machines (CMM) in Measurements of PM Parts - Influence of measurement strategy and data processing*. Euro PM 2018 Congress and Exhibition, **2018**.
- [100] Sinka, I., A. Cocks, and J. Tweed, *Constitutive data for powder compaction modeling*. J. Eng. Mater. Technol., **2001**, 123(2): 176–183.
- [101] Chtourou, H., M. Guillot, and A. Gakwaya, *Modeling of the metal powder compaction process using the cap model. Part I. Experimental material characterization and validation*. International Journal of Solids and Structures, **2002**, 39(4): 1059–1075.
- [102] Dorémus, P., C. Geindreau, A. Martin, L. Debove, R. Lecot, and M. Dao, *High pressure triaxial cell for metal powder*. Powder Metallurgy, **1995**, 38(4): 284–287.
- [103] Guyoncourt, D., J. Tweed, A. Gough, J. Dawson, and L. Pater, *Constitutive data and friction measurements of powders using instrumented die*. Powder Metallurgy, **2001**, 44(1): 25–33.
- [104] Mosbah, P., D. Bouvard, E. Ouedraogo, and P. Stutz, *Experimental techniques for analysis of die pressing and ejection of metal powder*. Powder Metallurgy, **1997**, 40(4): 269–277.
- [105] Sinka, I., J. McStea, and J. Sainsbury, *Tools for Improving PM: A New Apparatus for Calibration of Constitutive Models and Friction for Powder Compaction*. European Congress and Exhibition on Powder Metallurgy. European PM Conference Proceedings, **2008**, 3: 175.

- [106] Zhou, M., S. Huang, J. Hu, Y. Lei, Y. Xiao, B. Li, S. Yan, and F. Zou, *A density-dependent modified Drucker-Prager Cap model for die compaction of Ag57. 6-Cu22. 4-Sn10-In10 mixed metal powders*. Powder Technology, **2017**, 305: 183–196.
- [107] Geindreau, C., D. Bouvard, and P. Doremus, *Constitutive behaviour of metal powder during hot forming. Part I: Experimental investigation with lead powder as a simulation material*. European Journal of Mechanics-A/Solids, **1999**, 18(4): 581–596.
- [108] Zhang, B., M. Jain, C. Zhao, M. Bruhis, R. Lawcock, and K. Ly, *Experimental calibration of density-dependent modified Drucker-Prager/Cap model using an instrumented cubic die for powder compact*. Powder technology, **2010**, 204(1): 27–41.
- [109] Almanstötter, J., *A modified Drucker-Prager Cap model for finite element simulation of doped tungsten powder compaction*. International Journal of Refractory Metals and Hard Materials, **2015**, 50: 290–297.
- [110] Falgon, D., E. Vidal-Sallé, J.-C. Boyer, R. Peczalski, and J. Andrieu, *Identification procedure of a hardening law for powder compaction*. Powder technology, **2005**, 157(1-3): 183–190.
- [111] Majzoobi, G. and S. Jannesari, *Determination of the constants of cap model for compaction of three metal powders*. Advanced Powder Technology, **2015**, 26(3): 928–934.
- [112] Stribos, S., *Powder–wall friction: The effects of orientation of wall grooves and wall lubricants*. Powder Technology, **1977**, 18(2): 209–214.
- [113] Cameron, I., D. Gethin, and J. Tweed, *Friction measurement in powder die compaction by shear plate technique*. Powder metallurgy, **2002**, 45(4): 345–353.
- [114] Pm, *Measurement of friction for powder compaction modelling–comparison between laboratories*. Powder Metallurgy, **2000**, 43(4): 364–374.
- [115] Oppenheim, A., *Discrete-Time Signal Processing*. Pearson education signal processing series, Pearson Education, **1999**.
- [116] Gustafsson, F., *Determining the initial states in forward-backward filtering*. IEEE Transactions on signal processing, **1996**, 44(4): 988–992.

- [117] Zago, M., I. Cristofolini, A. Molinari, G. Pederzini, and A. Rambelli, *Processing method to improve the reliability of data recorded by an industrial press in describing powder behavior during uniaxial cold compaction*. Euro PM 2018 Congress and Exhibition, **2018**.
- [118] Han, L., J. Elliott, A. Bentham, A. Mills, G. Amidon, and B. Hancock, *A modified Drucker-Prager Cap model for die compaction simulation of pharmaceutical powders*. International Journal of Solids and Structures, **2008**, 45(10): 3088–3106.
- [119] Cristofolini, I., A. Molinari, G. Pederzini, and A. Rambelli, *Study of the uniaxial cold compaction of AISI 316L stainless steel powders through single action tests*. Powder Technology, **2016**, 295: 284–295.
- [120] Carnavas, P. and N. Page, *Elastic properties of compacted metal powders*. Journal of materials science, **1998**, 33(18): 4647–4655.
- [121] Timoshenko, S. and S. Woinowsky-Krieger, *Theory of Plates and Shells*. Engineering mechanics series, McGraw-Hill, **1959**.
- [122] Pavier, E. and P. Doremus, *Friction behavior of an iron powder investigated with two different apparatus*. International Workshop on Modelling of Metal Powder Forming Processes, Grenoble, France, **1997**, 21: 335–344.
- [123] Wikman, B., N. Solimannezhad, R. Larsson, M. Oldenburg, and H. H.-A., *Wall friction coefficient estimation through modelling of powder die pressing experiment*. Powder metallurgy, **2000**, 43(2): 132–138.
- [124] Solimanjad, N., *New method for measuring and characterisation of friction coefficient at wide range of densities in metal powder compaction*. Powder metallurgy, **2003**, 46(1): 49–54.
- [125] Solimanjad, N. and R. Larsson, *Die wall friction and influence of some process parameters on friction in iron powder compaction*. Materials science and technology, **2003**, 19(12): 1777–1782.
- [126] Heckel, R., *Density-pressure relationships in powder compaction*. Trans Metall Soc AIME, **1961**, 221(4): 671–675.
- [127] Peterson, J. and W. Small, *Evaluation of metal powders using Arnold density meter and Hall flowmeter*. Powder metallurgy, **1994**, 37(1): 37–41.

- [128] Rice, E. and J. Tengzelius, *Die filling characteristics of metal powders*. Powder Metallurgy, **1986**, 29(3): 183–194.
- [129] Höganäs AB website. https://www.hoganas.com/globalassets/download-media/sharepoint/brochures-and-datasheets---all-documents/stainless_steel_powders_for_sintered_components.pdf, **accessed: 14.04.2020**.
- [130] German, R. M., *Prediction of sintered density for bimodal powder mixtures*. Metallurgical Transactions A, **1992**, 23(5): 1455–1465.
- [131] B212-17, A., *Standard Test Method for Apparent Density of Free-Flowing Metal Powders Using the Hall Flowmeter Funnel*. ASTM International, **2017**.
- [132] B417-18, A., *Standard Test Method for Apparent Density of Non-Free-Flowing Metal Powders Using the Carney Funnel*. ASTM International, **2018**.
- [133] ISO3923-1:2018, *Metallic powders — Determination of apparent density — Part 1: Funnel method*, **2018**.
- [134] Al-Qureshi, H., A. Galiotto, and A. Klein, *On the mechanics of cold die compaction for powder metallurgy*. Journal of Materials Processing Technology, **2005**, 166(1): 135–143.
- [135] Hassanpour, A. and M. Ghadiri, *Distinct element analysis and experimental evaluation of the Heckel analysis of bulk powder compression*. Powder Technology, **2004**, 141(3): 251–261.
- [136] Fischmeister, H. F. and E. Arzt, *Densification of powders by particle deformation*. Powder Metallurgy, **1983**, 26(2): 82–88.
- [137] Hirschhorn, J. S., G. M. Maxwell, and A. V. Nadkarni, *Effect of particle shape and size on the shrinkage of stainless steel compacts*. Powder Technology, **1972**, 5(3): 147–154.
- [138] Höges, S., *Strategic partnership of GKN-HP-VW for binder additive manufacturing*. EuroPM2019 SIS Metal Injection moulding & Additive Manufacturing, **2019**.

- [139] Höges, S., *Industrialization of Binder Jetting*. Sinter based Additive Manufacturing Seminar, Bremen, **2019**.
- [140] Cristofolini, I., M. Pilla, M. Larsson, and A. Molinari, *A DOE analysis of dimensional change on sintering of a 3% Cr–0.5% Mo–x% C steel and its effect on dimensional and geometrical precision*. Powder Metallurgy Progress, **2012**, 3(12): 127–143.
- [141] Cristofolini, I., N. Corsentino, A. Molinari, and M. Larsson, *Study of the influence of material and geometry on the anisotropy of dimensional change on sintering of Powder Metallurgy parts*. International Journal of Precision Engineering and Manufacturing, **2014**, 15(9): 1865–1873.
- [142] Corsentino, N., C. Menapace, I. Cristofolini, M. Larsson, and A. Molinari, *The influence of the liquid phase on anisotropic dimensional change on sintering iron alloys*. International Journal of Powder Metallurgy, **2015**, 51(2): 27–37.
- [143] Cristofolini, I., C. Menapace, M. Cazzolli, A. Rao, W. Pahl, and A. Molinari, *The effect of anisotropic dimensional change on the precision of steel parts produced by powder metallurgy*. Journal of Materials Processing Technology, **2012**, 212(7): 1513–1519.
- [144] Menapace, C., M. Larsson, E. Torresani, I. Cristofolini, and A. Molinari, *Study of anisotropy during sintering of ferrous alloys*, **2012**, pp. 14–18.
- [145] Cristofolini, I., M. Pilla, A. Molinari, C. Menapace, and M. Larsson, *DOE investigation of anisotropic dimensional change during sintering of iron-copper-carbon*. International journal of powder metallurgy, **2012**, 48(4): 33–44.
- [146] Molinari, A., S. Amirabdollahian, M. Zago, M. Larsson, and I. Cristofolini, *Effect of geometry and green density on the anisotropic sintering shrinkage of axisymmetric iron parts*. Powder Metallurgy, **2018**, 61(4): 267–275.
- [147] Cristofolini, I., M. Pilla, A. Rao, S. Libardi, and A. Molinari, *Dimensional and geometrical precision of powder metallurgy parts sintered and sinterhardened at high temperature*. International journal of precision engineering and manufacturing, **2013**, 14(10): 1735–1742.

- [148] Cristofolini, I., N. Corsentino, M. Pilla, A. Molinari, and M. Larsson, *Influence of geometry on the anisotropic dimensional change on sintering of PM parts*. *Advances in Powder Metallurgy and Particulate Materials*, **2013**, 11: 49–61.
- [149] <https://www.ames-sintering.com/sintered-gears/>, **accessed: 14.04.2020**.
- [150] Federation, M. P. I., *Powder Metallurgy Design Solutions*. Metal Powder Industries Federation, **1999**.
- [151] DIN30912-2, *Sintered metal materials; sint-guide-lines; part 2: designing of sintered parts*. German National Standard, **1990**.
- [152] Cristofolini, I., N. Corsentino, M. Larsson, and A. Molinari, *Analytical model of the anisotropic dimensional change on sintering of ferrous pm parts*. *Powder Metallurgy Progress*, **2016**, 16(1): 27–39.
- [153] Lenel, F., H. Hausner, O. Roman, and G. Ansell, *The influence of gravity in sintering*. *Soviet Powder Metallurgy and Metal Ceramics*, **1963**, 2(5): 379–384.
- [154] Olevsky, E. and R. German, *Effect of gravity on dimensional change during sintering—I. Shrinkage anisotropy*. *Acta materialia*, **2000**, 48(5): 1153–1166.
- [155] Olevsky, E., R. German, and A. Upadhyaya, *Effect of gravity on dimensional change during sintering—II. Shape distortion*. *Acta Materialia*, **2000**, 48(5): 1167–1180.

Scientific production

Paper on journal

1. Molinari, S. Amirabdollahian, M. Zago, M. Larsson, I. Cristofolini, **(2018)** *Effect of geometry and green density on the anisotropic sintering shrinkage of axisymmetric iron parts*, Powder Metallurgy, Vol. 61:4, pp. 267-275.
2. S. Baselli, E. Torresani, M. Zago, S. Amirabdollahian, I. Cristofolini, A. Molinari, **(2018)** *Sintering shrinkage of uniaxial cold compacted iron: influence of the microstructure on the anisothermal and isothermal shrinkage of uniaxial cold-compacted iron*, Powder Metallurgy, Vol.61:4, pp. 276-284.
3. I. Cristofolini, A. Molinari, M. Zago, S. Amirabdollahian, O. Coube, M.J. Dougan, M. Larsson, M. Schneider, P. Valler, J. Voglhuber, L. Wimbart, **(2019)** *Design for powder metallurgy - Predicting anisotropic dimensional change on sintering of real parts*, International Journal of Precision Engineering and Manufacturing, Vol. 20:4, pp. 619-630.
4. M. Zago, I. Cristofolini, A. Molinari, **(2019)** *New interpretation for the origin of the anisotropic sintering shrinkage of AISI 316L rings based on the anisotropic stress field occurred on uniaxial cold compaction*, Powder Metallurgy, Vol. 62:2, pp. 115-123.
5. M. Zago, A. Molinari, A. Rambelli, G. Pederzini, I. Cristofolini, **(2019)** *Study of the influence of geometry and particle size on the densification and compaction mechanics of uniaxially cold compacted rings*, International Journal of Powder Metallurgy, Vol. 55:3, pp. 29-38.

Conference proceedings

1. Molinari, C. Menapace, E. Bisoffi, L. Emanuelli, E. Torresani, S. Baselli, M. Zago, I. Cristofolini *Geometrical and Structural Activity in Sintering of Uniaxially Cold Compacted Metallic Powders*, MS&T2016, Salt Lake City (USA), October 2016.
2. Molinari, M. Zago, S. Amirabdollahian, I. Cristofolini *Anisotropic Sintering Shrinkage of Ring Shaped Iron Parts: Effect of Geometry and Green Density and Correlation To The Stress Field During Uniaxial Cold Compaction*, EuroPM2017, Milan (Italy), October 2017.
3. I. Cristofolini, A. Molinari, M. Zago, G. Pederzini, A. Rambelli, *The influence of H/T ratio on the densification model of AISI 316L powder during uniaxial cold compaction*, in *Advances of Powder Metallurgy & Particulate Materials 2017*, Powdermet 2017 international conference, Las Vegas (USA), June 13-16 2017.
4. I. Cristofolini, A. Molinari, M. Zago, G. Pederzini, A. Rambelli, R. Crosa, F. Della Ricca, (2018) *The influence of lubricant on the constitutive model of low alloy steel powder mix*, *Advances in Powder Metallurgy & Particulate Materials*, PowderMet2018, San Antonio (USA), Part 1, pp. 55-66.
5. A. Molinari, M. Zago, S. Amirabdollahian, I. Cristofolini, *From compaction mechanics to sintering shrinkage of rings with different H/(Dext-Dint) ratio*, *Advances in Powder Metallurgy & Particulate Materials*, PowderMet2018, San Antonio (USA), Part 1, pp. 81-90.
6. I. Cristofolini, M. Zago, G. Pederzini, A. Rambelli, A. Molinari, *Influence of particle size on the compaction of AISI 316L powder uni-axially cold compacted*, WorldPM2018, Pechino (China), pp. 266-273.
7. I. Cristofolini, A. Molinari, M. Zago, S. Amirabdollahian, O. Coube, M. J. Dougan, M. Larsson, M. Schneider, P. Valler, J. Voglhuber, L. Wimbert, *Design for sintering club project – dealing with the anisotropy of dimensional changes in real parts*, EuroPM2018 Congress & Exhibition, Bilbao (Spain).
8. M. Zago, I. Cristofolini, A. Molinari, G. Pederzini, A. Rambelli, *Processing method to improve the reliability of data recorded by an industrial press describing powder behavior during uniaxial cold compaction*, EuroPM2018 Congress & Exhibition, Bilbao (Spain).

9. M. Zago, M. Larsson, I. Cristofolini, (2020) *An improved design method for net-shape manufacturing in powder metallurgy*, Lecture Notes in Mechanical Engineering, pp. 257-267. Springer Nature Switzerland.
10. I. Cristofolini, A. Molinari, M. Zago, G. Pederzini, A. Rambelli, *The analysis of densification curve of metallic powders in uniaxial cold compaction*, Advances in Powder Metallurgy and Particulate Materials, PowderMet2019, Phoenix (USA), Part 1, pp. 30-41.
11. M. Zago, I. Cristofolini, A. Molinari, G. Pederzini, A. Rambelli, (2019) *Study of elasto-plastic transition as affected by particle size during uniaxial cold compaction*, EuroPM2019 Congress & Exhibition, Maastricht (Netherlands).

Acknowledgments

First of all, I want to express my profound gratitude to Prof. Ilaria Cristofolini and Prof. Alberto Molinari for the trust they have placed in me from the very beginning to the end of the PhD project. I am sincerely grateful for their guidance, encouragement and enthusiasm. Finally, a special thank to prof. Ilaria Cristofolini for the accurate revision of this manuscript.

I would like to thank the company partners which provided the material of this study, especially to the Sacmi staff for their availability on fruitful discussions.

I would like to thank to the PhD colleagues for the continuous and constructive conversations at and out the university laboratories. Specifically, I would like to thank: Matteo, Silvia, Michelangelo, Michele, Daniel, Mara, Giulia, Ana Paula, Enrico, Sunil, Priya and Samuel. I would to express my gratitude to Sasan, that has shared his vast experience on CMM programming and the valuable time spent together in the metrology laboratory.

Last but not least, I would express my sincere gratitude to my mother Antonella, my father Tiziano and my brother Riccardo for helping and encouraging me in the hard times and for supporting my choices along the road that I am walking. Without them nothing would be possible.